PATH PLANNING FOR AIRCRAFT UNDER THREAT OF DETECTION FROM GROUND-BASED RADAR WITH UNCERTAINTY IN AIRCRAFT AND RADAR STATES

by

Austin D. Costley

A dissertation submitted in partial fulfillment
of the requirements for the degree

of

DOCTOR OF PHILOSOPHY

in

Electrical Engineering

Approved:

Greg Droge, Ph.D. Major Professor	Randall Christensen, Ph.D. Committee Member
Jake Gunther, Ph.D. Committee Member	Donald Cripps, Ph.D. Committee Member
Jeff Ferrin, Ph.D. Committee Member	D. Richard Cutler, Ph.D. Vice Provost of Graduate Studies

UTAH STATE UNIVERSITY
Logan, Utah

2022

ABSTRACT

Path Planning for Aircraft Under Threat of Detection from Ground-Based Radar with Uncertainty in Aircraft and Radar States

by

Austin D. Costley, Doctor of Philosophy

Utah State University, 2022

Major Professor: Greg Droge, Ph.D.
Department: Electrical and Computer Engineering

Manned and unmanned aircraft often operate within the detection range of ground-based radar systems. For certain applications, the risk of detection is a primary concern for the mission planners. The detection risk is influenced by several factors, including aircraft pose (i.e., position and orientation), aircraft radar cross-section, radar position, and radar parameters. Current path planning algorithms for the radar detection application assume that these factors are deterministic and known, however, in practice, these factors are estimated and have significant uncertainty. The objective of this research is to explore the incorporation of uncertainty in these factors to inform a path planning algorithm.

The objective is met by quantifying the detection risk and estimating its variability, modeling the uncertainty in the detection factors, and applying these developments to a path planner. The detection risk is quantified by an approximation to the probability of detection, P_D, which is linearized with respect to the aircraft pose, radar position, and radar parameters. The linearized model is used to estimate the variance of P_D induced by these uncertainties. The radar position and radar parameter uncertainty is assumed to be constant while aircraft pose uncertainty is estimated using an inertial navigation filter. To enable rapid path evaluation, this work presents a method to provide analytical expressions

for the nominal aircraft pose and IMU measurements along candidate paths which are used as inputs to the inertial navigation filter. The radar model with uncertainty and the efficient aircraft pose and IMU measurement generator are incorporated into a modified visibility graph path planner that uses the variance of P_D as part of the path validity check. The planner uses a linear covariance model of the aircraft dynamics to enable efficient generation of error budgets that provide actionable information to the mission planner regarding the sources of uncertainty.

(78 pages)

PUBLIC ABSTRACT

Path Planning for Aircraft Under Threat of Detection from Ground-Based Radar with Uncertainty in Aircraft and Radar States

Austin D. Costley

Mission planners for manned and unmanned aircraft operating within the detection range of ground-based radar systems are often concerned with the probability of detection. Several factors influence the probability of detection, including aircraft position and orientation, radar position, and radar performance parameters. Current path planning algorithms assume that these factors are known with certainty, but in practice, these factors are estimated and have some uncertainty.

This dissertation explores methods to consider the uncertainty in the detection factors for an aircraft path planner. First, the detection model is extended to include uncertainty in the aircraft position and orientation, radar position, and radar parameters. Second, an efficient method to estimate the aircraft position and orientation uncertainty is presented that enables rapid path evaluation. Third, the extended radar model and efficient aircraft uncertainty calculation are incorporated into a path planner that evaluates the sources of uncertainty and provides actionable information to the mission planner.

For my wife Jacqueline and our children.

ACKNOWLEDGMENTS

I would like to thank the members of my committee for their support and guidance. Their influence extends beyond the research contained in this dissertation. Thank you to Dr. Jeff Ferrin for his professional mentorship and example of servant leadership; Dr. Donald Cripps for his passion for control systems which inspired me to pursue it as a focus area; Dr. Jake Gunther for his excitement and energy for engineering and tackling difficult problems. A special thanks to Dr. Greg Droge for taking over as my Major Professor and helping me develop as a researcher. His review and advice greatly improved this dissertation. I especially thank Dr. Randy Christensen for his mentorship, encouragement, and guidance throughout this research. His example and influence extends beyond his role as a research advisor and will be felt for years to come.

I would also like to thank my family. Thank you to my parents, Dan and Cyndi, for their incredible example and encouragement in this endeavor. They always taught my sisters and me that we are children of God with unlimited potential - a message a hope to convey to my children. I especially thank my wife Jacqueline for her tireless support, encouragement, and care for our sweet children. I could not have completed this effort without her.

Finally, I thank God for the countless blessings in my life.

Austin D. Costley

CONTENTS

LIST OF FIGURES

CHAPTER 1

INTRODUCTION

Manned and unmanned aircraft operate in the presence of ground-based radar systems which transmit electromagnetic energy into the airspace to search for objects. Aircraft within the detection range of the radar will reflect some of the electromagnetic energy back to the radar system. Several factors influence the level of reflected energy and the probability that the aircraft is detected. These factors include the radar position, radar parameters (e.g., power, aperture, noise factor, loss factor, etc.), aircraft position and orientation, and the physical properties of the aircraft such as the radar cross section (RCS).

Aircraft mission planners concerned with radar detection risk seek to plan paths that keep the probability of detection below a mission-specified threshold given information about the aircraft and radar systems. Aircraft missions concerned with the probability of detection include reconnaissance [1], radar counter-measure deployment [2,3], and combat operations [4]. Current path planning and target detection methods assume that the factors that influence the probability of detection are deterministic and known [2–14]. However, in practice, each detection factor has uncertainty which increases the detection risk.

Uncertainty enters the detection factors listed above in the following ways. First, the position and capability of the radar system is estimated through gathered intelligence which includes satellite imagery or radar transmission detection. Second, the aircraft pose is estimated using a navigation filter that incorporates measurements from noisy and biased sensors. Third, the RCS model is dependent on the aircraft pose so pose uncertainties induce uncertainty in the RCS.

Consider the scenario shown in Figure 1.1 with an aircraft traveling through a region with two radar sensors (S_1, S_2). The radar detection areas are represented by the red regions, and the aircraft position uncertainty is represented by the blue region. The mission objective is to fly to the waypoint marked by the blue "X" and avoid detection. The

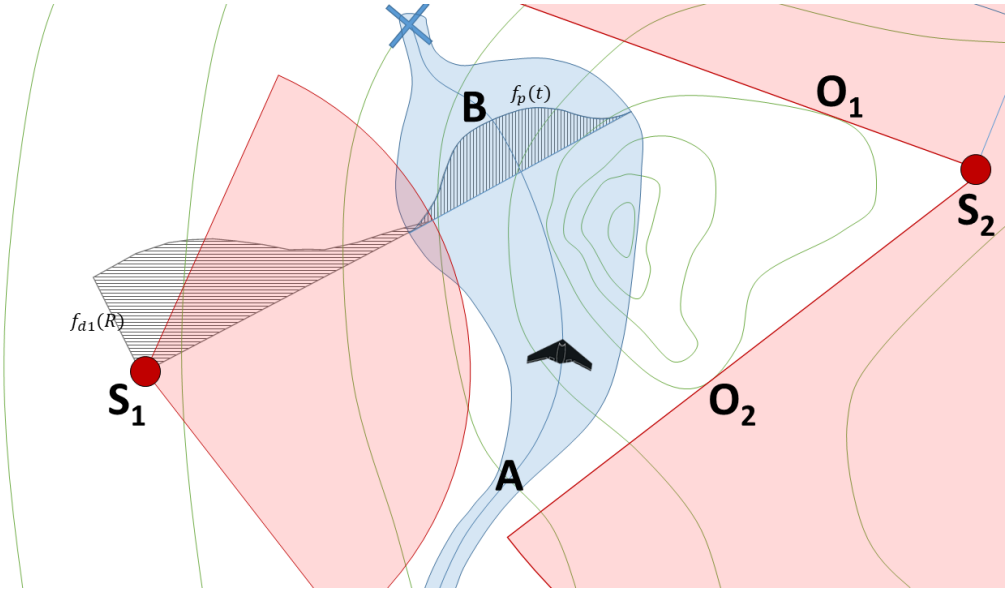

Fig. 1.1: An example of a UAV flying through a region with two radar sensors (S_1, S_2). The simplified detection regions are shown in red. The navigation state uncertainty is represented by the blue region surrounding the path. The distributions of the detection statistics and navigation uncertainty are over-laid on the respective regions. The navigation state uncertainty grows along the path representing a loss in global position measurements.

overlapping area between the blue and red regions represents the probability of detection due, in part, to the aircraft position uncertainty and is the motivation for the research presented in this work. This example leads to several research questions that are discussed in the following paragraphs.

First, how does the path planner calculate the detection risk? The target detection literature provides high-fidelity models for calculating the probability of detection [5–9]. However, current path planning algorithms do not quantify the probability of detection use simplified metrics to represent the detection risk. These metrics include the integrated inverse range models [2, 3, 10–12], peak/aggregate RCS [13], and the radar range equation [14]. An exception is [4], which quantifies the probability of detection using a logistic function approximation but does not provide a relationship between the logistic function variables and the radar parameters.

The research presented in this work uses a high-fidelity radar detection model from

[9] which provides an approximation of the probability of detection, P_D, given the radar position, radar parameters, aircraft pose, and RCS model. The radar detection model uses an approximation from [7] and a consolidated radar constant that is a function of common radar parameters. The radar detection and RCS models used in this work are described in detail in Chapter 2.

Second, how is uncertainty in the detection factors modeled and incorporated into the calculation of the detection risk? The target detection and path planning literature described above does not provide a method for incorporating uncertainty in the detection factors. The research presented in this work provides a method to estimate the variability in the probability of detection given the covariance in the aircraft pose, radar position, and consolidated radar constant. The method uses a linearized radar detection model and a Gaussian uncertainty assumption to estimate the standard deviation of P_D due to uncertainty in the detection factors. Chapter 2 describes the framework for incorporating the aircraft pose covariance into the radar detection model. Chapter 3 extends this framework and includes uncertainty in the radar state (i.e., uncertainty in the radar position and the consolidated radar constant).

Third, how is the radar detection framework incorporated into a path planner? The path planner in this research evaluates whether the detection risk stays below a specified threshold. The detection risk is defined as the sum of P_D and a multiple of the standard deviation of P_D calculated by the radar detection framework. P_D and its standard deviation are functions of the aircraft pose and the radar state with their associated covariances. The planner assumes that the radar state and radar state covariance are constant for a given planning scenario, whereas, the aircraft pose and pose covariance are dependent on the candidate path.

The aircraft pose covariance is estimated by an aided inertial navigation system (INS) that incorporates measurements from an inertial measurement unit (IMU), GPS, and altimeter. The INS estimates the pose covariance using the propagation and update equations from an extended Kalman filter (EKF). Inputs to these equations include the nominal air-

craft pose and sensor measurements along each candidate path. Generating the required aircraft poses and sensor measurements, especially the IMU measurements, is computationally intensive and hinders rapid path planning. To address this, Chapter 4 presents a novel aircraft state and IMU measurement generator (ASG) that provides analytical expressions for the aircraft poses and IMU measurements along a flyable trajectory.

A benefit of modeling the INS is that the planned path can be analyzed to determine the contribution of each source of uncertainty to the variability in P_D. This is accomplished by generating an error budget for the planned path. Error budgets are typically generated using the statistics from several Monte Carlo analyses. In this approach, the planned path is simulated hundreds or thousands of times for each source of uncertainty. This is computationally intensive and not well suited for rapid path planning applications. An alternative to Monte Carlo analysis is linear covariance analysis which uses linearized models and Gaussian noise assumptions to estimate the same statistical information as a Monte Carlo analysis in a single simulation over the planned path.

The radar detection framework, aircraft state generator, and linear covariance analysis are incorporated into a path planner as described in Chapter 5. The radar detection framework enables the planner to consider the variability in P_D induced by the aircraft pose covariance and radar state covariance. The ASG method efficiently generates inputs to an aided-INS to generate the aircraft pose covariance along the candidate path. Finally, linear covariance analysis enables the rapid generation of error budgets which provides actionable information for the mission planner about the planned path.

The radar detection path planning methods referenced above do not consider uncertainty in the aircraft and radar state when evaluating the detection risk of a candidate path. Incorporating these uncertainties provides a more complete picture of the detection risk for aircraft operating near ground-based radar systems. This dissertation describes research to address the challenges of this motivating example and provides the following contributions:

1. Develops a framework for incorporating uncertainty in the aircraft pose, and radar state into the radar detection model to obtain an estimate of the standard deviation

of P_D

2. Develops an analytical aircraft state and IMU measurement generator that converts a series of waypoints into a flyable path and generates samples for the nominal states and sensor measurements for an aided-INS

3. Applies the detection framework and ASG method to a path planner that uses linear covariance analysis to generate error budgets that inform the mission planner about the contribution of each source of uncertainty to the variability of P_D.

The research detailed in this dissertation has been submitted or published in high-quality refereed journals. Each of the following chapters is a paper that contains a relevant literature review, description of methods, and results. The following paragraphs introduce the papers presented in this dissertation and their current publication status.

Sensitivity of Single-Pulse Radar Detection to Aircraft Pose Uncertainties [15]
Submitted: *IEEE Transactions on Aerospace and Electronic Systems*
Provided in Chapter 2, this paper presents the radar detection model used in this dissertation and develops a framework for incorporating aircraft state covariance into the radar detection model. The framework linearizes the equations used to calculate P_D and includes support for three RCS models (i.e., constant, ellipsoid, simple spikeball). It is shown that the linearization is valid for high levels of state uncertainty and that even moderate levels of state uncertainty induce significant variability in P_D.

Sensitivity of Single-Pulse Radar Detection to Radar State Uncertainty [16]
Submitted: *IEEE Transactions on Aerospace and Electronic Systems*
Provided in Chapter 3, this paper extends the framework developed in [15] to incorporate uncertainties in the radar state which includes the radar position and the consolidate radar parameter. The framework is extended by defining partial derivatives of the equations used to calculate P_D with respect to the radar state. The linearization is validated with a Monte Carlo analysis and the results show that P_D is moderate radar state uncertainty induce

significant variability in P_D.

Analytical Aircraft State and IMU Signal Generator from Smoothed Reference Trajectory [17]

Published: *IEEE Transactions on Aerospace and Electronic Systems*

Provided in Chapter 4, this paper develops a method, ASG, to translate a series of waypoints to a flyable trajectory with analytical expressions for the aircraft states and IMU measurements along the path. The method uses a corner smoothing algorithm to convert a series of waypoints into continuous curvature path segments. Curvilinear motion theory and a coordinated turn assumption are used to obtain an expression for the specific force and angular rates experienced by the aircraft as it travels along the trajectory. The results illustrate three corner smoothing algorithms and show that the IMU measurements are accurate and consistent with the integration method provided by Groves [18].

Path Planning with Uncertainty for Aircraft Under Threat of Detection from Ground-Based Radar [19]

Submitted: *Under Review - Will submit to Robotics and Autonomous Systems*

Provided in Chapter 5, this paper incorporates the radar detection framework presented in Chapters 2 and 3 and the ASG method presented in Chapter 4 into a path planner. The planner uses an aided-INS to fuse measurements from the IMU, GPS, and altimeter and estimate the aircraft state covariance. Linear covariance analysis is used to evaluate the final trajectory and generate an error budget. The results show that the planner successfully maintains the detection risk below the mission-specified threshold and provide an example of how a mission planner may use the error budget information to improve the planned path.

REFERENCES

[1] N. Ceccarelli, J. J. Enright, E. Frazzoli, S. J. Rasmussen, and C. J. Schumacher, "Micro uav path planning for reconnaissance in wind," in *2007 American Control Conference*, 2007, pp. 5310–5315.

[2] R. Larson, M. Pachter, and M. Mears, "Path Planning by Unmanned Air Vehicles for Engaging an Integrated Radar Network," in *AIAA Guidance, Navigation, and Control Conference and Exhibit*. American Institute of Aeronautics and Astronautics, 2001.

[3] F. Xiao-wei, L. Zhong, and G. Xiao-guang, "Path Planning for UAV in Radar Network Area," in *2010 Second WRI Global Congress on Intelligent Systems*, vol. 3, Dec. 2010, pp. 260–263.

[4] P. T. Kabamba, S. M. Meerkov, and F. H. Z. III, "Optimal Path Planning for Unmanned Combat Aerial Vehicles to Defeat Radar Tracking," *Journal of Guidance, Control, and Dynamics*, May 2012.

[5] J. Marcum, "A statistical theory of target detection by pulsed radar," *IRE Transactions on Information Theory*, vol. 6, no. 2, pp. 59–267, Apr. 1960.

[6] P. Swerling, "Probability of Detection for Fluctuating Targets," RAND Corporation, Tech. Rep., Jan. 1954.

[7] D. North, "An Analysis of the factors which determine signal/noise discrimination in pulsed-carrier systems," *Proceedings of the IEEE*, vol. 51, no. 7, pp. 1016–1027, Jul. 1963.

[8] D. K. Barton, "Modern radar system analysis," *Norwood, MA, Artech House, 1988, 607 p.*, 1988.

[9] B. R. Mahafza and A. Elsherbeni, *MATLAB Simulations for Radar Systems Design*. CRC Press, Dec. 2003.

[10] S. Bortoff, "Path planning for UAVs," in *Proceedings of the 2000 American Control Conference. ACC (IEEE Cat. No.00CH36334)*, vol. 1, Jun. 2000, pp. 364–368 vol.1, iSSN: 0743-1619.

[11] P. Chandler, S. Rasmussen, and M. Pachter, "UAV cooperative path planning," in *AIAA Guidance, Navigation, and Control Conference and Exhibit*. Dever,CO,U.S.A.: American Institute of Aeronautics and Astronautics, Aug. 2000.

[12] M. Pachter and J. Hebert, "Optimal aircraft trajectories for radar exposure minimization," in *Proceedings of the 2001 American Control Conference. (Cat. No.01CH37148)*, vol. 3, Jun. 2001, pp. 2365–2369 vol.3, iSSN: 0743-1619.

[13] F. Moore, "Radar cross-section reduction via route planning and intelligent control," *IEEE Transactions on Control Systems Technology*, vol. 10, no. 5, pp. 696–700, Sep. 2002.

[14] M. McFarland, R. Zachery, and B. Taylor, "Motion planning for reduced observability of autonomous aerial vehicles," in *Proceedings of the 1999 IEEE International Conference on Control Applications (Cat. No.99CH36328)*, vol. 1, Aug. 1999, pp. 231–235 vol. 1.

[15] A. Costley, R. Christensen, G. Droge, and R. C. Leishman, "Sensitivity of single-pulse radar detection to aircraft pose uncertainties," 2022, under review, available in preprint at https://arxiv.org/abs/2201.06727.

[16] A. Costley, R. Christensen, R. C. Leishman, and G. Droge, "Sensitivity of single-pulse radar detection to radar state uncertainty," 2022, under review, available in preprint at https://arxiv.org/abs/2203.11372.

[17] A. Costley, R. Christensen, R. C. Leishman, and G. N. Droge, "Analytical aircraft state and imu signal generator from smoothed reference trajectory," *IEEE Transactions on*

Aerospace and Electronic Systems, vol. 58, no. 3, pp. 2517–2530, 2022, ©2021 IEEE. Reprinted, with permission.

[18] P. D. Groves, *Principles of GNSS, Inertial, and Multisensor Integrated Navigation Systems*. Norwood, UNITED STATES: Artech House, 2013.

[19] A. Costley, G. Droge, R. Christensen, R. C. Leishman, and J. Swedeen, "Path Planning with Uncertainty for Aircraft Under Threat of Detection from Ground-Based Radar," Jul. 2022. [Online]. Available: https://arxiv.org/abs/2207.03716v1

CHAPTER 2

SENSITIVITY OF SINGLE-PULSE RADAR DETECTION TO AIRCRAFT POSE UNCERTAINTIES

Sensitivity of Single-Pulse Radar Detection to Aircraft Pose Uncertainties

Mr. Austin Costley, Dr. Randall Christensen, Dr. Robert C. Leishman, Dr. Greg Droge

***Abstract*—Mission planners for aircraft that operate in radar detection environments are often concerned with the probability of detection. The probability of detection is a nonlinear function of the aircraft pose and radar position. Current path planning techniques for this application assume that the aircraft pose is deterministic. In practice, however, the aircraft pose is estimated using a navigation filter and therefore contains uncertainty. The uncertainty in the aircraft pose induces uncertainty in the probability of detection, but this phenomenon is generally not considered when path planning. This paper provides a method for combining aircraft pose uncertainty with single-pulse radar detection models to aid mission planning efforts. The method linearizes the expression for the probability of detection and two radar cross section models. The linearized models are then used to determine the variability of the probability of detection induced by uncertainty in the aircraft pose. The results of this paper verifies the linearization using Monte Carlo analysis and explores the sensitivity of the probability of detection to aircraft pose uncertainty.**

NOMENCLATURE

P_D	Probability of detection
$\bar{P}_D$	P_D at nominal state
P_{fa}	Probability of false alarm
$\mathcal{S}$	Signal-to-noise ratio
σ_r	Radar cross section (m^2)
R	Range to target (m)
c_r	Lumped radar parameter ($Jm^2/^\circ K$)
NED	North-East-Down coordinate frame
$\boldsymbol{x_a}$	Aircraft state vector
$\bar{\boldsymbol{x}}_{\boldsymbol{a}}$	Nominal aircraft state vector
$\delta \boldsymbol{x_a}$	Aircraft perturbation state vector
$\boldsymbol{p_a^n}$	Aircraft position vector in NED frame
$\boldsymbol{\Theta}$	Aircraft Euler angle vector ($rad.$)
p_{an}, p_{ae}, p_{ad}	Aircraft position in NED frame (m)
ϕ_a, θ_a, ψ_a	Aircraft Euler angles roll, pitch, yaw ($rad.$)
$\boldsymbol{p_r^n}$	Radar position vector in NED frame
p_{rn}, p_{re}, p_{rd}	Radar position elements in NED frame (m)
$\boldsymbol{\rho_r^b}$	Radar position vector in aircraft body frame
ρ_{rx}, ρ_{ry}, ρ_{rz}	Radar position in aircraft body frame (m)
σ_{re}	Ellipsoid RCS (m^2)
a, b, c	Ellipsoid RCS parameters (m)
σ_{rs}	Simple spikeball RCS (m^2)
a_s, b_s	Simple spikeball RCS parameters (m^2)
α	RCS azimuth angle ($rad.$)
ϕ	RCS elevation angle ($rad.$)
θ_r	Radar detection azimuth angle ($rad.$)
ϕ_r	Radar detection elevation angle ($rad.$)
C_{xx}	Aircraft pose covariance
C_{P_D}	Variance of P_D
σ_{pd}	Standard deviation of P_D

This work was supported by Air Force Research Laboratory, Wright-Patterson Air Force Base, OH.

A. Costley is with the Electrical and Computer Engineering Department, Utah State University, Logan, UT 84322 USA (e-mail: austin.costley@usu.edu)

R. Christensen is with the Electrical and Computer Engineering Department, Utah State University, Logan, UT 84322 USA (e-mail: randall.christensen@usu.edu)

R. Leishman is with the ANT Center, Air Force Institute of Technology, Wright-Patterson Air Force Base, OH 45433 USA (e-mail: robert.leishman@afit.edu)

G. Droge is with the Electrical and Computer Engineering Department, Utah State University, Logan, UT 84322 USA (e-mail: greg.droge@usu.edu)

I. INTRODUCTION

Manned and unmanned aircraft are often tasked with operating under threat of detection from ground-based radar systems. Mission planners must plan paths that maintain the probability of detection below mission-specified levels. A path that fails to meet this criteria may present an unacceptable level of risk to the pilot or aircraft. Missions that are concerned with detection risk include reconnaissance [1], radar counter-measure deployment [2, 3], and combat operations [4]. A number of factors contribute to the probability of detection. The factors include the aircraft position and orientation (pose), radar system parameters, the physical characteristics of the aircraft (e.g. radar cross section (RCS)), and atmospheric conditions.

A common assumption when modeling the detection probability is that the aircraft pose along the planned path is deterministic and known [2–13]. In practice, uncertainties in the aircraft pose enter through a variety of sources. First, disturbances arise due to environmental factors (e.g. wind gusts [14]) and the physical characteristics of the aircraft (e.g., wing and tail design). Second, the inertial navigation system on the UAV estimates the pose of the aircraft using noisy and biased sensors [15–17]. Considering navigation errors is particularly important for regions where global position measurements are contested, degraded, or denied. When these uncertainties are taken into account, the aircraft pose is represented by a probabilistic distribution. The variability in the resulting distribution induces variability in the predicted probability of detection. This can be illustrated using Monte Carlo analysis where samples from the distribution of the aircraft pose result in a range of detection probabilities. This paper develops a framework for incorporating aircraft pose uncertainty in the calculation of the probability of detection, P_D, for a single-pulse radar model. It is shown that pose uncertainty can be a significant source of variability in the probability of detection.

Current path planning methods use a variety of approaches to evaluate the detection risk and survivability along candidate paths. Detection risk methods include the integrated inverse range models [2, 3, 6–8], peak/aggregate RCS [9], and the radar range equation [5]. Although these approaches model the detection risk, they do not quantify the probability of detection, which is necessary to plan paths that maintain the probability of detection below a mission-specified threshold. Other methods extend the detection risk evaluation and consider aircraft survivability, which includes modeling adversarial sensor networks and weapons systems to determine the probability that the aircraft will complete the mission [4, 11–13]. The approach in [4, 11] uses a logistic function approximation of the probability of detection and integrates it over a window of time to model a adversary tracking and engaging the aircraft. Alternatively, [12, 13] use Markov processes with transition probabilities to determine if the aircraft is detected, tracked, and engaged. The survivability methods provide an extended view of the path planning problem but they are beyond the scope of this paper and do not consider aircraft pose uncertainty in their models. The approach in this paper focuses on a path planning application where the instantaneous probability of detection is predicted while considering aircraft pose uncertainty.

The target detection literature has made various developments to create high-fidelity radar detection models. The single-pulse radar model is used to determine the instantaneous probability of detection given radar parameters, radar position, and the pose of the detected aircraft. Marcum [18] expresses target detection as a probability using a nonlinear function of the radar parameters, target radar cross section (RCS), and range to target. Swerling [19] extends the work by Marcum to include fluctuating targets for multiple-pulse detection models. Mahafza [20] extends the work by Marcum and Swerling to include considerations for modeling modern radar systems and provides expressions for common RCS models as a function of the aircraft pose (position and orientation) relative to the radar. The probability of detection thus depends upon various radar parameters, the inverse of the relative range, and the relative pose of the aircraft with respect to the radar.

Despite the significant dependence upon relative aircraft pose, none of the literature mentioned above considers the effects of aircraft pose uncertainty on the predicted probability of detection. The primary contribution of this paper is a framework for incorporating aircraft pose uncertainty with the single-pulse radar detection model presented by Mahafza. This is accomplished by linearizing the expression for the probability of detection with respect to aircraft pose. The linearized system is then used to approximate, to the first order, the variance of the probability of detection due to the pose uncertainty. The results verify the linearization by running a Monte Carlo analysis and illustrate the sensitivity of the probability of detection to several aircraft pose uncertainty levels. The framework may be used by mission planners to better understand the variability of the detection risk due to aircraft pose uncertainty. The resulting information can be used to plan paths to avoid detection in the presence of uncertainty, which is a primay objective of operating near adversarial radar networks.

This paper is organized as follows. The single-pulse radar detection and RCS models are discussed in Section II. The framework for linearizing the expression for the probability of detection and incorporating aircraft pose uncertainty is presented in Section III. The results for this paper are provided in Section IV where the linearization is verified and the sensitivity of the probability of detection to aircraft pose uncertainty is presented.

II. Radar Detection Model

This section describes the single-pulse detection model as presented by Mahafza [20]. The model includes expressions for the probability of detection, P_D, signal-to-noise ratio, $\mathcal{S}$, and RCS, σ_r, as functions of the aircraft pose and radar position. This section uses the ellipsoid RCS models from [20] and defines the simple spikeball as a second model.

The singe-pulse detection model described in this section quantifies P_D given the aircraft pose and radar position. An approximation to P_D is used to provide a differentiable function which will be leveraged in the following section. The simplified model does not account for fluctuating targets or multiple radar frequencies which may be added to this framework in the future. Similarly, the RCS models presented in this section provide analytical expressions for the RCS based on the relative pose of the aircraft. These models balance fidelity and computational complexity with the intnent of enabling path planning algorithms that must rapidly evaulate many possibilities. Mission planners should consider the fidelity required for their specific applications.

A. Probability of Detection

P_D is a function of the probability of false alarm, P_{fa}, and the signal-to-noise ratio, $\mathcal{S}$. P_{fa} is a considered a constant for a particular radar, while $\mathcal{S}$ depends both on radar parameters and the relative target pose. A common expression for P_D is Marcum's Q-function [20]. However, it contains an integral that does not have a closed form solution. An accurate approximation to P_D, provided by North [20, 21], is

$$P_D \approx 0.5 \times \text{erfc}\left(\sqrt{-\ln P_{fa}} - \sqrt{\mathcal{S} + 0.5}\right) \tag{1}$$

where $\text{erfc}(\cdot)$ is the complementary error function given by

$$\text{erfc}(z) = 1 - \frac{2}{\sqrt{\pi}} \int_0^z e^{-\zeta^2} d\zeta. \tag{2}$$

Fig. 1 shows an example graph of P_D with respect to $\mathcal{S}$.

A general expression for the signal-to-noise ratio is a function of the radar constant, c_r, radar cross section, σ_r, and range to the radar, R, given by

$$\mathcal{S} \quad = \quad c_r \frac{\sigma_r}{kR^4} \tag{3}$$

where k is Boltzmann's constant $(1.38 \times 10^{-23}\ J/^\circ K)$. The radar constant, c_r, is a function of radar parameters such as power, aperture area, noise figure, and loss factor and is dependent on the type of radar being modeled. The specific

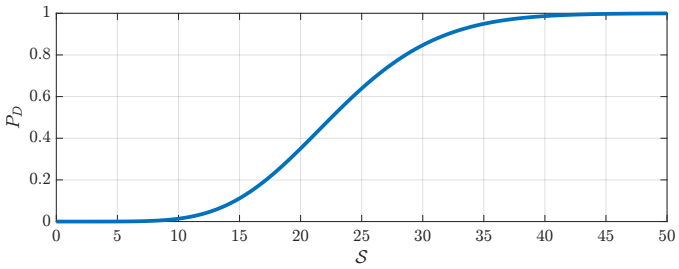

Fig. 1: P_D with respect to $\mathcal{S}$ for a constant $P_{fa} = 1e^{-10}$. $\mathcal{S}$ is determined by the aircraft state and radar position and parameters.

radar parameters are not critical to the development of this paper so they will be lumped into a single radar constant. The following paragraphs describe the calculation of σ_r and R given the radar position and the pose of the target aircraft.

Consider the detection event depicted in Fig. 2. The range, R, is calculated using the aircraft and radar positions. The RCS, σ_r, is a function of the azimuth and elevation angles to the radar, which are determined by the pose of the aircraft and the radar position. Let the aircraft position in the NED frame, $\boldsymbol{p_a^n}$, and orientation, $\boldsymbol{\Theta_a}$, be defined by

$$\boldsymbol{p_a^n} = \begin{bmatrix} p_{an} & p_{ae} & p_{ad} \end{bmatrix}^\intercal \quad (4)$$

$$\boldsymbol{\Theta_a} = \begin{bmatrix} \phi_a & \theta_a & \psi_a \end{bmatrix}^\intercal \quad (5)$$

where $\boldsymbol{\Theta_a}$ is a vector of Euler angles for the roll, pitch, and yaw of the aircraft [22]. Thus, (3) is expressed more explicitly as

$$\mathcal{S}\left(\boldsymbol{p_a^n}, \boldsymbol{\Theta_a}\right) = c_r \frac{\sigma_r\left(\boldsymbol{p_a^n}, \boldsymbol{\Theta_a}\right)}{kR\left(\boldsymbol{p_a^n}\right)^4}. \quad (6)$$

and the range to the radar is given by

$$R(\boldsymbol{p_a^n}) = ||\boldsymbol{p_a^n} - \boldsymbol{p_r^n}||_2 \quad (7)$$

where $\boldsymbol{p_r^n}$ represents the position of the radar in the NED frame with

$$\boldsymbol{p_r^n} = \begin{bmatrix} p_{rn} & p_{re} & p_{rd} \end{bmatrix}^\intercal. \quad (8)$$

In this work the radar position is assumed to be deterministic and known.

B. Radar Cross Section Models

The RCS of an aircraft is dependent on several factors including the azimuth and elevation angles to the radar, radar frequency, and the aircraft size, shape, and material. In this work, the RCS will be calculated using simplified models that illustrate the sensitivity of RCS to the pose of the aircraft relative to the radar. The RCS models provide analytical expressions for the RCS value as a function of the azimuth and elevation angles of the radar detection vector in the body frame of the aircraft that represent the backscattered RCS using a Physical Optics approximation [20]. The RCS representations used in this work are described in the following paragraphs.

The body frame x and y axes are shown as b_x and b_y in Fig. 2. The body frame z axis points out of the bottom of the aircraft. The relative position of the radar in the body frame of the aircraft is given by

$$\boldsymbol{\rho_r^b} = \begin{bmatrix} \rho_{rx} & \rho_{ry} & \rho_{rz} \end{bmatrix}^\intercal. \quad (9)$$

The vector $\boldsymbol{\rho_r^b}$ is calculated using the aircraft pose and radar position by

$$\boldsymbol{\rho_r^b} = T_n^b\left(\boldsymbol{p_r^n} - \boldsymbol{p_a^n}\right) \quad (10)$$

where T_n^b is the direction cosine matrix formed by the ZYX Euler angle sequence [22] given by

$$T_n^b = \begin{bmatrix} C\psi_a C\theta_a & -C\phi_a S\psi_a + C\psi_a S\phi_a S\theta_a & S\phi_a S\psi_a + C\phi_a C\psi_a S\theta_a \\ C\theta_a S\psi_a & C\phi_a C\psi_a + S\phi_a S\psi_a S\theta_a & -C\psi_a S\phi_a + C\phi_a S\psi_a S\theta_a \\ -S\theta_a & C\theta_a S\phi_a & C\phi_a C\theta_a \end{bmatrix} \quad (11)$$

and S$\cdot$ and C$\cdot$ are the $\sin(\cdot)$ and $\cos(\cdot)$ functions.

The RCS azimuth angle is the angle from the body frame x axis to the projection of the radar detection vector into the x-y plane of the body frame. The RCS elevation angle ϕ is the angle from the x-y plane in the body frame of the aircraft to the radar detection vector with a positive angle towards the bottom of the aircraft. The RCS azimuth and elevation angles are given by

$$\alpha = \arctan\left(\frac{\rho_{ry}}{\rho_{rx}}\right) \quad (12)$$

and

$$\phi = \arctan\left(\frac{\rho_{rz}}{\sqrt{(\rho_{rx})^2 + (\rho_{ry})^2}}\right). \quad (13)$$

A common graphical representation of an RCS model is a polar plot, where the angle is either the RCS azimuth or elevation angle and the radius represents the RCS value. Fig. 3 provides example polar plots for three radar cross section models as functions of the RCS azimuth angle. The complex spikeball (Fig. 3a) is the highest fidelity model and is generally obtained through radar measurements and data gathering or computational electromagnetics [23].

Path planners often [4, 5, 9] use simplified models such as those in Figs. 3b-3c because they provide analytical expressions for the RCS. The simplified models employed in this work are the ellipsoid and simple spikeball models. The ellipsoid model captures large broadside cross sections that are common for fixed-wing aircraft. The spikeball model has repeating lobes around the aircraft where the number and size of the lobes is configurable. The spikeball model also illustrates the performance of the method presented in this work when strong non-linearities are present in the RCS model. A mission planner should select an RCS model and associated model parameters that approximate of the aircraft RCS to captures the primary structure of the data. The remainder of this section presents equations for computing the RCS for the simplified models as a function of the RCS azimuth and elevation angles.

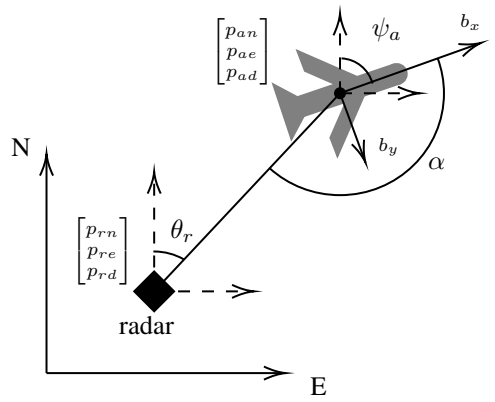

Fig. 2: Graphical representation of the quantities used in the radar detection model.

The first RCS model is the ellipsoid. The equation for the RCS of an ellipsoid [4, 20] represents a 3dimensional surface given by

$$\sigma_{re} = \frac{\pi \left(abc\right)^2}{\left(\left(a\,\mathrm{S}\alpha\,\mathrm{C}\phi\right)^2 + \left(b\,\mathrm{S}\alpha\,\mathrm{S}\phi\right)^2 + \left(c\,\mathrm{C}\alpha\right)^2\right)^2} \tag{14}$$

where a, b, and c, are the length of the ellipsoid axes. A polar plot of the ellipsoid RCS with respect to α is shown in Fig. 3b. Note that the ellipsoid model is also a function of the elevation angle, ϕ.

The second RCS model the "simple spikeball." The term comes from the shape of the plot in polar coordinates. An example of a simple spikeball with four lobes is shown in Fig. 3c. The expression for a simple spikeball RCS is given by

$$\sigma_{rs} \quad = \quad \left|a_s \sin\left(\frac{n}{2}\alpha\right)\right| + b_s \tag{15}$$

where a_s determines the amplitude of the lobes, b_s is the minimum RCS value, and n determines the number of lobes. Note that the simple spikeball model does not depend on ϕ.

III. Linearized Probability of Detection

The aircraft pose is represented by a Gaussian distributed random variable with a mean $\boldsymbol{x_a} = \begin{bmatrix}\boldsymbol{p_a^n} & \boldsymbol{\Theta_a}\end{bmatrix}^\mathsf{T}$ and covariance C_{xx}. The prior sections have shown that P_D is a nonlinear function of the aircraft state. Hence, variability in the aircraft pose induces variability in the probability of detection. The expected P_D (i.e. the mean) and the uncertainty (i.e. variance) are approximated by linearizing (1) about the aircraft state. The framework presented in this paper does not dictate how the pose uncertainty is calculated or stipulate what error sources are considered in its calculation. It is left to the mission planner to determine what uncertainty sources and resulting pose covariance best represent the planning application.

The combination of (1) and (6) provides an expression for P_D as a function of the aircraft pose, $\boldsymbol{x_a}$, which is expressed as a nominal pose, $\bar{\boldsymbol{x}}_{\boldsymbol{a}}$, with a perturbation, $\delta\boldsymbol{x_a}$, as

$$\boldsymbol{x_a} = \bar{\boldsymbol{x}}_{\boldsymbol{a}} + \delta\boldsymbol{x_a}. \tag{16}$$

In general, P_D is a nonlinear function with respect to the pose of the detected aircraft. However, variations in P_D can be approximated by linearizing Eqs. (1), (6), and (7) about a nominal operating point using a Taylor series expansion to obtain

$$\delta P_D \approx \frac{\partial P_D}{\partial \mathcal{S}}\left(\frac{\partial \mathcal{S}}{\partial R}\frac{\partial R}{\partial \boldsymbol{x_a}} + \frac{\partial \mathcal{S}}{\partial \sigma_r}\frac{\partial \sigma_r}{\partial \boldsymbol{x_a}}\right)\Bigg|_{\bar{\boldsymbol{x}}_{\boldsymbol{a}}} \delta\boldsymbol{x_a} \tag{17}$$

$$\approx A_P \delta\boldsymbol{x_a}. \tag{18}$$

where δP_D is the perturbation of P_D due to the perturbation of the aircraft state. The nominal operating point, $\bar{\boldsymbol{x}}_{\boldsymbol{a}}$, is chosen as the nominal aircraft pose around which the perturbations are being calculated. The variance of P_D due to aircraft pose uncertainty is computed using a similarity transform as

$$C_{P_D} = E\left[\delta P_D \delta P_D^\mathsf{T}\right] \tag{19}$$

$$= A_P C_{xx} A_P^\mathsf{T} \tag{20}$$

and the standard deviation is given by

$$\sigma_{pd} = \sqrt{C_{P_D}}. \tag{21}$$

These equations show that A_P must be calculated to compute the variability of P_D. The following subsections will define the five partial derivatives from (17) required to compute A_P.

A. Partial Derivative of P_D with Respect to $\mathcal{S}$

The partial derivative of P_D with respect to $\mathcal{S}$ is computed by combining (1) and (2) to obtain

$$P_D \quad \approx \quad 0.5 - \frac{1}{\sqrt{\pi}}\int_0^W \exp\left(-\zeta^2\right) d\zeta \tag{22}$$

where

$$W \quad = \quad \sqrt{-\ln P_{fa}} - \sqrt{\mathcal{S} + 0.5}. \tag{23}$$

Proceed by computing the derivative of P_D with respect to W by applying the fundamental theorem of calculus

$$\frac{\partial P_D}{\partial W} = \frac{-\exp\left(-W^2\right)}{\sqrt{\pi}} \tag{24}$$

The partial derivative of W with respect to $\mathcal{S}$ is given by

$$\frac{\partial W}{\partial \mathcal{S}} = \frac{-1}{2\sqrt{\mathcal{S} + 0.5}}.$$

It follows that

$$\frac{\partial P_D}{\partial \mathcal{S}} = \frac{\partial P_D}{\partial W}\frac{\partial W}{\partial \mathcal{S}} = \frac{\exp\left(-W^2\right)}{2\sqrt{\pi}\sqrt{\mathcal{S} + 0.5}}. \tag{25}$$

B. Partial Derivative of $\mathcal{S}$ with Respect to Range

The partial derivative of the signal-to-noise ratio (6) with respect to range is given by

$$\frac{\partial \mathcal{S}}{\partial R} = -c_r \frac{4\sigma_r}{kR^5}. \tag{26}$$

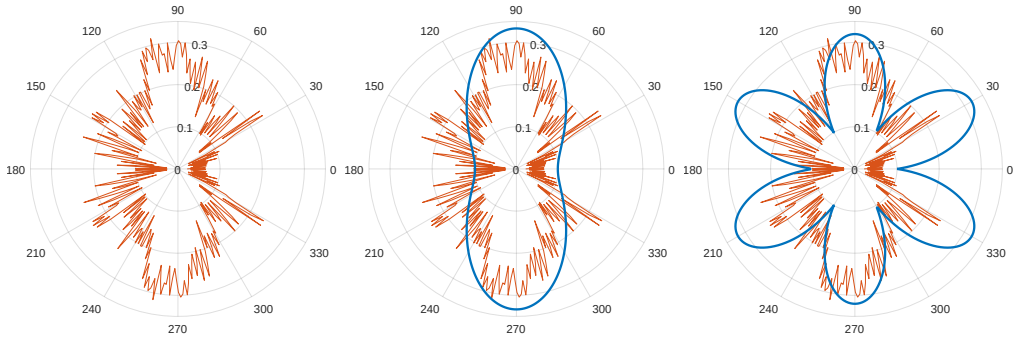

(a) Complex Spikeball (b) Ellipsoid (c) Simple Spikeball

Fig. 3: Examples of four RCS models as a function of the azimuth angle, α, where the aircraft nose is pointed towards the 0 degree line. (a) Shows the highest fidelity model and is typically obtained through measurements. (b) and (c) Show the ellipsoid and simple spikeball RCS models that are dependent on radar azimuth angle α. The ellipsoid model is a 3D ellipsoid that is also dependent on the radar elevation angle ϕ (not pictured). The complex spikeball is included on the other figures to show how these models may be used to approximate the high-fidelity model.

C. Partial Derivative of Range with Respect to Aircraft State

The range or distance between the aircraft and the radar is given by (7). The partial derivative of range with respect to the aircraft position is given by

$$\frac{\partial R}{\partial \boldsymbol{x_a}} = \left[\frac{\partial}{\partial \boldsymbol{p_a}}||\boldsymbol{p_a}-\boldsymbol{p_r}||_2 \quad \boldsymbol{0_{1x3}}\right] \tag{27}$$

$$= \left[\frac{(\boldsymbol{p_a}-\boldsymbol{p_r})^\intercal}{||\boldsymbol{p_a}-\boldsymbol{p_r}||_2} \quad \boldsymbol{0_{1x3}}\right]. \tag{28}$$

D. Partial Derivative of $\mathcal{S}$ with Respect to Radar Cross Section

The partial derivative of the signal-to-noise ratio (6) with respect to the RCS is given by

$$\frac{\partial \mathcal{S}}{\partial \sigma_r} = c_r \frac{1}{kR^4}. \tag{29}$$

E. Partial Derivative of RCS with Respect to Aircraft State

The partial derivative of the RCS with respect to the aircraft state, $\frac{\partial \sigma_r}{\partial \boldsymbol{x_a}}$, is dependent on the choice of RCS model. The lengthy derivation of the partial derivatives of the RCS models presented in Section II-B are provided in Appendix A.

F. Combining Expressions for A_P

Finally, the partial derivatives calculated in the preceding subsections are combined to obtain an expression for A_P as

$$A_P = \left[-c_r \frac{2\exp\left(-W^2\right)(\boldsymbol{p_a}-\boldsymbol{p_r})^\intercal}{kR^6\sqrt{\pi}\sqrt{\mathcal{S}+0.5}} \quad \boldsymbol{0_{1x3}}\right] \tag{30}$$

$$+c_r \frac{\exp\left(-W^2\right)}{2kR^4\sqrt{\pi}\sqrt{\mathcal{S}+0.5}} \frac{\partial \sigma_r}{\partial \boldsymbol{x_a}} \tag{31}$$

where $\frac{\partial \sigma_r}{\partial \boldsymbol{x_a}}$ depends on the chosen RCS model as defined in Appendix A. The resulting expression for A_p is used to compute the variance of P_D with respect to the aircraft state uncertainty using (21). Section IV provides results that verify the linearization presented in this section and illustrates the sensitivity of P_D to aircraft state uncertainty.

TABLE I: Radar parameters for used in results section

Param	Value	Description
a	0.2 m	Ellipsoid RCS forward axis length
b	0.24 m	Ellipsoid RCS side axis length
c	0.26 m	Ellipsoid RCS up axis length
a_s	0.18 m^2	Spikeball RCS lobe amplitude
b_s	0.12 m^2	Spikeball RCS minimum
n	6	Number of lobes
L σ_{pa}	0.1 m	Low position state std. dev.
M σ_{pa}	10 m	Medium position state std. dev.
H σ_{pa}	100 m	High position state std. dev.
L σ_{ang}	0.1 deg.	Low Euler angle state std. dev.
M σ_{ang}	1 deg.	Medium Euler angle state std. dev.
H σ_{ang}	2 deg.	High Euler angle state std. dev.
$\bar{\psi}_a$	0 deg.	Aircraft course angle
$\bar{p}_{ad}$	-3 km	Aircraft position along "down" axis
$\boldsymbol{p_r^n}$	$\boldsymbol{0_{3\times 1}}$ m	Radar position vector (NED)
c_r	167.4 $Jm^2/°K$	Lumped radar constant
P_{fa}	$1.7e^{-4}$	Probability of false alarm
R	600 km	Range to aircraft

IV. Results

The results for this paper are separated into two sections. First, results are presented to verify the linearization of the radar detection and RCS models. Second, the sensitivity of P_D to the aircraft state uncertainty is presented. Both sections provide results for the RCS models presented in Section II-B for three levels of aircraft state uncertainty (low, medium, high). Table I provides the parameter values used in this section. The radar parameters represent a surveillance radar from examples in [20]. The aircraft pose uncertainty levels are associated with a navigation system aided by GPS measurements (Low), degraded GPS measurements (Medium), and no GPS measurements (High).

A. Linearization Verification

The linearization described in Section III provides a first order approximation to variations in the nonlinear radar detection model due to variations in the aircraft pose. The validity of this approximation is dependent on the operating point $\bar{\boldsymbol{x}}_{\boldsymbol{a}}$, the RCS model, and the pose uncertainty C_{xx} and is assessed in this section.

The linearization verification will be illustrated using Monte Carlo analysis for a scenario where the radar is at the origin of the NED frame ($\boldsymbol{p}_{\boldsymbol{r}}^{\boldsymbol{n}} = \mathbf{0}_{\mathbf{3}\times\mathbf{1}}$) and the aircraft position is rotated around the radar at a nominal range with a fixed nominal heading and altitude. In this approach, the aircraft is considered at a series of nominal poses that are perturbed with random samples according to the state uncertainty level. The k^{th} nominal aircraft pose is given by

$$\bar{\boldsymbol{x}}_{\boldsymbol{a}}[k] = \begin{bmatrix} R\sin(\theta_r[k]) & R\cos(\theta_r[k]) & \bar{p}_{ad} & \mathbf{0}_{\mathbf{1}\times\mathbf{3}} \end{bmatrix}^{\mathsf{T}}, \quad (32)$$

where $\theta_r[k]$ ranges from 0–180 degrees in increments of 0.5 degrees. The nominal range, $R = 600$ km, ensures that P_D is near 0.5 for some values of θ_r given the RCS models defined in Table I and $\bar{p}_{ad} = -3$ km which is within the operating altitude for tactical unmanned aircraft [24]. The nominal state for the i^{th} Monte Carlo run is perturbed using

$$\boldsymbol{x}_{\boldsymbol{a},\boldsymbol{i}}[k] = \bar{\boldsymbol{x}}_{\boldsymbol{a},\boldsymbol{i}}[k] + \boldsymbol{w}_{\boldsymbol{i}}[k] \quad (33)$$

where $\boldsymbol{w}_{\boldsymbol{i}}[k]$ is sampled as a zero-mean Gaussian distributed random vector with a covariance matrix given by

$$C_{xx} = \begin{bmatrix} \sigma_{pa}\mathbf{I}_{\mathbf{3}\times\mathbf{3}} & \mathbf{0} \\ \mathbf{0} & \sigma_{ang}\mathbf{I}_{\mathbf{3}\times\mathbf{3}} \end{bmatrix}. \quad (34)$$

The perturbed states are used to calculate $P_D[k]$ using (1) for each $\theta_r[k]$ value. The collection of P_D values over the range of θ_r make up a single Monte Carlo run. The full Monte Carlo analysis consisted of 1000 runs. In addition to P_D calculated from the perturbed states, $\bar{P}_D$ is calculated with (1) using the nominal aircraft state, $\bar{\boldsymbol{x}}_{\boldsymbol{a}}$.

The Monte Carlo results are provided in Figs. 4-5, which show gray lines representing P_D calculated for each Monte Carlo run over a range of radar azimuth angles, θ_r. The standard deviation estimated with the linearized system, σ_{pd}, is calculated using (21) with $\bar{\boldsymbol{x}}_{\boldsymbol{a}}$. The associated $3\sigma_{pd}$ values are illustrated with dashed red lines. For valid linearization, the $3\sigma_{pd}$ values calculated from the linearized system will be consistent with the Monte Carlo results. This is shown graphically by the red dashed lines mostly encapsulating the the gray lines representing P_D calculated for each Monte Carlo run. The following paragraphs describe the verification results for the RCS models introduced in Section II-B.

Fig. 4 shows the Monte Carlo result for the ellipsoid RCS where $\bar{P}_D$ ranges from near 0 when the radar detection vector points to the front and rear of the aircraft and nearly 0.85 when it points to the side of the aircraft. The variation in P_D is significantly influenced by the shape of the ellipsoid RCS model which is much larger at the sides of the aircraft. Furthermore, the bottom plot of Fig. 4 illustrates over 5% variability in P_D, and that σ_{pd} a strong function of θ_r. Note that the magnitude of σ_{pd} is consistent with the Monte Carlo

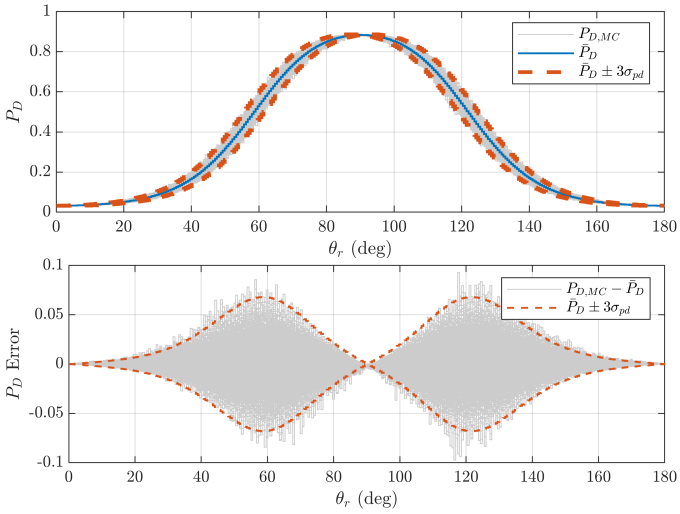

Fig. 4: Monte Carlo analysis results for probability of detection with "medium" level of aircraft state uncertainty over the range $\theta_r = [0,\ 180]$ degrees with the ellipsoid RCS model. The plots show "hair" lines P_D (top) and P_D error (bottom) for each Monte Carlo run and the $3\sigma_{pd}$ approximated with the linearized models.

ensemble statitcs for all azimuth angles and that the azimuth angles associated with the largest σ_{pd} values are the angles where the RCS model and (1) change most rapidly.

Fig. 5 shows similar results for the spikeball RCS. As in the previous case, $\bar{P}_D$ exhibits a strong dependence on the azimuth angle, ranging from close to 0 to nearly 0.9. For several azimuth angles, the variation in P_D is large, approaching $\pm 15\%$, which is due to rapid changes in the RCS and (1) near these angles. As in the case of the ellipsoid, the $3\sigma_{pd}$ values obtained via linearization appropriately encapsulate most of the Monte Carlo ensembles for all radar azimuth angles. At radar azimuth angles of 0, 60, 120, and 180 degrees, the Monte Carlo ensembles become biased due to linearization errors near the sharp corners of the spikeball RCS model and (1) approaching 0. Near these angles, the linear approximation to RCS model presents a bias that influences the estimation of P_D. Regardless of the indicated bias, the Monte Carlo ensembles are mostly encapsulated by the $3\sigma_{pd}$ values calculated from the linearized models at these angles, resulting in a conservative estimate of σ_{pd}. Note that if the sharp corners were sharp outward spikes, the linearization of the RCS model would cause a similar bias where the $3\sigma_{pd}$ values are higher than the extent of the Monte Carlo samples which would represent a conservative approximation of σ_{pd}.

Several important conclusions are drawn from the results of this section. First, the variability of P_D due to uncertainty in aircraft pose is substantial for ellipsoid and spikeball RCS models, $\pm 5\%$ for the former and $\pm 10\%$ for the latter. Second, sharp changes in the RCS with respect to azimuth angle induce a skew in the distribution of P_D about the nominal value. The skew is especially prominent for the case of high state uncertainties. Third, despite the induced skew, he $3\sigma_{pd}$ values predicted by (21) are consistent with the extents of the Monte

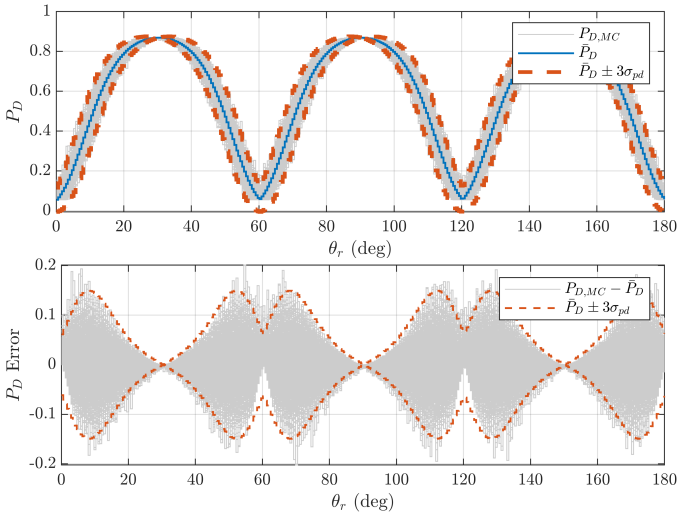

Fig. 5: Monte Carlo analysis results for probability of detection with "medium" level of aircraft state uncertainty over the range $\theta_r = [0,\ 180]$ degrees with the spikeball RCS model. The plots show "hair" lines P_D (top) and P_D error (bottom) for each Monte Carlo run and the $3\sigma_{pd}$ approximated with the linearized models.

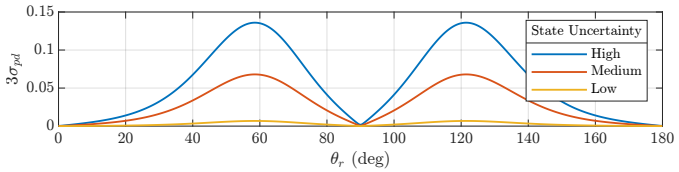

Fig. 6: Probability of detection sensitivity to state uncertainty for the ellipsoid RCS. Each line indicates the $3\sigma_{pd}$ values of the linearized P_D statistics.

Carlo ensembles, yielding conservative bounds for P_D.

B. Sensitivity to State Uncertainty

The results of the previous section served to verify the variation in P_D predicted by (21). This section explores the sensitivity of P_D to state uncertainty using the linearized models. This is illustrated by evaluating $3\sigma_{pd}$ values over a range of θ_r for the two RCS models and the three levels of state uncertainty. Note that the nominal range for each RCS model is the same as in the previous section.

Fig. 6 shows $3\sigma_{pd}$ for the ellipsoid RCS model across a range of θ_r for the three state uncertainty levels. The plot shows that $3\sigma_{pd}$ approaches 0.15 for the high level of state uncertainty. The magnitude of the sensitivity is highly dependent on the radar azimuth angle, θ_r. The magnitude of σ_{pd} is primarily driven by the rate of change of the RCS model and (1) at a given azimuth angle. Fig. 7 shows similar results for the spikeball RCS but $3\sigma_{pd}$ approaches 0.3 for the high level of state uncertainty.

The results in this section show that σ_{pd} varies based on the RCS model, radar azimuth angle θ_r, and the state uncertainty. The σ_{pd} values for the ellipsoid and spikeball RCS models are significant, especially for the medium and high

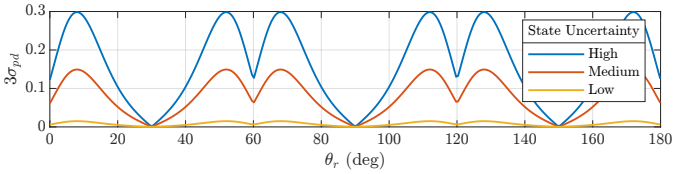

Fig. 7: Probability of detection sensitivity to state uncertainty for the spikeball RCS. Each line indicates the $3\sigma_{pd}$ values estimated by the linearized models.

levels of state uncertainty. This indicates that considering the state uncertainty for the ellipsoid and spikeball RCS models provides significant value, especially for scenarios with large state uncertainty. Failing to consider the state uncertainty in these scenarios will result in detection probabilities that are higher than expected.

V. Conclusion

In planning the path of an aircraft, operators must ensure that the probability of being detected by radar systems stays below mission-specified levels. The probability of detection P_D is commonly considered a deterministic value that is a function of the aircraft pose, radar position, and radar parameters. This approach fails to consider the variability in P_D induced by uncertainty in such parameters. A source of uncertainty in mission planning is in the aircraft pose which is often modeled as a Gaussian random vector with a mean and covariance. This paper presents a method for estimating the variability of P_D due to uncertainty in the aircraft pose.

The method presented in this work provides a first-order approximation of the variations in P_D. This is accomplished by linearizing an expression for P_D with respect to the aircraft pose. The resulting linear model is used to determine the 3σ variability of P_D due to uncertainty in the aircraft pose. As part of the linearization, the necessary partial derivatives are derived for the ellipsoid, and spikeball radar cross section models.

The linearization of P_D with respect to the aircraft state is verified using a Monte Carlo analysis for three levels of aircraft pose uncertainty and the two radar cross section models. Despite small biases present in the Monte Carlo ensemble due to sharp changes in the simple spikeball RCS model, the 3σ values predicted by the linear model appropriately incapsulate the variations in P_D due to uncertainty in the aircraft pose.

The sensitivity of P_D to aircraft pose uncertainty is also explored in this paper. The results show that the magnitude of the 3σ bound is significant for the ellipsoid and simple spikeball RCS models – nearly 0.15 and 0.3, respectively for a high level of state uncertainty. These variations are significant and must be considered in mission planning efforts. Failing to consider the aircraft pose uncertainty will result in detection probabilities that are higher than expected. Mission planners interested in applying the framework presented in this paper must collect the following information:

- Parameters for the RCS model
- Radar parameters c_r and P_{fa}
- Radar position in NED frame

- Aircraft pose and covariance samples along a nominal trajectory

The methods presented in this paper provide a framework for incorporating uncertainty in the aircraft pose into the calculation of the probability of detection. Several extensions to this work may be explored. First, in this work, the radar position and radar parameters are assumed to be known and deterministic quantities. In practice, these values are estimated and have inherent uncertainty. The framework presented in this paper may be extended to incorporate uncertainties in these parameters. Second, the framework in this paper may be applied to a path planner that accounts for the variability of P_D due to uncertainties in the aircraft pose. Third, the current framework utilizes a single-pulse detection model. This may be extended to support multiple-pulse detection to examine the effect of pulse-integration methods and Swerling models for fluctuating targets. Fourth, additional RCS models may be explored.

REFERENCES

[1] N. Ceccarelli, J. J. Enright, E. Frazzoli, S. J. Rasmussen, and C. J. Schumacher, "Micro uav path planning for reconnaissance in wind," in *2007 American Control Conference*, 2007, pp. 5310–5315.

[2] R. Larson, M. Pachter, and M. Mears, "Path Planning by Unmanned Air Vehicles for Engaging an Integrated Radar Network," in *AIAA Guidance, Navigation, and Control Conference and Exhibit*. American Institute of Aeronautics and Astronautics, 2001.

[3] F. Xiao-wei, L. Zhong, and G. Xiao-guang, "Path Planning for UAV in Radar Network Area," in *2010 Second WRI Global Congress on Intelligent Systems*, vol. 3, Dec. 2010, pp. 260–263.

[4] P. T. Kabamba, S. M. Meerkov, and F. H. Z. III, "Optimal Path Planning for Unmanned Combat Aerial Vehicles to Defeat Radar Tracking," *Journal of Guidance, Control, and Dynamics*, May 2012.

[5] M. McFarland, R. Zachery, and B. Taylor, "Motion planning for reduced observability of autonomous aerial vehicles," in *Proceedings of the 1999 IEEE International Conference on Control Applications (Cat. No.99CH36328)*, vol. 1, Aug. 1999, pp. 231–235 vol. 1.

[6] S. Bortoff, "Path planning for UAVs," in *Proceedings of the 2000 American Control Conference. ACC (IEEE Cat. No.00CH36334)*, vol. 1, Jun. 2000, pp. 364–368 vol.1, iSSN: 07431619.

[7] P. Chandler, S. Rasmussen, and M. Pachter, "UAV cooperative path planning," in *AIAA Guidance, Navigation, and Control Conference and Exhibit*. Dever,CO,U.S.A.: American Institute of Aeronautics and Astronautics, Aug. 2000.

[8] M. Pachter and J. Hebert, "Optimal aircraft trajectories for radar exposure minimization," in *Proceedings of the 2001 American Control Conference. (Cat. No.01CH37148)*, vol. 3, Jun. 2001, pp. 2365–2369 vol.3, iSSN: 07431619.

[9] F. Moore, "Radar cross-section reduction via route planning and intelligent control," *IEEE Transactions on Control Systems Technology*, vol. 10, no. 5, pp. 696–700, Sep. 2002.

[10] M. Jun and R. D'Andrea, "Path Planning for Unmanned Aerial Vehicles in Uncertain and Adversarial Environments," in *Cooperative Control: Models, Applications and Algorithms*, ser. Cooperative Systems, S. Butenko, R. Murphey, and P. M. Pardalos, Eds. Boston, MA: Springer US, 2003, pp. 95–110.

[11] X. Sun, C. Cai, J. Yang, and X. Shen, "Route evaluation for unmanned aerial vehicle based on type-2 fuzzy sets," *Engineering Applications of Artificial Intelligence*, vol. 39, pp. 132–145, Mar. 2015. [Online]. Available: https://www.sciencedirect.com/science/article/pii/S0952197614002802

[12] T. Erlandsson and L. Niklasson, "Automatic evaluation of air mission routes with respect to combat survival," *Information Fusion*, vol. 20, pp. 88–98, Nov. 2014. [Online]. Available: https://www.sciencedirect.com/science/article/pii/S1566253513001437

[13] T. Erlandsson, "Route planning for air missions in hostile environments," *The Journal of Defense Modeling and Simulation*, vol. 12, no. 3, pp. 289–303, Jul. 2015, publisher: SAGE Publications. [Online]. Available: https://doi.org/10.1177/1548512914544529

[14] W. Pisano and D. Lawrence, "Autonomous Gust Insensitive Aircraft," in *AIAA Guidance, Navigation and Control Conference and Exhibit*. Honolulu, Hawaii: American Institute of Aeronautics and Astronautics, Aug. 2008. [Online]. Available: https://arc.aiaa.org/doi/10.2514/6.2008-6510

[15] P. G. Savage, *Strapdown analytics*. Maple Plain, Minn.: Strapdown Associates, 2000.

[16] J. Farrell, *Aided Navigation: GPS with High Rate Sensors*, 1st ed. USA: McGraw-Hill, Inc., 2008.

[17] M. S. Grewal, A. P. Andrews, and C. G. Bartone, *Global Navigation Satellite Systems, Inertial Navigation, and Integration*. John Wiley & Sons, Jan. 2020.

[18] J. Marcum, "A statistical theory of target detection by pulsed radar," *IRE Transactions on Information Theory*, vol. 6, no. 2, pp. 59–267, Apr. 1960.

[19] P. Swerling, "Probability of Detection for Fluctuating Targets," RAND Corporation, Tech. Rep., Jan. 1954.

[20] B. R. Mahafza and A. Elsherbeni, *MATLAB Simulations for Radar Systems Design*. CRC Press, Dec. 2003.

[21] D. North, "An Analysis of the factors which determine signal/noise discrimination in pulsed-carrier systems," *Proceedings of the IEEE*, vol. 51, no. 7, pp. 1016–1027, Jul. 1963.

[22] Beard, Randy and McLain, Timothy, *Small Unmanned Aircraft Theory and Practice*. Princeton University Press, 2012.

[23] R. F. v. Schalkwyk and J. C. Smit, "Dynamic Radar Cross Section Measurements of a Full-scale Aircraft for RCS Modelling Validation," Jan. 2017, publisher: IET Digital Library. [Online]. Available: https://digital-library.theiet.org/content/conferences/10.1049/cp.2017.0429

[24] R. E. Weibel, "Safety considerations for operation of different classes of unmanned aerial vehicles in the National Airspace System," Thesis, Massachusetts Institute of Technology, 2005. [Online]. Available: https://dspace.mit.edu/handle/1721.1/30364

APPENDIX A
RADAR CROSS SECTION LINEARIZATION

The following paragraphs will define the partial derivatives of the RCS models presented in Section II-B. The ellipsoid and simple spikeball RCS models are functions of the RCS azimuth and elevation angles from the radar detection vector and the partial derivatives of these expressions are derived as follows

$$\frac{\partial \alpha}{\partial \boldsymbol{x_a}} = \frac{\partial \alpha}{\partial \boldsymbol{\rho_r^b}} \frac{\partial \boldsymbol{\rho_r^b}}{\partial \boldsymbol{x_a}} \tag{35}$$

$$\frac{\partial \phi}{\partial \boldsymbol{x_a}} = \frac{\partial \phi}{\partial \boldsymbol{\rho_r^b}} \frac{\partial \boldsymbol{\rho_r^b}}{\partial \boldsymbol{x_a}} \tag{36}$$

where

$$\frac{\partial \boldsymbol{\rho_r^b}}{\partial \boldsymbol{x_a}} = \begin{bmatrix} \frac{\partial \boldsymbol{\rho_r^b}}{\partial \boldsymbol{p_a^n}} & \frac{\partial \boldsymbol{\rho_r^b}}{\partial \boldsymbol{\Theta_a}} \end{bmatrix}. \tag{37}$$

The partial derivative of the azimuth and elevation angle with respect to $\boldsymbol{\rho_r^b}$ are given by

$$\frac{\partial \alpha}{\partial \boldsymbol{\rho_r^b}} = \begin{bmatrix} \frac{-\rho_{ry}}{\rho_{rx}^2+\rho_{ry}^2} & \frac{\rho_{rx}}{\rho_{rx}^2+\rho_{ry}^2} & 0 \end{bmatrix} \tag{38}$$

$$\frac{\partial \phi}{\partial \boldsymbol{\rho_r^b}} = \begin{bmatrix} \frac{-\rho_{rx}\rho_{rz}}{\gamma} & \frac{-\rho_{ry}\rho_{rz}}{\gamma} & \frac{\sqrt{\rho_{rx}^2+\rho_{ry}^2}}{\rho_{rx}^2+\rho_{ry}^2+\rho_{rz}^2} \end{bmatrix} \tag{39}$$

where

$$\gamma = \left(\rho_{rx}^2 + \rho_{ry}^2 + \rho_{rz}^2\right)\sqrt{\rho_{rx}^2 + \rho_{ry}^2}. \tag{40}$$

The partial derivative of $\boldsymbol{\rho_r^b}$ with respect to the aircraft position in the NED frame is given by

$$\frac{\partial \boldsymbol{\rho_r^b}}{\partial \boldsymbol{p_a^n}} = -T_n^b \tag{41}$$

where T_n^b is defined in (11). The partial derivative of $\boldsymbol{\rho_r^b}$ with respect to the aircraft orientation is given by

$$\frac{\partial \boldsymbol{\rho_r^b}}{\partial \boldsymbol{\Theta_a}} = \begin{bmatrix} \frac{\partial \boldsymbol{\rho_r^b}}{\partial \boldsymbol{\Theta_a}}_{11} & \frac{\partial \boldsymbol{\rho_r^b}}{\partial \boldsymbol{\Theta_a}}_{12} & \frac{\partial \boldsymbol{\rho_r^b}}{\partial \boldsymbol{\Theta_a}}_{13} \\ \frac{\partial \boldsymbol{\rho_r^b}}{\partial \boldsymbol{\Theta_a}}_{21} & \frac{\partial \boldsymbol{\rho_r^b}}{\partial \boldsymbol{\Theta_a}}_{22} & \frac{\partial \boldsymbol{\rho_r^b}}{\partial \boldsymbol{\Theta_a}}_{23} \\ \frac{\partial \boldsymbol{\rho_r^b}}{\partial \boldsymbol{\Theta_a}}_{31} & \frac{\partial \boldsymbol{\rho_r^b}}{\partial \boldsymbol{\Theta_a}}_{32} & \frac{\partial \boldsymbol{\rho_r^b}}{\partial \boldsymbol{\Theta_a}}_{33} \end{bmatrix} \tag{42}$$

where

$$\begin{aligned}
\frac{\partial \boldsymbol{\rho_r^b}}{\partial \boldsymbol{\Theta_a}}_{11} &= -(C\phi_a S\psi_a - C\psi_a S\phi_a S\theta_a)p_{\Delta d} \\
&\quad -(S\phi_a S\psi_a + C\phi_a C\psi_a S\theta_a)p_{\Delta e} && (43)\\
\frac{\partial \boldsymbol{\rho_r^b}}{\partial \boldsymbol{\Theta_a}}_{12} &= C\psi_a S\theta_a p_{\Delta n} - C\psi_a C\theta_a S\phi_a p_{\Delta e} \\
&\quad -C\phi_a C\psi_a C\theta_a p_{\Delta d} && (44)\\
\frac{\partial \boldsymbol{\rho_r^b}}{\partial \boldsymbol{\Theta_a}}_{13} &= (C\phi_a C\psi_a + S\phi_a S\psi_a S\theta_a)p_{\Delta e} \\
&\quad -(C\psi_a S\phi_a - C\phi_a S\psi_a S\theta_a)p_{\Delta d} \\
&\quad +C\theta_a S\psi_a p_{\Delta n} && (45)\\
\frac{\partial \boldsymbol{\rho_r^b}}{\partial \boldsymbol{\Theta_a}}_{21} &= (C\phi_a Cpsi_a + S\phi_a S\psi_a S\theta_a)p_{\Delta d} \\
&\quad +(C\psi_a S\phi_a - C\phi_a S\psi_a S\theta_a)p_{\Delta e} && (46)\\
\frac{\partial \boldsymbol{\rho_r^b}}{\partial \boldsymbol{\Theta_a}}_{22} &= S\psi_a S\theta_a p_{\Delta n} - C\phi_a C\theta_a S\psi_a p_{\Delta d} \\
&\quad -C\theta_a S\phi_a S\psi_a p_{\Delta e} && (47)\\
\frac{\partial \boldsymbol{\rho_r^b}}{\partial \boldsymbol{\Theta_a}}_{23} &= (C\phi_a S\psi_a - C\psi_a S\phi_a S\theta_a)p_{\Delta e} \\
&\quad -(S\phi_a S\psi_a + C\phi_a C\psi_a S\theta_a)p_{\Delta d} \\
&\quad -C\psi_a C\theta_a p_{\Delta n} && (48)\\
\frac{\partial \boldsymbol{\rho_r^b}}{\partial \boldsymbol{\Theta_a}}_{31} &= C\theta_a S\phi_a p_{\Delta d} - C\phi_a C\theta_a p_{\Delta e} && (49)\\
\frac{\partial \boldsymbol{\rho_r^b}}{\partial \boldsymbol{\Theta_a}}_{32} &= C\theta_a p_{\Delta n} + C\phi_a S\theta_a p_{\Delta d} + S\phi_a S\theta_a p_{\Delta e} && (50)\\
\frac{\partial \boldsymbol{\rho_r^b}}{\partial \boldsymbol{\Theta_a}}_{32} &= 0 && (51)
\end{aligned}$$

and

$$\begin{aligned}
\boldsymbol{p_\Delta^n} &= \boldsymbol{p_r^n} - \boldsymbol{p_a^n} && (52)\\
&= \begin{bmatrix} p_{\Delta n} & p_{\Delta e} & p_{\Delta d} \end{bmatrix}^\mathsf{T}. && (53)
\end{aligned}$$

The partial derivatives of the RCS models with respect to α and ϕ are defined in the following subsections.

A. Ellipsoid RCS

The second RCS model is the ellipsoid. The partial derivative of the ellipsoid RCS model with respect to the aircraft state is given by

$$\frac{\partial \sigma_{re}}{\partial \boldsymbol{x_a}} = \frac{\partial \sigma_{re}}{\partial \alpha}\frac{\partial \alpha}{\partial \boldsymbol{x_a}} + \frac{\partial \sigma_{re}}{\partial \phi}\frac{\partial \phi}{\partial \boldsymbol{x_a}}. \tag{54}$$

The partial derivatives of the ellipsoid RCS model with respect to the RCS azimuth and elevation angles are given by

$$\begin{aligned}
\frac{\partial \sigma_{re}}{\partial \alpha} &= \frac{-2\pi(abc)^2 \sin(2\alpha)\kappa}{D^3} && (55)\\
\frac{\partial \sigma_{re}}{\partial \phi} &= \frac{-2\pi(abc)^2 \left(b^2 - a^2\right)\sin(\alpha)^2 \sin(2\phi)}{D^3} && (56)
\end{aligned}$$

where

$$\kappa = a^2\cos(\phi)^2 + b^2\sin(\phi)^2 - c^2 \tag{57}$$

and

$$\mathrm{D} = (a\,\sin\alpha\,\cos\phi)^2 + (b\,\sin\alpha\,\sin\phi)^2 + (c\,\cos\phi)^2\,. \tag{58}$$

B. Simple Spikeball RCS

The third radar cross section model is the simple spikeball. The partial derivative of the simple spikeball RCS model in (15) with respect to the aircraft state is

$$\frac{\partial \sigma_{rs}}{\partial \boldsymbol{x_a}} = \frac{\partial \sigma_{rs}}{\partial \alpha}\frac{\partial \alpha}{\partial \boldsymbol{x_a}} \tag{59}$$

where

$$\frac{\partial \sigma_{rs}}{\partial \alpha} = \frac{n}{2}a_s\cos\left(\frac{n}{2}\alpha\right)\mathrm{sign}\left(a_s\sin\left(\frac{n}{2}\alpha\right)\right). \tag{60}$$

CHAPTER 3

SENSITIVITY OF SINGLE-PULSE RADAR DETECTION TO RADAR STATE UNCERTAINTY

Sensitivity of Single-Pulse Radar Detection to Radar State Uncertainty

Mr. Austin Costley, Dr. Randall Christensen, Dr. Robert C. Leishman, Dr. Greg Droge

***Abstract*—Mission planners for aircraft operating under threat of detection from ground-based radar systems are often concerned with the probability of detection. Current approaches to path planning in such environments consider the radar state (i.e. radar position and parameters) to be deterministic and known. In practice, there is uncertainty in the radar state which induces uncertainty in the probability of detection. This paper presents a method to incorporate the uncertainty of the radar state in a single-pulse radar detection model. The method linearizes the radar detection model with respect to the the radar state and uses the linearized models to estimate, to the first order, the variance of the probability of detection. The results in this paper validate the linearization using Monte Carlo analysis and illustrate the sensitivity of the probability of detection to radar state uncertainty.**

NOMENCLATURE

P_D	Probability of detection
P_{fa}	Probability of false alarm
$\mathcal{S}$	Signal-to-noise ratio
σ_r	Radar cross section (m^2)
R	Range to target (m)
c_r	Culmination constant of radar parameters
$\boldsymbol{x_a}$	Aircraft state vector
$\boldsymbol{p_a^n}$	Aircraft position vector in NED frame
$\boldsymbol{\Theta_a}$	Aircraft Euler angle vector
p_{an}, p_{ae}, p_{ad}	Aircraft position elements in NED frame
ϕ_a, θ_a, ψ_a	Aircraft Euler angles (roll, pitch, yaw)
$\boldsymbol{p_r^n}$	Radar position vector in NED frame
p_{rn}, p_{re}, p_{rd}	Radar position elements in NED frame
a, b, c	Ellipsoid RCS parameters
α	RCS azimuth angle
ϕ	RCS elevation angle
θ_r	Radar detection azimuth angle
ϕ_r	Radar detection elevation angle
C_{aa}	Aircraft pose covariance
σ_{pd}	Standard deviation of P_D

I. INTRODUCTION

Manned and unmanned aircraft are often tasked with operating under threat of detection from ground-based radar systems. Missions executed in such environments include reconnaissance [1], radar counter-measure deployment [2, 3], and combat operations [4]. Planners for these missions are often concerned with the probability of being detected, which is determined by a number of factors. The factors include the aircraft position and orientation (pose), radar position, radar parameters (e.g. power, aperture, noise factor, loss factor, etc.), and the physical characteristics of the aircraft such as the radar cross section (RCS).

The target detection literature provides high-fidelity single-pulse radar detection models which estimate the instantaneous probability of detection given the radar position, radar parameters, and the pose of the detected aircraft. Marcum [5] and Swerling [6] express target detection as a probability for single-pulse and fluctuating target models. Mahafza [7] extends the work by Marcum and Swerling to include considerations for modeling modern radar systems and common RCS models. Most path planning algorithms use simplified radar models that do not attempt to quantify the probability of detection [2, 3, 8–12]. In constrast, Kabamba [4] quantifies the probability of tracking with a logistic function approximation, but the model abstracts away the radar-specific parameters. This paper will use a high-fidelity model from [7] which quantifies the probability of detection as a function of radar parameters such as power, aperture, noise factor, and loss factor.

A common feature of the referenced path planning and radar detection literature [2–16] is that the aircraft pose, radar position, and radar parameters are deterministic and known. However, [17] shows that moderate aircraft pose uncertainty induced significant variability in the probability of detection. The resulting mean and variance of the probability of detection is useful for path planning [15, 16] and error budget analysis [18–20].

The primary contribution of this paper is an extension of the framework developed in [17] to incorporate radar position and parameter uncertainty in the calculation of the probability of detection for a single-pulse radar model. This is accomplished by linearizing the radar detection model with respect to the radar state. The linearized model is used to produce a first-order approximation of the variability of the probability of detection due to uncertainties in the aircraft and radar states. The linearization is validated using Monte Carlo analysis. Futhermote, the sensitivity of the probability of detection to aircraft and radar state uncertainties is illustrated by evaluating the radar detection model with three levels of radar state uncertainty.

The remainder of this paper is organized as follows. The

This work was supported by Air Force Research Laboratory, Wright-Patterson Air Force Base, OH.

A. Costley is with the Electrical and Computer Engineering Department, Utah State University, Logan, UT 84322 USA (e-mail: adcostley@gmail.com)
R. Christensen is with Blue Origin, Kent, WA 98032 USA (e-mail: rchristensen@blueorigin.com)
R. Leishman is with the ANT Center, Air Force Institute of Technology, Wright-Patterson Air Force Base, OH 45433 USA (e-mail: robert.leishman@afit.edu)
G. Droge is with the Electrical and Computer Engineering Department, Utah State University, Logan, UT 84322 USA (e-mail: greg.droge@usu.edu)

radar detection framework presented in [17] is reviewed in Section II. The linearization of the radar detection model with uncertainty in the radar state is derived in Section III. The results of the Monte Carlo and sensitivity analyses are provided in Section IV.

II. Radar Detection Model

The purpose of the radar detection model in this work is to provide an expression for the probability of detection, P_D, as a function of the aircraft pose, radar position, and radar parameters. A common expression for P_D uses Marcum's Q-function [7] which is dependent on the amplitude of the radar sinusoid and contains an integral that does not have a closed form solution. An accepted and accurate approximation to P_D provided by North [21] and used in [7] is

$$P_D \approx 0.5 \times \text{erfc}\left(\sqrt{-\ln P_{fa}} - \sqrt{\mathcal{S}+0.5}\right), \tag{1}$$

where P_{fa} is the probability of false alarm, $\mathcal{S}$ is the signal to noise ratio, and $\text{erfc}(\cdot)$ is the complementary error function given by

$$\text{erfc}(z) = 1 - \frac{2}{\sqrt{\pi}}\int_0^z e^{-\zeta^2} d\zeta. \tag{2}$$

The P_{fa} is considered a constant for a given radar, whereas $\mathcal{S}$ is a function of radar parameters and the pose of the target aircraft. A general expression for the signal-to-noise ratio is given by

$$\mathcal{S} \quad = \quad c_r \frac{\sigma_r}{kR^4}, \tag{3}$$

where k is Boltzmann's constant ($1.38 \times 10^{-23}\ J/^\circ K$), c_r is the consolidated radar constant, R is the range to the target, and σ_r is the RCS. Models for the radar constant, range to the target, and the RCS are provided in the following paragraphs.

The expression for consolidated radar constant depends on the radar type. Mahafza [7] provides an expression for a surveillance radar as

$$c_r = \frac{P_{av} A}{16 T_0 L F} \frac{T_{sc}}{\Omega}, \tag{4}$$

where P_{av} is the average transmitted power, A is the aperture, T_0 is the temperature, T_{sc} is the radar scan time, and Ω is the radar search volume.

Consider the radar detection scenario illustrated in Fig. 1. The range to the target is defined as the 2-norm of the difference between the aircraft and radar positions in the North-East-Down (NED) frame given by

$$R \quad = \quad ||\boldsymbol{p_r^n} - \boldsymbol{p_a^n}||_2. \tag{5}$$

where

$$\boldsymbol{p_r^n} = \begin{bmatrix} p_{rn} & p_{re} & p_{rd} \end{bmatrix}^\intercal \tag{6}$$

and

$$\boldsymbol{p_a^n} = \begin{bmatrix} p_{an} & p_{ae} & p_{ad} \end{bmatrix}^\intercal. \tag{7}$$

The RCS of the target aircraft is a function of the angles that describe the vector from the aircraft to the radar. These angles

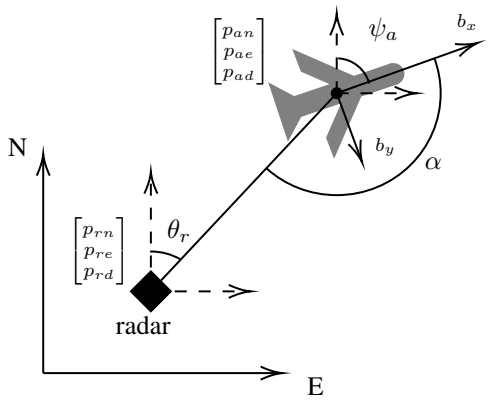

Fig. 1. Graphical representation of the quantities used in the radar detection model.

are referred to as the RCS azimuth angle α and elevation angle ϕ given by

$$\alpha \quad = \quad \arctan\left(\frac{\rho_{ry}}{\rho_{rx}}\right) \tag{8}$$

and

$$\phi \quad = \quad \arctan\left(\frac{\rho_{rz}}{\sqrt{(\rho_{rx})^2 + (\rho_{ry})^2}}\right), \tag{9}$$

where the relative position of the radar in the body frame of the aircraft is given by

$$\boldsymbol{\rho_r^b} = \begin{bmatrix} \rho_{rx} & \rho_{ry} & \rho_{rz} \end{bmatrix}^\intercal. \tag{10}$$

The body frame of the aircraft is defined with the x-axis out the nose of the aircraft, the z-axis out the bottom of the aircraft, and the y-axis out the right wing. The vector $\boldsymbol{\rho_r^b}$ is calculated using the aircraft pose and radar position by

$$\boldsymbol{\rho_r^b} = T_n^b \left(\boldsymbol{p_r^n} - \boldsymbol{p_a^n}\right), \tag{11}$$

where T_n^b is the direction cosine matrix formed by the ZYX Euler angle sequence [22] given by

$$T_n^b = \begin{bmatrix} C\psi_a C\theta_a & -C\phi_a S\psi_a + C\psi_a S\phi_a S\theta_a & S\phi_a S\psi_a + C\phi_a C\psi_a S\theta_a \\ C\theta_a S\psi_a & C\phi_a C\psi_a + S\phi_a S\psi_a S\theta_a & -C\psi_a S\phi_a + C\phi_a S\psi_a S\theta_a \\ -S\theta_a & C\theta_a S\phi_a & C\phi_a C\theta_a \end{bmatrix} \tag{12}$$

where S$\cdot$ and C$\cdot$ are the $\sin(\cdot)$ and $\cos(\cdot)$ functions, and ϕ_a, θ_a, and ψ_a are the Euler angles for the roll, pitch, and yaw of the aircraft, respectively.

As stated previously, the RCS is a function of α and ϕ, but the specific function depends on the chosen RCS model. The framework in [17] provides support for three analytical RCS models – constant, ellipsoid, and simple spikeball. This paper uses the ellipsoid RCS model [4, 7], although a similar derivation can be done for each of the other RCS models. The ellipsoid RCS model represents a 3-dimensional surface given by

$$\sigma_{re} = \frac{\pi\,(abc)^2}{\left((a\,\text{S}\alpha\,\text{C}\phi)^2 + (b\,\text{S}\alpha\,\text{S}\phi)^2 + (c\,\text{C}\alpha)^2\right)^2} \tag{13}$$

where a, b, and c, are the length of the ellipsoid axes. Note that the ellipsoid orientation is aligned with the body frame with the a axis forward, b axis down, and c axis out the right wing.

III. Linearized Probability of Detection

This section describes a method to linearize the radar detection model with respect to the radar position and radar parameters and incorporate the linearized model into the framework in [17] to account for radar state uncertainty. The previous section has shown that P_D is approximated by a nonlinear function of the aircraft pose, radar position, and radar constant c_r. Thus, variability in these quantities induces variability in P_D. Let the radar state be defined as

$$\boldsymbol{x_r} = \begin{bmatrix} \boldsymbol{p_r^n} & c_r \end{bmatrix}^\intercal \tag{14}$$

and the aircraft state be defined as

$$\boldsymbol{x_a} = \begin{bmatrix} \boldsymbol{p_a^n} & \phi_a & \theta_a & \psi_a \end{bmatrix}^\intercal. \tag{15}$$

A first order approximation for the mean and variance of P_D is obtained by linearizing (1) about the nominal aircraft and radar states and applying a Taylor series expansion. The expansion results in the sum of P_D evaluated at the nominal aircraft and radar states ($\bar{\boldsymbol{x}}_{\boldsymbol{a}}$, $\bar{\boldsymbol{x}}_{\boldsymbol{r}}$) with the perturbation of P_D, δP_D, as

$$P_D(\bar{\boldsymbol{x}}_{\boldsymbol{a}} + \delta\boldsymbol{x_a}, \bar{\boldsymbol{x}}_{\boldsymbol{r}} + \delta\boldsymbol{x_r}) \approx P_D(\bar{\boldsymbol{x}}_{\boldsymbol{a}}, \bar{\boldsymbol{x}}_{\boldsymbol{r}}) + \delta P_D \tag{16}$$

where $\delta\boldsymbol{x_a}$ and $\delta\boldsymbol{x_r}$ are perturbations on the aircraft and radar states. The perturbation of P_D, δP_D, is expanded as

$$\begin{aligned} \delta P_D = {} & \frac{\partial P_D}{\partial \mathcal{S}} \left[\frac{\partial \mathcal{S}}{\partial R}\frac{\partial R}{\partial \boldsymbol{x_a}} + \frac{\partial \mathcal{S}}{\partial \sigma_r}\frac{\partial \sigma_r}{\partial \boldsymbol{x_a}} \right]\Bigg|_{\bar{\boldsymbol{x}}_{\boldsymbol{a}}} \delta\boldsymbol{x_a} + \\ & \frac{\partial P_D}{\partial \mathcal{S}} \left[\frac{\partial \mathcal{S}}{\partial R}\frac{\partial R}{\partial \boldsymbol{p_r^n}} + \frac{\partial \mathcal{S}}{\partial \sigma_r}\frac{\partial \sigma_r}{\partial \boldsymbol{p_r^n}} \quad \frac{\partial \mathcal{S}}{\partial c_r} \right]\Bigg|_{\bar{\boldsymbol{x}}_{\boldsymbol{r}}} \delta\boldsymbol{x_r} \qquad (17) \\ \approx {} & A_{Pa}\delta\boldsymbol{x_a} + A_{Pr}\delta\boldsymbol{x_r}. \qquad (18) \end{aligned}$$

Thus, the perturbation can be approximated as a linear combination of perturbations on the aircraft and radar states. The Jacobians A_{Pa} and A_{Pr} have three partial derivatives in common $\left(\frac{\partial P_D}{\partial \mathcal{S}}, \frac{\partial \mathcal{S}}{\partial R}, \frac{\partial \mathcal{S}}{\partial \sigma_r}\right)$. The common partial derivatives and the remaining partial derivatives that define A_{Pa} are derived in [17]. The remaining partial derivatives $\left(\frac{\partial R}{\partial \boldsymbol{p_r^n}}, \frac{\partial \sigma_r}{\partial \boldsymbol{x_r}}, \frac{\partial \mathcal{S}}{\partial c_r}\right)$ are derived in the following paragraphs.

The partial derivative of the range to the aircraft as defined in (5) with respect to the radar state is given by

$$\frac{\partial R}{\partial \boldsymbol{p_r^n}} = \frac{-(\boldsymbol{p_a} - \boldsymbol{p_r})^\intercal}{||\boldsymbol{p_a} - \boldsymbol{p_r}||_2}. \tag{19}$$

The RCS, σ_r, is a function of the RCS azimuth α and elevation ϕ angles so the partial derivative of σ_r with respect to the radar state is expanded to obtain

$$\frac{\partial \sigma_r}{\partial \boldsymbol{p_r^n}} = \frac{\partial \sigma_r}{\partial \alpha}\frac{\partial \alpha}{\partial \boldsymbol{p_r^n}} + \frac{\partial \sigma_r}{\partial \phi}\frac{\partial \phi}{\partial \boldsymbol{p_r^n}}. \tag{20}$$

The partial derivatives of σ_r with respect to α and ϕ $\left(\frac{\partial \sigma_r}{\partial \alpha}, \frac{\partial \sigma_r}{\partial \phi}\right)$ are dependent on the chosen RCS model. For the ellipsoid RCS model [4, 7, 17], these partial derivatives are given by

$$\begin{aligned} \frac{\partial \sigma_{re}}{\partial \alpha} &= \frac{-2\pi(abc)^2 \sin(2\alpha)\kappa}{D^3} \qquad (21) \\ \frac{\partial \sigma_{re}}{\partial \phi} &= \frac{-2\pi(abc)^2 \left(b^2 - a^2\right)\sin(\alpha)^2 \sin(2\phi)}{D^3}, \qquad (22) \end{aligned}$$

where

$$\kappa = a^2\cos(\phi)^2 + b^2\sin(\phi)^2 - c^2 \tag{23}$$

and

$$\mathrm{D} = (a\,\sin\alpha\,\cos\phi)^2 + (b\,\sin\alpha\,\sin\phi)^2 + (c\,\cos\phi)^2\,. \tag{24}$$

The partial derivatives of α and ϕ as defined in (8) and (9) with respect to the radar position are common for all RCS models $\left(\frac{\partial \alpha}{\partial \boldsymbol{p_r^n}}, \frac{\partial \phi}{\partial \boldsymbol{p_r^n}}\right)$ and are expanded as

$$\begin{aligned} \frac{\partial \alpha}{\partial \boldsymbol{p_r^n}} &= \frac{\partial \alpha}{\partial \boldsymbol{\rho_r^b}}\frac{\partial \boldsymbol{\rho_r^b}}{\partial \boldsymbol{p_r^n}} \qquad (25) \\ \frac{\partial \phi}{\partial \boldsymbol{p_r^n}} &= \frac{\partial \phi}{\partial \boldsymbol{\rho_r^b}}\frac{\partial \boldsymbol{\rho_r^b}}{\partial \boldsymbol{p_r^n}}, \qquad (26) \end{aligned}$$

where

$$\begin{aligned} \frac{\partial \alpha}{\partial \boldsymbol{\rho_r^b}} &= \begin{bmatrix} \frac{-\rho_{ry}}{\rho_{rx}^2+\rho_{ry}^2} & \frac{\rho_{rx}}{\rho_{rx}^2+\rho_{ry}^2} & 0 \end{bmatrix} \qquad (27) \\ \frac{\partial \phi}{\partial \boldsymbol{\rho_r^b}} &= \begin{bmatrix} \frac{-\rho_{rx}\rho_{rz}}{\gamma} & \frac{-\rho_{ry}\rho_{rz}}{\gamma} & \frac{\sqrt{\rho_{rx}^2+\rho_{ry}^2}}{\rho_{rx}^2+\rho_{ry}^2+\rho_{rz}^2} \end{bmatrix} \qquad (28) \end{aligned}$$

and

$$\gamma = \left(\rho_{rx}^2 + \rho_{ry}^2 + \rho_{rz}^2\right)\sqrt{\rho_{rx}^2 + \rho_{ry}^2}. \tag{29}$$

The remaining expression is calculated by taking the partial derivative of (11) with respect to $\boldsymbol{p_r^n}$ given by

$$\frac{\partial \boldsymbol{\rho_r^b}}{\partial \boldsymbol{p_r^n}} = T_n^b. \tag{30}$$

Finally, the partial derivative of $\mathcal{S}$ as defined in (3) with respect to the radar constant c_r is given by

$$\frac{\partial \mathcal{S}}{\partial c_r} = \frac{\sigma_r}{kR^4}. \tag{31}$$

The partial derivatives are used to obtain an expression for A_{Pr} as

$$\begin{aligned} A_{Pr} &= \frac{\partial P_D}{\partial \mathcal{S}} \left[\frac{\partial \mathcal{S}}{\partial R}\frac{\partial R}{\partial \boldsymbol{p_r^n}} + \frac{\partial \mathcal{S}}{\partial \sigma_r}\frac{\partial \sigma_r}{\partial \boldsymbol{p_r^n}} \quad \frac{\partial \mathcal{S}}{\partial c_r} \right] \qquad (32) \\ &= \frac{\exp\left(-\left(\sqrt{-\ln P_{fa}} - \sqrt{\mathcal{S}+0.5}\right)^2\right)}{2\sqrt{\pi}\sqrt{\mathcal{S}+0.5}} \\ &\quad \left[\frac{4c_r\sigma_r(\boldsymbol{p_a}-\boldsymbol{p_r})^\intercal}{kR^5||\boldsymbol{p_a}-\boldsymbol{p_r}||_2} + \frac{c_r}{kR^4}\frac{\partial \sigma_r}{\partial \boldsymbol{p_r^n}} \quad \frac{\sigma_r}{kR^4} \right] \qquad (33) \end{aligned}$$

where $\frac{\partial \sigma_r}{\partial \boldsymbol{p_r^n}}$ is determined by (20) for the ellipsoid RCS model.

The purpose of linearizing the radar detection model is to obtain an expression for the variability of P_D due to uncertainties in the aircraft and radar states. The variance of the linearized model is calculated by taking the expectation of $(\delta P_D)^2$ as

$$\begin{aligned} \sigma_{pd}^2 &= E\left[(\delta P_D)^2\right] \qquad (34) \\ &= A_{Pa}C_{aa}A_{Pa}^\intercal + A_{Pr}C_{rr}A_{Pr}^\intercal \qquad (35) \end{aligned}$$

where C_{aa} is the covariance of the aircraft state and C_{rr} is the covariance of the radar state.

TABLE I
PARAMETERS FOR USED IN RESULTS SECTION

Param	Value	Description
a	0.15 m	Ellipsoid RCS forward axis length
b	0.13 m	Ellipsoid RCS side axis length
c	0.21 m	Ellipsoid RCS up axis length
σ_{pa}	10 m	Aircraft position std. dev.
σ_{ang}	1 deg.	Euler angle state std. dev.
L σ_{pr}	10 m	Low radar position std. dev.
M σ_{pr}	100 m	Medium radar position std. dev.
H σ_{pr}	1000 m	High radar position std. dev.
L σ_{cr}	1 $\text{Jm}^2/^\circ\text{K}$	Low radar constant std. dev.
M σ_{cr}	5 $\text{Jm}^2/^\circ\text{K}$	Medium radar constant std. dev.
H σ_{cr}	10 $\text{Jm}^2/^\circ\text{K}$	High radar constant std. dev.
$\bar{\psi}_a$	90 deg.	Nominal aircraft course angle
$\bar{p}_{ad}$	-3 km	Nominal aircraft position - "down" axis
$\bar{\boldsymbol{p}}_{\boldsymbol{r}}^{\boldsymbol{n}}$	$\mathbf{0_{3\times1}}$ m	Nominal radar position vector (NED)
$\bar{c}_r$	167 $\text{Jm}^2/^\circ\text{K}$	Nominal radar constant
P_{fa}	$1.7e^{-4}$	Probability of false alarm

IV. RESULTS

The results of this paper are separated into two sections. First, results are presented to illustrate the validity of the linearization presented in Section III using Monte Carlo analysis. Second, the linearized models are used to illustrate the sensitivity of P_D to variations in the aircraft and radar states. The sensitivity of P_D is examined using a moderate level of aircraft state uncertainty and three levels of radar state uncertainty (Low, Medium, and High). The radar model used in this section is a surveillance radar from [7] and the parameters used to generate the results are provided in Table I.

A. Linearization Validation

The linearization approach described in Section III provides a first order approximation to the variation in P_D due to uncertainty in the aircraft and radar states. The validity of this approximation is dependent on the nominal operating point of the aircraft state $\bar{\boldsymbol{x}}_{\boldsymbol{a}}$ and radar state $\bar{\boldsymbol{x}}_{\boldsymbol{r}}$, the associated state covariances C_{aa} and C_{rr}, and the RCS model.

The linearization is validated using Monte Carlo analysis for a scenario where the nominal radar position is at the origin of the NED frame ($\bar{\boldsymbol{p}}_{\boldsymbol{r}}^{\boldsymbol{n}} = \mathbf{0_{3\times1}}$) and nominal aircraft positions are obtained by rotating the aircraft about the radar at a nominal range. The nominal radar constant value is 167 $\text{m}^2/^\circ\text{K}$ which is obtained from a radar example provided in [7]. In this approach, the aircraft is considered at a series of nominal poses that are perturbed with random samples according to the aircraft state uncertainty level. The radar states are similarly perturbed at the beginning of every Monte Carlo run. The nominal radar state is given by

$$\bar{\boldsymbol{x}}_{\boldsymbol{r}} = \begin{bmatrix} 0 & 0 & 0 & \bar{c}_r \end{bmatrix}^\intercal. \tag{36}$$

The k^{th} nominal aircraft state is given by

$$\bar{\boldsymbol{x}}_{\boldsymbol{a}}[k] = \begin{bmatrix} \bar{\boldsymbol{p}}_{\boldsymbol{a}}^{\boldsymbol{n}} & 0 & 0 & \bar{\psi}_a \end{bmatrix}^\intercal \tag{37}$$

where

$$\bar{\boldsymbol{p}}_{\boldsymbol{a}}^{\boldsymbol{n}} = \begin{bmatrix} R\sin(\theta_r[k]) & R\cos(\theta_r[k]) & \bar{p}_{ad} \end{bmatrix}^\intercal \tag{38}$$

and $\theta_r[k]$ ranges from 0–180 degrees in increments of 0.5 degrees. The nominal range, $R = 500$ km, ensures that P_D is near 0.5 for some values of θ_r given the parameters defined in Table I. The nominal states for the i^{th} Monte Carlo run are perturbed using

$$\boldsymbol{x}_{\boldsymbol{a},\boldsymbol{i}}[k] = \bar{\boldsymbol{x}}_{\boldsymbol{a}}[k] + \boldsymbol{w}_{\boldsymbol{r},\boldsymbol{i}}[k] \tag{39}$$

and

$$\boldsymbol{x}_{\boldsymbol{r},\boldsymbol{i}} = \bar{\boldsymbol{x}}_{\boldsymbol{r}} + \boldsymbol{w}_{\boldsymbol{a},\boldsymbol{i}} \tag{40}$$

where $\boldsymbol{w}_{\boldsymbol{a},\boldsymbol{i}}[k]$ and $\boldsymbol{w}_{\boldsymbol{r},\boldsymbol{i}}$ are sampled as zero-mean Gaussian distributed random vectors with a covariance matrices given by

$$C_{xx} = \begin{bmatrix} \sigma_{pa}\mathbf{I_{3\times3}} & \mathbf{0} \\ \mathbf{0} & \sigma_{ang}\mathbf{I_{3\times3}} \end{bmatrix} \tag{41}$$

and

$$C_{rr} = \begin{bmatrix} \sigma_{pr}\mathbf{I_{3\times3}} & 0 \\ \mathbf{0_{1\times3}} & \sigma_{cr} \end{bmatrix}. \tag{42}$$

The perturbed states are used to calculate $P_D[k]$ using (1) for each $\theta_r[k]$ value. The collection of P_D values over the range of θ_r make up a single Monte Carlo run. The full Monte Carlo analysis in this work consists of 500 runs. In addition to P_D calculated from the perturbed states, $\bar{P}_D$ is calculated using the nominal states, $\bar{\boldsymbol{x}}_{\boldsymbol{a}}$ and $\bar{\boldsymbol{x}}_{\boldsymbol{r}}$.

The first Monte Carlo analysis is performed using the ellipsoid RCS model and the Medium level of radar state uncertainty. Fig. 2 shows the Monte Carlo results for this scenario. The top plot illustrates the P_D values calculated using (1) for each Monte Carlo run, $P_{D,MC}$, and the nominal states, $\bar{P}_D$. The plot also shows upper and lower 3-σ_{pd} values as calculated using the linearized model in (35) which is expected to envelop 99.7% of the Monte Carlo values. The bottom plot illustrates the difference between P_D calculated from the nominal states and P_D calculated using (1) for each Monte Carlo run. Observe that the 3-σ_{pd} values of P_D are nearly 0.1 for $\theta_r \approx 45$ and 135 degrees. This indicates that depending on the value of θ_r, the variability in P_D may increase the detection risk by 0.1. A key aspect to note is that the 3-σ_{pd} values predicted by (35) are consistent with the ensemble statistics of the Monte Carlo runs for all values of θ_r.

Two conclusions are drawn from the results in this section. First, a moderate level of aircraft state uncertainty and Medium level of radar state uncertainty induces substantial variability in P_D (nearly ±0.1 for certain detection angles). Second, the variance of the linearized model is consistent with the extents of the ensemble statistics of the Monte Carlo runs as indicated by Fig. 2.

B. Sensitivity to State Uncertainty

The next set of results illustrate the sensitivity of P_D to uncertainty in the radar state. The first analysis shows the 3-σ variability of P_D due to Low, Medium, and High radar

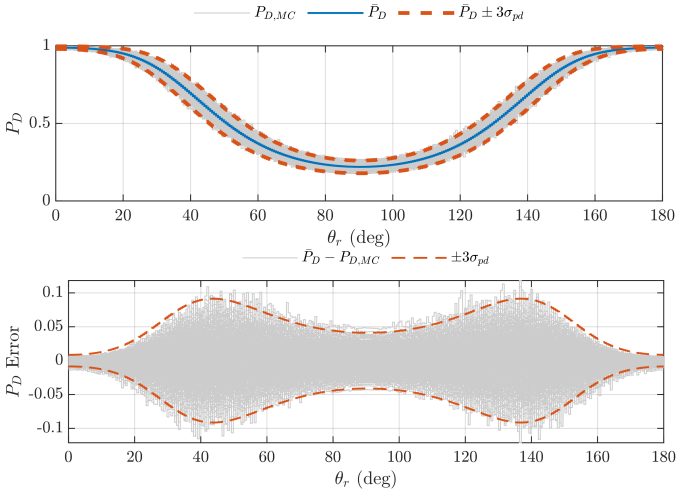

Fig. 2. Monte Carlo analysis results for P_D with "Medium" level of aircraft and radar state uncertainty over the range $\theta_r = [0,\ 180]$ degrees with the ellipsoid RCS model. The plots show "hair" lines for P_D (top) and P_D error (bottom) for each Monte Carlo run and 3-σ_{pd} calculated with the linearized radar model.

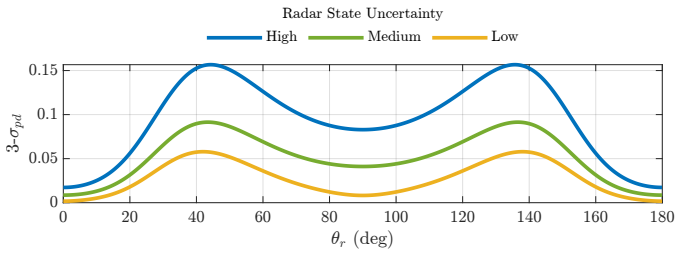

Fig. 3. Sensitivity analysis of P_D for three levels of radar state uncertainty over the range $\theta_r = [0,\ 180]$ degrees with the ellipsoid RCS model and $R = 500$ km. Each line indicates the 3-σ_{pd} value for each level of state uncertainty.

state uncertainty as defined in Table I. The second analysis provides an error budget that illustrates the contribution of each of the four sources of uncertainty (i.e. aircraft position, aircraft orientation, radar position, and radar constant) to the variability of P_D.

The first analysis is accomplished by calculating 3-σ_{pd} using (35) with the nominal aircraft and radar states over a range of θ_r for the three levels of radar state uncertainty. The nominal states were set using the same approach as the Monte Carlo analysis. Fig. 3 shows the results of this analysis where, as expected, the magnitude of 3-σ_{pd} gets larger for higher levels of radar state uncertainty. Note that the magnitude of 3-σ_{pd} is nearly 0.1 for the Medium level of radar state uncertainty and over 0.15 for the High level of radar state uncertainty for $\theta_r \approx 45$ and 135 degrees. This indicates that at certain detection angles, P_D may be 0.1 or 0.15 higher than the nominal value due to Medium to High levels of uncertainty in the aircraft and radar states.

The second analysis provides an error budget for the Medium level of radar state uncertainty. An error budget illustrates the contribution of each source of uncertainty (or error) in a given scenario. This is accomplished by calculating the 3-σ_{pd} value using (35) with the nominal aircraft and

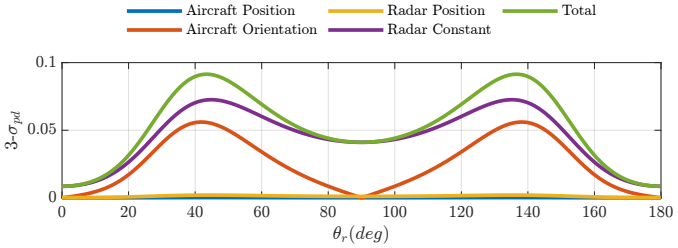

Fig. 4. Error budget for variability of P_D due to four sources of uncertainty for the "Medium" level of radar state uncertainty, ellipsoid RCS model, and $R = 500$ km. Each line indicates the 3-σ uncertainty magnitude as contributed by a given source of uncertainty. The Total line indicates the 3-σ_{pd} magnitude for the scenario.

radar states when a single source of uncertainty is present (or activated) and the other uncertainty sources deactivated. The method is repeated for each source of uncertainty to obtain an expression for 3-σ_{pd} due to each source of uncertainty.

Fig. 4 shows the resulting error budget with four sources of uncertainty (i.e. aircraft position, aircraft orientation, radar position, and the radar constant). The "Total" line shows the magnitude of 3-σ_{pd} with all the error sources active which corresponds to the square root of the sum of the squares of the 3-σ_{pd} values due to each contributing source. The "Total" line is also the same as the "Medium" line from Fig. 3. Observe that the largest contributor to the overall variability in P_D is the uncertainty in the radar constant when σ_{cr} is just under 3% of the nominal radar constant value.

Several conclusions can be drawn from the results presented in this section. The variability of P_D is sensitive to the level of radar state uncertainty for a given scenario and the magnitude of the variability depends on the radar detection angle. The High level of radar state uncertainty induces a 3-σ_{pd} value of over 0.15 for $\theta_r \approx 45$ and 135 degrees. These detection angles are associated with the areas of the ellipsoid RCS model with the largest variability. Uncertainty in the aircraft and radar states has the greatest influence at these detection angles. The contribution of individual error sources to the overall variability in P_D is illustrated in the error budget in Fig. 4. The graph indicates that the variability in P_D is primarily driven by the uncertainty in the radar constant and the orientation of the aircraft. If the mission planner desires to reduce the variability in P_D, attention should first be given to the possibility of reducing uncertainty in the radar constant and improving the estimate of the aircraft orientation.

V. Conclusion

Mission planning for aircraft operating in environments with ground-based radar systems must account for the probability of detection. Several factors influence the probability of detection including aircraft pose, radar position, and radar performance characteristics. Current methods for path planning in radar detection environments consider these factors to be deterministic and known. In practice, these factors are estimated using gathered intelligence and have some uncertainty. The methods presented in this work extend [17] to incorporate uncertainty in the radar state.

The framework in [17] provides a first-order approximation of the variance of P_D due to uncertainties in the aircraft state. This is accomplished by linearizing the radar detection equations with respect to the aircraft state. The methods in this paper extend this framework by linearizing the radar detection equations with respect to the radar state. The linearized equations are used to compute the variability of P_D due to uncertainties in the aircraft and radar states.

The linearization of P_D with respect to the radar states is validated using Monte Carlo analysis for three levels of radar state uncertainty. Two conclusions are drawn from the Monte Carlo analysis. First, the radar state uncertainty induces significant variability in P_D (nearly 0.1 for medium radar state uncertainty). Second, the 3-σ_{pd} values values predicted by the linearized model are consistent with the ensemble statistics for the ellipsoid RCS model indicating valid linearization.

The sensitivity of P_D to state uncertainty is also explored in this paper. The sensitivity analysis shows that the magnitude of the 3-σ_{pd} values from the linearized models are over 0.15 for High radar state uncertainty and the magnitude varies based on the detection angle. An error budget is generated to identify the contributions of each source of uncertainty. The error budget indicates that the uncertainty in the radar constant is the largest contributor to the variability in P_D with a radar constant standard deviation of only 3% of the nominal value.

The results in this paper indicate that the linearization is valid and the incorporation of the radar state uncertainty has a significant influence on the variability of P_D. Failing to incorporate uncertainty in the radar state will result in detection probabilities that are higher than expected.

REFERENCES

[1] N. Ceccarelli, J. J. Enright, E. Frazzoli, S. J. Rasmussen, and C. J. Schumacher, "Micro uav path planning for reconnaissance in wind," in *2007 American Control Conference*, 2007, pp. 5310–5315.

[2] R. Larson, M. Pachter, and M. Mears, "Path Planning by Unmanned Air Vehicles for Engaging an Integrated Radar Network," in *AIAA Guidance, Navigation, and Control Conference and Exhibit*. American Institute of Aeronautics and Astronautics, 2001.

[3] F. Xiao-wei, L. Zhong, and G. Xiao-guang, "Path Planning for UAV in Radar Network Area," in *2010 Second WRI Global Congress on Intelligent Systems*, vol. 3, Dec. 2010, pp. 260–263.

[4] P. T. Kabamba, S. M. Meerkov, and F. H. Zeitz, "Optimal Path Planning for Unmanned Combat Aerial Vehicles to Defeat Radar Tracking," *Journal of Guidance, Control, and Dynamics*, vol. 29, no. 2, pp. 279–288, Mar. 2006. [Online]. Available: https://arc.aiaa.org/doi/10.2514/1.14303

[5] J. Marcum, "A statistical theory of target detection by pulsed radar," *IRE Transactions on Information Theory*, vol. 6, no. 2, pp. 59–267, Apr. 1960.

[6] P. Swerling, "Probability of Detection for Fluctuating Targets," RAND Corporation, Tech. Rep., Jan. 1954.

[7] B. R. Mahafza and A. Elsherbeni, *MATLAB Simulations for Radar Systems Design*. CRC Press, Dec. 2003.

[8] S. Bortoff, "Path planning for UAVs," in *Proceedings of the 2000 American Control Conference. ACC (IEEE Cat. No.00CH36334)*, vol. 1, Jun. 2000, pp. 364–368 vol.1, iSSN: 0743-1619.

[9] P. Chandler, S. Rasmussen, and M. Pachter, "UAV cooperative path planning," in *AIAA Guidance, Navigation, and Control Conference and Exhibit*. Dever,CO,U.S.A.: American Institute of Aeronautics and Astronautics, Aug. 2000.

[10] M. Pachter and J. Hebert, "Optimal aircraft trajectories for radar exposure minimization," in *Proceedings of the 2001 American Control Conference. (Cat. No.01CH37148)*, vol. 3, Jun. 2001, pp. 2365–2369 vol.3, iSSN: 0743-1619.

[11] F. Moore, "Radar cross-section reduction via route planning and intelligent control," *IEEE Transactions on Control Systems Technology*, vol. 10, no. 5, pp. 696–700, Sep. 2002.

[12] M. McFarland, R. Zachery, and B. Taylor, "Motion planning for reduced observability of autonomous aerial vehicles," in *Proceedings of the 1999 IEEE International Conference on Control Applications (Cat. No.99CH36328)*, vol. 1, Aug. 1999, pp. 231–235 vol. 1.

[13] M. Jun and R. D'Andrea, "Path Planning for Unmanned Aerial Vehicles in Uncertain and Adversarial Environments," in *Cooperative Control: Models, Applications and Algorithms*, ser. Cooperative Systems, S. Butenko, R. Murphey, and P. M. Pardalos, Eds. Boston, MA: Springer US, 2003, pp. 95–110.

[14] Q. Xu, J. Ge, T. Yang, and X. Sun, "A trajectory design method for coupling aircraft radar cross-section characteristics," *Aerospace Science and Technology*, vol. 98, p. 105653, Mar. 2020. [Online]. Available: https://linkinghub.elsevier.com/retrieve/pii/S1270963819304183

[15] A. Bry and N. Roy, "Rapidly-exploring random belief trees for motion planning under uncertainty," *Proceedings - IEEE International Conference on Robotics and Automation*, pp. 723–730, 2011.

[16] L. Blackmore, M. Ono, and B. C. Williams, "Chance-Constrained Optimal Path Planning With Obstacles," *IEEE Transactions on Robotics*, vol. 27, no. 6, pp. 1080–1094, Dec. 2011.

[17] A. Costley, R. Christensen, G. Droge, and R. C. Leishman, "Sensitivity of single-pulse radar detection to aircraft pose uncertainties," *IEEE Transactions on Aerospace and Electronic Systems*, under review, available in preprint at https://arxiv.org/abs/2201.06727.

[18] P. S. Maybeck, *Stochastic Models, Estimation, and Control*. New York: Navtech Book and Software Store, 1994, vol. 1.

[19] J. Farrell, *Aided Navigation: GPS with High Rate Sensors*, 1st ed. USA: McGraw-Hill, Inc., 2008.

[20] R. Christensen, G. Droge, and R. Leishman, "A closed-loop linear covariance framework for vehicle path planning in an uncertain obstacle field," 2021.

[21] D. North, "An Analysis of the factors which determine signal/noise discrimination in pulsed-carrier systems," *Proceedings of the IEEE*, vol. 51, no. 7, pp. 1016–1027, Jul. 1963.

[22] Beard, Randy and McLain, Timothy, *Small Unmanned Aircraft Theory and Practice*, 2012.

CHAPTER 4

ANALYTICAL AIRCRAFT STATE AND IMU SIGNAL GENERATOR FROM SMOOTHED REFERENCE TRAJECTORY

Analytical Aircraft State and IMU Signal Generator from Smoothed Reference Trajectory

Mr. Austin Costley, Dr. Randall Christensen, Dr. Robert C. Leishman, Dr. Greg Droge

***Abstract*—Generating aircraft position, velocity, and attitude along a reference trajectory is useful in many path and mission planning applications. In applications simulating an inertial navigation system the body-frame accelerations and angular rates are also required. This work presents a method for generating a smoothed continuous-curvature reference trajectory from a series of waypoints using line, arc, clothoid, and Fermat spiral segments in a fillet smoothing framework. The geometry of the segments are used to generate the position, velocity, and attitude of an aircraft following the reference trajectory. A primary contribution of this work is the use of the path geometry, coordinated turn model, and curvilinear motion theory to obtain analytical solutions for the body-frame accelerations and angular rates of the aircraft along the reference trajectory.**

NOMENCLATURE

ψ_Δ	Course angle change at waypoint
k, ψ	Path curvature and course angle
x_0, y_0, ψ_0, k_0	Initial position, course angle, and curvature of path
ρ	Turn direction of path (1 left,-1 right)
θ	Polar angle for arc and Fermat segments
r	Radius of arc segment
s	Length of segment or along segment
σ_c	Curvature rate of clothoid segments
$\theta_{k_{max}}$	Polar angle associated with maximum curvature of Fermat segment
c	Shaping parameter of Fermat segment
$\boldsymbol{e_n}, \boldsymbol{e_t}$	Unit vectors normal and tangent to path
$\boldsymbol{v}, \boldsymbol{a}$	Velocity and acceleration vectors.
R_n^b	Rotation matrix from navigation frame to body frame
$\boldsymbol{g^n}$	Gravity vector in the navigation frame
x_t, y_t	Transition point between segments
x_m, y_m	Midpoint of arc segment
d	Attachment distance from waypoint to start of first transition segment
x_c, y_c	Center point of arc segment
k_{max}, k'_{max}	Maximum curvature and maximum curvature rate per unit length
ϕ_a, ϕ_f	Central angle of arc and Fermat segments
$\boldsymbol{a^n}$	Acceleration in the navigation frame
ϕ_e, θ_e, ψ_e	Euler angles for roll, pitch, and yaw
p, q, r	Body frame angular rates

This work was supported by Air Force Research Laboratory, Wright-Patterson Air Force Base, OH.

A. Costley is with the Electrical and Computer Engineering Department, Utah State University, Logan, UT 84322 USA (e-mail: austin.costley@usu.edu)
R. Christensen is with the Electrical and Computer Engineering Department, Utah State University, Logan, UT 84322 USA (e-mail: randall.christensen@usu.edu)
R. Leishman is with the ANT Center, Air Force Institute of Technology, Wright-Patterson Air Force Base, OH 45433 USA (e-mail: robert.leishman@afit.edu)
G. Droge is with the Electrical and Computer Engineering Department, Utah State University, Logan, UT 84322 USA (e-mail: greg.droge@usu.edu)

I. INTRODUCTION

An objective for the mission and path planning of unmanned aerial vehicles (UAVs) is to determine a flyable path that meets mission requirements. The characteristics of a flyable path are determined by the capabilities of the aircraft. The mission requirements vary based on the application, such as path planning in contested environments to avoid detection [1], reconnaissance missions where the aircraft attitude determines sensor coverage [2], and obstacle avoidance [3].

Candidate paths generated by the path planner are assessed based on mission requirements. The path assessment often consists of evaluating functions of the aircraft pose (i.e. position and orientation) and sensor measurements along the path. This work presents a method called ASG for generating analytical aircraft state and inertial measurement unit (IMU) signals along smoothed candidate paths. The aircraft states and IMU measurements will be calculated using path segment geometry, a coordinated turn assumption [4], and curvilinear motion theory [5].

An important aspect of mission and path planning for UAVs is to account for uncertainty during the operation. Uncertainties exist in three components in planning, namely, vehicle position and orientation, environmental, and vehicle motion uncertainties. Path planning techniques often model some or all of these uncertainties to determine an optimal path [3, 6]. In this work, a fixed-wing UAV with an inertial navigation system (INS) [7] is considered. The propagation of the state estimates and uncertainty of an INS is dependent on measurements from a strapdown IMU [8]. Thus, a path planning algorithm considering the uncertainty of such a system would require estimating aircraft states and the associated IMU measurements along the candidate path.

IMU measurement generation is used in a variety applications. Among the most popular applications are trajectory reconstruction [9, 10], trajectory generation [7, 11, 12], and simulation [4, 13]. While there is significant overlap between these classifications, the chosen application typically determines the information that is available to generate the IMU measurements. For example, the trajectory reconstruction application typically reconstructs a trajectory using recorded flight data. In contrast, the simulation application can obtain acceleration and angular rates directly from the integration of

aircraft dynamics. The trajectory generation application is the most relevant for the purposes of this work.

Trajectory generation takes a series of aircraft poses and calculates expressions for the accelerations and angular rates experienced by the aircraft. These quantities can then be used to generate IMU signals along the path. Most approaches to trajectory generation rely on numerical derivatives of lower-order states to calculate accelerations and angular rates [7, 11–13]. The numerical derivative is sufficiently accurate for small sampling times, however, the accuracy degrades with large sampling times. The large sampling times are often desired in path planning to reduce the computational burden of evaluating path validity. The primary contribution of this work is ASG, a method for analytically generating aircraft states and IMU signals using path segment geometry and a coordinated turn model. The analytical approach avoids numerical derivatives and is stable for large sampling times.

The first stage of the ASG method generates a smoothed reference trajectory from a piecewise linear candidate path (or series of waypoints). The piecewise linear path is not flyable for a fixed-wing UAV due to the discontinuities in course angle. The piecewise linear path can be converted to a flyable path using a path smoothing algorithm [14, 15]. This work will use a fillet corner smoothing algorithm that converts the piecewise linear path into a flyable path that maintains curvature continuity. The corner smoothing approach described in this work is not a novel contribution but a description of the approach is provided in Section III for completeness and reproducibility. The corner smoothing approaches used in this work were chosen because the resulting path consists of a series of segments that have analytical solutions for position, course angle, and curvature.

The path segments generated by the path smoothing algorithm are lines, arcs, and transition segments. The transition segments are used to connect the lines and arcs and maintain continuity in course angle and curvature. The first transition segment is the clothoid, which provides a linearly changing curvature per unit length [16]. A drawback to the clothoid curve is the dependence on the Fresnel Integrals that do not have a closed form solution, however, accurate approximations exist and can be used to simplify the computation [17]. The second transition segment is the Fermat Spiral [18], which avoids the costly computation of the Fresnel Integrals while maintaining continuous curvature. This work describes an algorithm for generating 3 types of smoothed paths (Arc Fillet, Clothoid Fillet, and Fermat Fillet) parameterized by a maximum curvature and maximum curvature rate. The smoothed path is then used to obtain analytical expressions for the aircraft state and IMU measurements along the candidate path.

The ASG method generates and samples the smooth reference trajectory and analytically generates IMU measurements. The novel IMU measurement generation approach is compared with a third party open-source software package based on Matlab code provided with [7], by Paul Groves. The software package provides many utilities for INS implementations. In particular, this work uses a method for generating IMU signals given position, velocity, and attitude samples. The IMU measurements generated by the ASG method are compared with those generated from the Groves method. The comparison shows agreement between the two methods. Furthermore, the ASG method provides greater accuracy as the step time is increased because it has analytical solutions for the path geometry instead of relying on discrete derivatives.

The next section describes background information that is used throughout this work. Section III presents the corner smoothing algorithm that converts a series of waypoints to a path of continuous course angle. The path segment definitions (see Section II-B) are used to determine the position and course angle of the aircraft. Section IV describes a method for determining the roll, pitch, and body-frame accelerations and angular rates of the aircraft assuming straight-and-level flight during straight line segments, and a coordinated turn for transition segments and arcs. Finally, Section V provides results for the ASG method that show the resulting aircraft states and that the accuracy of the IMU measurements is maintained for large time steps.

II. Background

This section presents background information used throughout this work. Section II-A describes the notation. Section II-B defines the segment types used in the corner smoothing algorithm. Finally, accelerations and angular rates along the smoothed path are determined by curvilinear motion theory which is discussed in Section II-C.

A. Notation

In this work, curvature rate refers to the derivative of curvature with respect to path length, s, thus the following convention will be used for brevity

$$\frac{dk}{ds} = k' \tag{1}$$

when the derivative is taken with respect to time, the standard dot notation will be used, $\dot{k}$.

Vectors in this work will be expressed in bold face such that $\boldsymbol{v} = \begin{bmatrix} v_x & v_y & v_z \end{bmatrix}^T$ for a vector in Cartesian coordinates.

This work will maintain three frames of reference in which vector quantities may be expressed, namely, inertial, i, body, b, and the Navigation or North-East-Down (NED), n. The frame in which a vector is expressed will be indicated by the superscript so the velocity vector in the NED frame would be expressed as $\boldsymbol{v}^n = \begin{bmatrix} v_n & v_e & v_d \end{bmatrix}^T$.

The cross product matrix is used throughout this work and will be given by

$$\Omega = [\boldsymbol{\omega}\times] = \begin{bmatrix} 0 & -\omega_z & \omega_y \\ \omega_z & 0 & -\omega_x \\ -\omega_y & \omega_x & 0 \end{bmatrix}. \tag{2}$$

B. Corner Smoothing Segment Definitions

There is a significant amount of literature on the subject of corner smoothing [14, 15]. As the name suggests, corner smoothing takes a corner made from the connection point of two straight path segments and generates a curved segment to

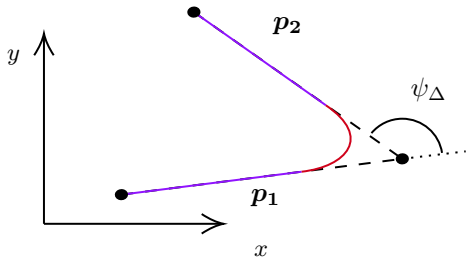

Fig. 1. Corner smoothing example where a two segment piece-wise linear path is smoothed to create path with continuous course angle and curvature. The entry vector is shown as $\boldsymbol{p_1}$, the exit vector is shown as $\boldsymbol{p_2}$, and the course angle change is expressed as ψ_Δ.

transition from the first straight segment to the second straight segment. Fig. 1 shows an example of a two segment piece-wise linear path with a smoothed turn.

The corner smoothing algorithm in this work will output a series of path segments, including straight lines, maximum curvature (minimum turn radius) arcs, and transition segments with changing curvature. The transition segments that will be used in this work are clothoid and Fermat spiral segments. For a given corner, the algorithm will generate two or three smoothing segments depending on the sharpness of the turn. A sharp turn will require three segments (transition segment, maximum curvature arc, transition segment). Whereas a gradual turn will only require two transition segments to smooth the corner. The following subsections define expressions to determine the Cartesian positions (x, y), course angle (ψ), and curvature (k) along each of the path segment types.

1) Line: The first segment type is a line which is defined by

$$\begin{aligned} x(s) &= x_0 + s\cos(\psi_0) && (3)\\ y(s) &= y_0 + s\sin(\psi_0) && (4)\\ \psi &= \psi_0 && (5)\\ k &= 0 && (6) \end{aligned}$$

where s is the length along the segment, and ψ_0 is the initial segment angle.

2) Arc: The arc is a continuous curvature segment. In the smoothing application, the arc will be parameterized by the maximum curvature (k_{max}) attainable by the aircraft. The expressions that define the arc are parameterized by the polar angle, θ, and are given by

$$\begin{aligned} x(\theta) &= x_0 - \rho r\sin(\psi_0) + \rho\cos(\theta) && (7)\\ y(\theta) &= y_0 + \rho r\cos(\psi_0) + \rho\sin(\theta) && (8)\\ \psi(\theta) &= \psi_0 + \rho\theta && (9)\\ k &= \frac{\rho}{r} && (10) \end{aligned}$$

where r is the radius of the arc (the inverse of curvature), and ρ indicates the direction of travel where

$$\rho = \begin{cases} 1, & \text{counter-clockwise (left) turn} \\ -1, & \text{clockwise (right) turn.} \end{cases} \quad (11)$$

The polar angle, θ, is related to the length on the path by the arc length formula $s = r\theta$. Thus, the arc can be sampled at a specified arc length interval by computing the associated polar angle interval and applying the equations above. Note that the convention employed here is that $\theta = 0$ is associated with the point on the curve where $\psi = \frac{\pi}{2}$.

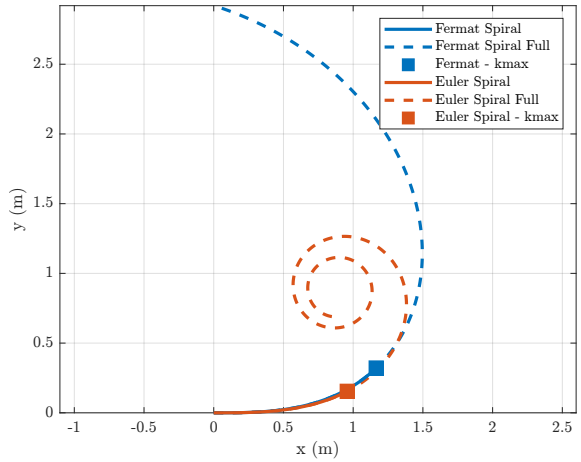

Fig. 2. Euler spiral and Fermat spiral with $\psi_0 = \frac{\pi}{2}$, $k_0 = 0$. The curvature rate for the Euler spiral is $\sigma_c = 1$ and Fermat Spiral has a maximum curvature of 1 $\frac{1}{m}$. The square markers on each line indicate the location where the curvature of the segment is equal to one and the solid segments (before the markers) show the part of the segments used in the path smoothing algorithm.

3) Clothoid: A clothoid or Euler spiral is a path segment whose curvature varies linearly by segment length [19]. The position along the clothoid segment is determined by computing the Fresnel Integrals given by

$$x = C(s) = x_0 + \int_0^s \cos(0.5\sigma_c\xi^2 + k_0\xi + \psi_0)d\xi \quad (12)$$

$$y = S(s) = y_0 + \int_0^s \sin(0.5\sigma_c\xi^2 + k_0\xi + \psi_0)d\xi \quad (13)$$

where s is the length along the clothoid segment, ψ_0 is the initial segment angle, k_0 is the initial segment curvature, x_0 and y_0 represent the starting point of the segment, and σ_c is the curvature rate of the clothoid segment. A primary challenge when working with clothoids is that the Fresnel Integrals do not have a closed form solution so numerical solutions are required to compute positions along the path. However, there are numerous methods [14, 20, 21] for computing accurate approximations to these equations that help mitigate this drawback.

The course angle of a clothoid segment changes quadratically by segment length as given by

$$\psi(s) = \psi_0 + k_0 s + 0.5\sigma_c s^2. \quad (14)$$

Finally, the curvature of the clothoid segment is given by

$$k(s) = k_0 + \sigma_c s. \quad (15)$$

This shows the linear relationship between path length and curvature. An example of a Euler spiral is shown in Fig. 2 for a segment that is 5 meters long, has an initial segment angle and initial curvature of zero, and a curvature rate of one.

4) Fermat Spiral: Another spiral that has been investigated for corner smoothing is the Fermat spiral [18]. The Fermat spiral is an interesting corner smoothing candidate as it provides many of the benefits of the clothoid but avoids the integral computation used to compute the positions along the curve. The curve is parameterized in a polar coordinate system as $r = c\sqrt{\theta}$, where the c parameter can be used to modify the curve characteristics and θ is the polar angle. Converting the curve to Cartesian coordinates results in

$$x(\theta) = x_0 + c\sqrt{\theta}\cos(\rho\theta + \psi_0) \quad (16)$$
$$y(\theta) = y_0 + c\sqrt{\theta}\sin(\rho\theta + \psi_0). \quad (17)$$

The curve is shown in Fig. 2 where it can be noted that curvature does not monotonically increase as the polar angle increases, instead, the curvature increases to a maximum and then decreases until settling at a nearly constant value. The curvature is given by the non-linear equation

$$k(\theta) = \frac{1}{c}\frac{2\sqrt{\theta}\left(4\theta^2+3\right)}{\left(4\theta^2+1\right)^{\frac{3}{2}}}. \quad (18)$$

Fig. 3 shows the curvature of the Fermat spiral for a quarter of a rotation of the polar angle. The figure shows that there is a single maximum for $\theta > 0$. The value of the polar angle at which the maximum curvature is achieved at

$$\theta_{k_{max}} = \sqrt{\frac{\sqrt{7}}{2} - \frac{5}{4}} \approx 0.26995 \quad (19)$$

which is independent of the shaping parameter, c. Beyond $\theta_{k_{max}}$ the curvature decreases. This may appear to be a drawback for using this type of segment in corner smoothing, however, in this application, the polar angle is restricted to the range of $0 < \theta < \theta_{k_{max}}$ so the curvature is monotonically increasing along the transition segment.

The last curve property of interest is the course angle which is given by

$$\psi(\theta) = \theta + \arctan(2\theta). \quad (20)$$

For the corner smoothing application, it is important to define equations for a reflected segment that starts at an arbitrary point along the segment and tracks back to the start of the segment. This operation is more involved for a Fermat Spiral segment than the other segments defined in this section so it will receive special attention here. The position equation for the reflected Fermat Spiral is parameterized by the curve end point (x_{end}, y_{end}), and course at the end of the segment ψ_{end} and is given by

$$x(\theta) = x_{end} + c\sqrt{\theta_{end}-\theta}\cos(\rho(\theta-\theta_{end}) + \psi_{end}) \quad (21)$$
$$y(\theta) = y_{end} + c\sqrt{\theta_{end}-\theta}\sin(\rho(\theta-\theta_{end}) + \psi_{end}) \quad (22)$$

and θ_{end} is the polar angle at the end of the reflected Fermat Spiral segment.

Lekkas et al. [18], show how the shaping parameter, c, can be set such that the maximum curvature of the segment is equal to the maximum curvature of the aircraft. This is accomplished by solving (18) and using $\theta = \theta_{k_{max}}$ and $k(\theta_{k_{max}}) = k_{max}$. Then an expression for c is given by

$$c = \frac{1}{k_{max}}\frac{2\sqrt{\theta_{k_{max}}}\left(4\theta_{k_{max}}^2+3\right)}{\left(4\theta_{k_{max}}^2+1\right)^{\frac{3}{2}}} \quad (23)$$

which will result in a scaled curve that reaches a maximum curvature of k_{max}. Thus, the Fermat spiral can be parameterized to respect the same maximum curvature constraint used in the clothoid smoothing implementation.

One drawback to using the Fermat spiral for corner smoothing is that the length of the path is given by

$$s = c\sqrt{2}\int_0^{\theta_{k_{max}}} \sqrt{1+4\theta^2}\,d\theta \quad (24)$$

which does not have a closed form solution. In [18] the length of a Fermat segment is expressed as a hyper-geometric function with guaranteed convergence over the domain of interest. Thus, in implementation, the computational cost of (24) can be mitigated using a lookup table or an iterative solution to the hyper-geometric function with some convergence criteria.

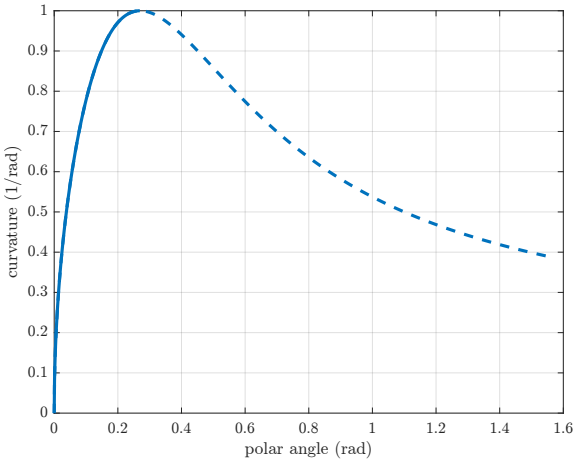

Fig. 3. Curvature of Fermat spiral for a quarter of a rotation of the polar angle with a maximum curvature of 1 $\frac{1}{m}$. The solid line shows the portion of the spiral that will be used in the transition segment. The curvature decreases after the point of maximum curvature.

C. Curvilinear Motion Theory

Curvilinear motion theory defines the motion of a particle along a curved path [5]. Properties of this theory will be used to relate the geometry of the path with the aircraft state vector. The velocity and acceleration along a curved path is given by

$$\boldsymbol{v} = \dot{s}\boldsymbol{e}_t \quad (25)$$

and

$$\boldsymbol{a} = \ddot{s}\boldsymbol{e}_t + \dot{s}\dot{\psi}\boldsymbol{e}_n \quad (26)$$

where $\boldsymbol{e}_t$ and $\boldsymbol{e}_n$, are the tangent and normal vectors, and $\dot{\psi}$ is the angular rate of the path.

TABLE I
PATH SMOOTHING METHOD COMPARISON OF COURSE ANGLE AND CURVATURE CONTINUITY AND RESPECTING LIMITS ON CURVATURE AND CURVATURE RATE (✓= YES, - = NO)

	Continuous		Respect	
Method	ψ	k	k_{max}	k'_{max}
Arc Fillet	✓	-	✓	-
Clothoid Fillet	✓	✓	✓	✓
Fermat Fillet	✓	✓	✓	-

III. CORNER SMOOTHING

In the first stage of the aircraft state generator presented in this work, a piece-wise linear path is converted into a smooth path with continuous course angle or curvature. In the case of continuous curvature, a limit on curvature and curvature rate can be imposed to ensure that the path will be flyable by a specific aircraft. In this way, the physical limitations of the aircraft can be considered and the resulting states can more accurately reflect the behavior of the aircraft.

This section describes three methods for smoothing a piece-wise linear path 1) Arc Fillet, 2) Clothoid Fillet, and 3) Fermat Fillet. Each of these methods perform corner smoothing at every way-point in the path. The resulting path will consist of a series of straight line, arc, and transition segments with varying curvature. This section is particularly useful for a person in the navigation field that may be unfamiliar with corner smoothing algorithms because it provides a unified framework for three methods used in the path planning field.

The path smoothing algorithms presented in this section assume that the spacing between the way-points is sufficiently large enough to perform the indicated corner smoothing method. For example, if the start or end way-point in Fig. 1 was closer to the corner point than the connection between the straight path and the smoothing arc, then the algorithms presented here would not be sufficient.

The first path smoothing approach presented in this section is the Arc Fillet method where a maximum curvature segment is used to connect two straight segments. This method has continuous course angle but has discontinuous path curvature. The second is the Clothoid Fillet method where clothoid segments are used to smooth the corners or, where needed, transition to a k_{max} segment. This method has continuous curvature and course angle and respects limits on curvature and curvature rate. The third is the Fermat Fillet method which is similar to the Clothoid Fillet method but Fermat spiral segments are used in place of clothoid segments. This method has continuous curvature and course angle and respects limits on curvature, however, it is not guaranteed to respect limits on curvature rate. These properties are summarized in Table I.

The three approaches presented in this section iterate through the corners in the path and compute a series of path segments that represent the resulting smooth path. The sharpness of the corner and positions of the way-points before and after the corner are required to determine the smoothing segments. The position of the way-points is provided to the algorithm. The sharpness of the corner is represented by the change of course angle, ψ_Δ, required to transition from the entry segment to the exit segment. The ψ_Δ quantity can be computed by expressing the entry and exit segments as vectors ($\boldsymbol{p_1}$ and $\boldsymbol{p_2}$ from Fig. 1) and using properties of the dot product to determine the angle between the vectors. Another important quantity for each corner is the turn direction, ρ, which is determined using the sign of the cross product of the two vectors. The sign convention for ρ is given in (11).

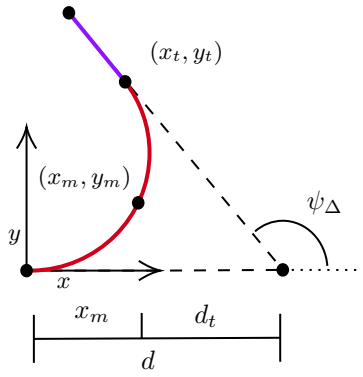

Fig. 4. Arc Fillet example where the origin for the plot is at the connection point along the straight segment entering the way-point and the initial course angle for the arc matches the course angle of the entering segment.

A. Arc Fillet

The Arc Fillet method smooths a corner at a way-point by adding a circular arc of maximum curvature (k_{max}) that transitions from the first straight segment to the other. The arc segment is parameterized by the radius, $r = 1/k_{max}$, and the arc length, $s = r\psi_\Delta$, as discussed in Section II-B2. Then (8) is used with $\theta = \psi_\Delta$ to determine the end point, (x_t, y_t), and the midpoint, (x_m, y_m), of the arc. The distance along the x-axis from the midpoint of the arc is computed geometrically as

$$d_t = \left| \frac{y_m}{\tan^{-1}\left(\frac{\pi - \psi_\Delta}{2}\right)} \right| \tag{27}$$

and the distance from the way-point to the connection point of the arc on the first straight segment is given by

$$d = d_t + x_m. \tag{28}$$

This distance is used to determine the connection point for the arc segment on the first straight segment. Fig. 4 shows the geometry of the Arc Fillet method and includes a graphical representation of x_m and d_t.

B. Clothoid Fillet

The Clothoid Fillet method uses clothoid segments to connect the straight segments and arcs while maintaining continuous curvature. Using clothoid segments to generate continuous curvature paths is well documented in [22]. This section will describe the specific application of smoothing corners using a clothoid fillet method within the unified framework of the current work.

The Clothoid Fillet method relies on the fact that the scaling factor, σ_c, of a clothoid segment represents the rate

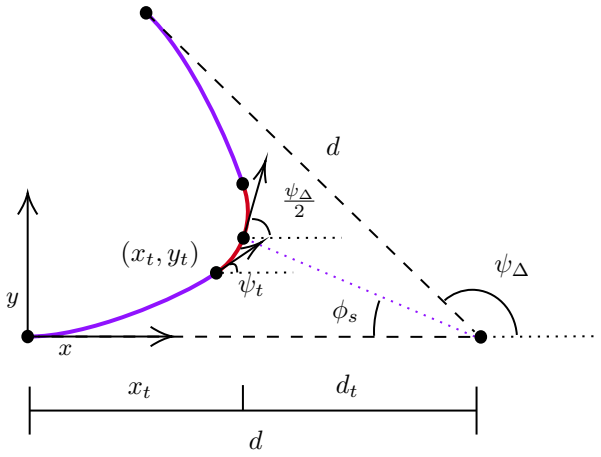

Fig. 5. Smoothing with clothoid segments. The blue lines represent clothoids reflected about the bisecting angle and the red segment is a maximum curvature segment.

of change of the curvature of the segment. This method uses the maximum change in curvature, k'_{max}, to transition from the initial straight segment ($k = 0$), to a maximum curvature ($k = k_{max}$) arc. The transition segment is then reflected to obtain a transition from the constant curvature arc to the second straight segment. The resulting smoothed path consists of a series of segments including straight segments, k_{max} orbits, and clothoid transition segments with curvature changing linearly by k'_{max}. Fig. 5 shows a representation of a series of segments generated by the path smoothing algorithm when transition segments are used. The blue segments are transition segments and the red segment is a k_{max} arc.

When the turn is small enough enough two clothoid segments can be used to smooth the corner, otherwise, a k_{max} arc must be added. The course angle change at which the k_{max} arc segment is required is determined by solving (15) with $k_0 = 0$ to determine the segment length at which the segment reaches maximum curvature ($k = k_{max}$) as

$$s_{kmax} = \frac{k_{max}}{k'_{max}}. \tag{29}$$

Then evaluating (14) with $k_0 = \psi_0 = 0$ and $s = s_{kmax}$ gives

$$\psi_m = \frac{k^2_{max}}{2k'_{max}} \tag{30}$$

where ψ_m is the change of course angle produced change by one clothoid segment. Thus, the maximum course angle change that can be spanned with two clothoid segments is $2\psi_m$.

It remains to define the parameters of the line segments used for corner smoothing with the Clothoid Fillet method. The parameters include initial position, (x_0, y_0), initial course angle, ψ_0, initial curvature, k_0, curvature rate, σ_c, and segment length, s. The following paragraphs discuss how each of these parameters are determined for the smoothing segments based on the course angle change of the corner.

The initial position for the first clothoid segment is the attachment point for the smoothing segments to the initial straight segment. The attachment point can only be determined after the smoothing segments are defined so the smoothing segments will be defined for a base-case where the initial position, course angle, and curvature for the first clothoid segment are $x_0 = y_0 = \psi_0 = k_0 = 0$.

The clothoid curvature rate, σ_c, for the initial clothoid segment is set to the maximum curvature rate ($\sigma_c = k'_{max}$) desired for the current application. The second clothoid segment is a reflection of the first clothoid segment so the curvature rate is negated ($\sigma_c = -k'_{max}$) to reduce the curvature from the transition curvature back to $k = 0$.

The segment length for each of the smoothing segments is determined using the course angle change of the corner and the curvature rate for the clothoid segments. For the case where the turn can be spanned by two clothoid segments ($\psi_\Delta \leq 2\psi_m$), (14) is solved for s with $\psi = \frac{\psi_\Delta}{2}$, $\psi_0 = 0$, and $\sigma_c = k'_{max}$ which yields $s = \sqrt{\psi_\Delta / k'_{max}}$. For the case where a maximum curvature segment is required to smooth the corner, $s = s_{kmax}$ (see (29)). The segment length defined here is the same for both clothoids segments used in the Clothoid Fillet Method. The segment length of the arc segment when one is required is computed using the arc length formula as

$$s = \frac{\phi_a}{k_{max}} \tag{31}$$

where ϕ_a is the central angle of the arc (see Fig. 6) and is expressed as

$$\phi_a = 2\left(\frac{\psi_\Delta}{2} - \psi_t\right). \tag{32}$$

For small turns ($\psi_\Delta \leq 2\psi_m$), two clothoid segments are defined to smooth the corner. Each clothoid segment provides a course angle change of $\psi_\Delta/2$. The initial position (x_t,y_t) and course angle (ψ_t) of the second clothoid segment is determined by evaluating (12)-(15) with $\sigma_c = k'_{max}$, $s = \sqrt{\psi_\Delta / k'_{max}}$, and $k_0 = 0$. The initial curvature of the second clothoid segment is given by $k_0 = \sigma_c s = \sqrt{k'_{max}\psi_\Delta}$.

For large turns ($\psi_\Delta > 2\psi_m$), a k_{max} arc is added between the clothoid transition segments. In this case, the initial clothoid segment transitions from zero curvature to k_{max} so the length of the segment is s_{kmax} (see (29)). The initial position (x_{t1},y_{t1}) and course angle (ψ_{t1}) of the arc segment is then determined by evaluating (12)-(15) with $c = k'_{max}$, $s = s_{kmax}$, and $k_0 = 0$. The length of the arc segment is given in (31). The initial position (x_{t2},y_{t2}) and course angle (ψ_{t2}) of the second clothoid segment can be determined by evaluating (7)-(10) with $(x_0, y_0, \psi_0) = (x_{t1}, y_{t1}, \psi_{t1})$, $\theta = \phi_a$, and $r = 1/k_{max}$.

The parameters defined in the preceding paragraphs are summarized in Table II. The table shows the segment parameters required to smooth large and small corners using the Clothoid Fillet method. The parameters are provided in terms of the course angle change of the corner (ψ_Δ), the maximum curvature of the smoothed corner (k_{max}) and the maximum curvature rate (k'_{max}).

With the smoothing segments defined for the base case of the Clothoid Fillet method, it remains to determine the attachment point (x_a, y_a, ψ_a) on the initial straight segment. The attachment point is determined by computing the parameter d in Fig. 5 which represents the distance from the attachment

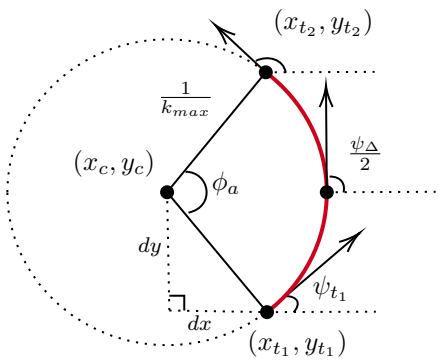

Fig. 6. Definition of key parameters in the development of a k_{max} segment.

TABLE II
SEGMENT DEFINITION FOR CLOTHOID FILLET CORNER SMOOTHING.

ψ_Δ	Segment	(x_0, y_0, ψ_0)	k_0	σ_c	s
Small	Clothoid	(x_a, y_a, ψ_a)	0	k'_{max}	$\sqrt{\frac{\psi_\Delta}{k'_{max}}}$
	Clothoid	(x_t, y_t, ψ_t)	$\sqrt{k'_{max}\psi_\Delta}$	$-k'_{max}$	$\sqrt{\frac{\psi_\Delta}{k'_{max}}}$
Large	Clothoid	(x_a, y_a, ψ_a)	0	k'_{max}	$\frac{k_{max}}{k'_{max}}$
	Arc	(x_t, y_t, ψ_t)	k_{max}	0	$\frac{\phi_a}{k_{max}}$
	Clothoid	$(x_{t_2}, y_{t_2}, \psi_{t_2})$	k_{max}	$-k'_{max}$	$\frac{k_{max}}{k'_{max}}$

point to the end of the straight segment. Equation (27) can be used to compute the value for d_t where y_m is the y component of the transition point between the two smoothing clothoid segments ($y_m = y_t$), or the midpoint of the k_{max} segment, where one is used. Then the attachment distance d is calculated as

$$d = x_t + d_t \tag{33}$$

where x_t is the x component of the transition point between the two clothoid segments, or the midpoint of the k_{max} arc segment, where one is used. Then (3) and (4) can be evaluated using the segment parameters of the initial straight segment and with $s = s_o - d$ where s_o is the original length of the initial straight segment.

Finally, the initial position and heading for each of the smoothing segments are adjusted based on the calculated attachment position and course angle. The adjustment is accomplished by adding the attachment position and course angle to the initial position and course angle of each of the segments.

C. Fermat Fillet

The Fermat spiral was shown to be an effective transition segment for path smoothing applications in [18]. This section reiterates some of the development from [18] to fit in the framework presented in this work and define the segments required to smooth a corner using the Fermat Fillet method. The parameters required to define a Fermat spiral segment are the initial position and course angle (x_0, y_0, ψ_0), initial curvature (k_0), and span of the polar angle (θ_Δ).

The Fermat Fillet method results in a continuous curvature path where the transition segments are Fermat spirals. Similar to the Clothoid Fillet method, the corner can be smoothed with two Fermat spirals for small turns, or two Fermat spirals and a k_{max} arc segment for large turns. The largest course angle change that can be achieved with one Fermat spiral segment is determined by combining (19) and (20) as

$$\psi_m = \sqrt{\frac{\sqrt{7}}{2} - \frac{5}{4}} + \tan^{-1}\left(\sqrt{\frac{\sqrt{7}}{2} - \frac{5}{4}}\right) \tag{34}$$

$$\approx 0.7650 \quad \text{rad.} \tag{35}$$

Then the largest course angle change (ψ_Δ) that can be spanned by two Fermat spiral segments is $2\psi_m$.

In the case where a k_{max} segment is needed ($\psi_\Delta > 2\psi_m$), θ_{kmax} is defined by (19) and the course angle at the transition between the first Fermat spiral segment and the k_{max} arc is ψ_m. In the case where two Fermat spiral segments can span ψ_Δ (where $\psi_\Delta \leq 2\psi_m$), the course angle at the transition is given by $\psi_t = \psi_\Delta/2$. In this case, θ_{kmax} is more difficult to compute because (20) is not invertible. However, [18] suggests using a root finding method to iteratively solve for the roots of the course angle equation. This can be implemented by defining

$$f(\theta) = \theta + \tan^{-1}(2\theta) - \psi_t \tag{36}$$

where subtracting ψ_t moves the root of the course angle equation such that applying the root finding method will result in the θ associated with the desired course angle ψ_t.

With θ_{kmax} and ψ_t defined, the first Fermat spiral segment can be completely defined. The base case starts at the origin with $\psi_0 = 0$, and $\theta_{max} = \theta_{kmax}$ using the value for θ_{kmax} determined above. Then, the scale factor, c, in the Fermat spiral can be computed using (23) with $\theta_{kmax} = \psi_m$ which ensures that k_{max} will be achieved at ψ_m even if the segment ends prior to the curvature reaching k_{max}. The transition point, (x_t, y_t), can be determined by evaluating (16) and (17) at θ_{max} and the course angle at the transition is ψ_t.

In the case where a k_{max} segment is required, an arc is added with with an initial position of (x_t, y_t), initial course angle of ψ_t, radius of $1/k_{max}$, and arc length given by

$$s = \frac{\psi_\Delta - 2\psi_t}{k_{max}} \tag{37}$$

then (8) can be evaluated at $\theta = \psi_\Delta - 2\psi_t$ to get the transition point for the second Fermat spiral segment, (x_t, y_t), and $\theta = \frac{\psi_\Delta - 2\psi_t}{2}$ to get the midpoint of the arc, (x_m, y_m).

The second transition segment is then defined that connects to the first transition segment, or the k_{max} arc at (x_t, y_t). The second transition segment is a reflection of the first transition segment. For the Fermat spiral, this reflection is accomplished by computing the connection point, (x_c, y_c), to the exit segment and flipping the sign of the direction parameter, ρ. The connection point is determined by computing the deviation from the straight line segment, where the cross track deviation, h, and down track deviation, l, are given by

$$h = c\sqrt{\theta_{kmax}}\sin(\theta_{kmax}) \tag{38}$$

$$l = c\sqrt{\theta_{kmax}}\cos(\theta_{kmax}) \tag{39}$$

TABLE III
SEGMENT DEFINITION FOR FERMAT FILLET CORNER SMOOTHING.

ψ_Δ	Segment	(x_0, y_0, ψ_0)	k_0	s	θ_{kmax} Method
Small	Fermat	(x_a, y_a, ψ_a)	0	Eq. (24)	Root Finding
	Fermat (reflected)	(x_c, y_c, ψ_c)	0	Eq. (24)	Root Finding
Large	Fermat	(x_a, y_a, ψ_a)	0	Eq. (24)	Eq. (19)
	Arc	(x_t, y_t, ψ_t)	k_{max}	$\frac{\psi_\Delta - 2\psi_t}{k_{max}}$	n/a
	Fermat (reflected)	(x_c, y_c, ψ_c)	0	Eq. (24)	Eq. (19)

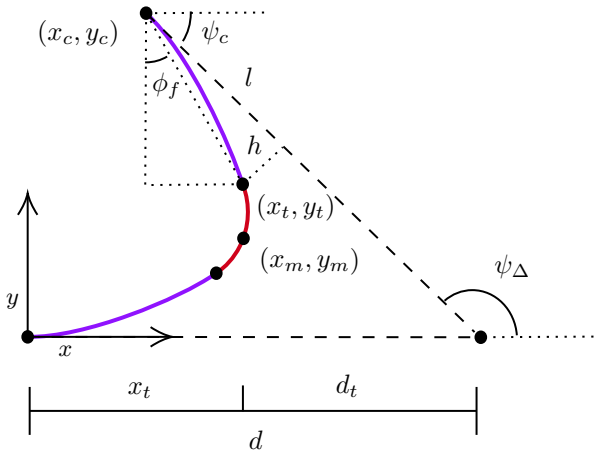

Fig. 7. Parameters used in Fermat Fillet method.

then the magnitude of the deviation is given by

$$\beta = \sqrt{l^2 + h^2}. \tag{40}$$

Then determine the angle, ϕ_f, that relates (x_c, y_c) and (x_t, y_t) as follows

$$\psi_c = \pi - \psi_\Delta \tag{41}$$
$$\phi_f = \frac{\pi}{2} - \psi_c - \theta_{kmax}. \tag{42}$$

The connection point is then calculated as

$$x_c = x_t - \beta \sin(\phi_f) \tag{43}$$
$$y_c = y_t + \rho\beta \cos(\phi_f). \tag{44}$$

The geometry used to compute these parameters is shown graphically in Fig. 7. These results are used with (21) and (22) to compute the properties of the reflected segment.

This method calculates a final connection point and uses a reflection parameter so that the terminal point of the final segment is at the transition point, (x_t, y_t). This requires additional computation for the creation and sampling of the segments but provides simple segment parameter definitions. The parameters used to define the segments using the Fermat Fillet method are summarized in Table III.

The final parameter of interest in the Fermat Fillet method is the distance, d, to the connection point on the first straight segment. Similar to the approach in the Clothoid Fillet method, d_t is computed using (27) where y_m is either the mid-point of the k_{max} arc segment or y_t if there is no k_{max} segment. Then the distance d is calculated as

$$d = x_t + d_t \tag{45}$$

where x_t is the x value of the transition point between the two Fermat segments, or it is the x value of the mid-point of the k_{max} arc, if one is required.

Finally, the initial position and heading for each of the smoothing segments are adjusted based on the calculated attachment position and course angle. The adjustment is accomplished by adding the attachment position and course angle to the initial position and course angle of each of the segments.

IV. IMU SIGNAL GENERATION

The purpose of this section is to present a method to efficiently determine the accelerations and angular rates experienced by an aircraft following a path smoothed using the methods described in Section III. The accelerations and angular rates can then be used as nominal error-free measurements from an IMU and be used to propagate the covariance of the state estimate of a navigation system. For applications requiring high fidelity IMU measurements, additional elements such as coning, sculling, biases, and misalignment and scale-factor errors can be added to the accelerations and angular rates generated in this section [9]. This section will present an approach for determining the acceleration and angular rates for an aircraft using curvilinear motion theory (see Section II-C), vehicle dynamics, and knowledge of the aircraft maneuver (coordinated turn).

Other methods for generating accelerations and angular rates exist, namely, inverting the navigation equations, or 6-DOF aircraft simulations. These methods have potential to be highly accurate, but they are computationally expensive which may be prohibitive depending on the application. The method presented in this section is intended to efficiently provide accelerations and angular rates at high enough fidelity to provide accurate covariance propagation results.

The accelerations experienced by the aircraft in the NED frame can be expressed using curvilinear motion theory as

$$\boldsymbol{a}^n = \ddot{s}\boldsymbol{e}_t^n + \dot{s}\dot{\psi}\boldsymbol{e}_n^n \tag{46}$$

where tangent vector in the 2D plane is computed as a function of the course angle as

$$\boldsymbol{e}_t^n = \begin{bmatrix} \cos(\psi_e) & \sin(\psi_e) & 0 \end{bmatrix}^\mathsf{T} \tag{47}$$

and the normal vector is defined to complete the right-handed coordinate frame between the tangent vector and positive-z unit vector as

$$\boldsymbol{e}_n^n = \begin{bmatrix} 0 & 0 & 1 \end{bmatrix}^\mathsf{T} \times \boldsymbol{e}_t^n. \tag{48}$$

Combining (46) - (48) results in

$$\boldsymbol{a}^n = \begin{bmatrix} \ddot{s}\cos(\psi_e) - \dot{s}\dot{\psi}_e \sin(\psi_e) \\ \ddot{s}\sin(\psi_e) + \dot{s}\dot{\psi}_e \cos(\psi_e) \\ 0 \end{bmatrix} \tag{49}$$

as the expression for the acceleration experienced by the aircraft in the NED frame and is valid for all of the segment types presented in this work.

The angular rates experienced by an aircraft are dependent on the path shape and the dynamics of the vehicle maneuver. An aircraft, for example, can perform a variety of maneuvers to negotiate a turn (i.e. skid-to-steer, coordinated turn) and each will result in different angular rates. In this work, the angular rates for an aircraft executing a coordinated turn will be examined. The coordinated turn is a common aircraft turning condition where there is no lateral acceleration in the body frame of the aircraft [23].

The coordinated turn assumption provides a useful relationship between the course angle (ψ_e) and roll angle (ϕ_e) [4] of the aircraft as

$$\dot{\psi}_e = \frac{g}{V_a}\tan\phi_e. \tag{50}$$

The rate of change of the roll angle can be computed by first differentiating (50) as

$$\ddot{\psi}_e = \frac{g}{V_a}\frac{1}{\cos^2\phi_e}\dot{\phi}_e \tag{51}$$

and solving for the roll angle rate, which yields

$$\dot{\phi}_e = \ddot{\psi}_e\frac{V_a}{g}\cos^2\phi_e. \tag{52}$$

The roll rate ($\dot{\phi}_e$) and course angle rate ($\dot{\psi}_e$) need to be converted to body-frame angular rates, (p, q, r). This conversion requires a frame change from the Euler angle frames to the body-frame which will be completed using a ZYX Euler angle sequence. The Euler angle rates are related to the body-frame angular rates [4] as

$$\begin{bmatrix} p \\ q \\ r \end{bmatrix} = \underbrace{\begin{bmatrix} 1 & 0 & -\sin\theta \\ 0 & \cos\phi & \sin\phi\cos\theta \\ 0 & -\sin\phi & \cos\phi\cos\theta \end{bmatrix}}_{A_B} \begin{bmatrix} \dot{\phi}_e \\ \dot{\theta}_e \\ \dot{\psi}_e \end{bmatrix}. \tag{53}$$

Assuming no change in pitch angle, substitution of (52) and (59) into (53) yields

$$\begin{bmatrix} p \\ q \\ r \end{bmatrix} = A_B \begin{bmatrix} \ddot{\psi}_e\frac{V_a}{g}\cos^2\phi_e \\ 0 \\ \dot{\psi}_e \end{bmatrix} \tag{54}$$

or in component form

$$p = \ddot{\psi}_e\frac{V_a}{g}\cos^2\phi_e - \dot{\psi}_e\sin\theta_e \tag{55}$$

$$q = \dot{\psi}_e\sin\phi_e\cos\theta_e \tag{56}$$

$$r = \dot{\psi}_e\cos\phi_e\cos\theta_e. \tag{57}$$

This indicates that to compute the angular rates of an aircraft executing a coordinated turn, $\dot{\psi}_e$ and $\ddot{\psi}_e$ must be determined for each of the segment type in the path.

The time-derivative of the course angle is computed from (14) utilizing the chain rule

$$\dot{\psi}_e(t) = \frac{d}{dt}\psi_e\left(s\left(t\right)\right) \tag{58}$$

$$= \frac{d\psi_e}{ds}\frac{ds}{dt}. \tag{59}$$

The second derivative of heading with respect to time is computed utilizing a combination of multiplication rule and chain rule as

$$\ddot{\psi}_e(t) = \frac{d}{dt}\psi_e'(s(t))\dot{s}(t) \tag{60}$$

$$= \frac{d\psi_e'}{ds}\frac{ds}{dt}\dot{s}(t) + \psi_e'\ddot{s}(t) \tag{61}$$

$$= \psi_e''(s(t))\dot{s}(t)^2 + \psi_e'(t)\ddot{s}(t). \tag{62}$$

To generate the angular rates for the aircraft, it remains to define $\dot{\psi}_e$ and $\ddot{\psi}_e$ for each of the segment types used in the path smoothing algorithm. The line segment is trivially defined as $\dot{\psi}_e = \ddot{\psi}_e = 0$. The following subsections provide the derivation of expressions for $\dot{\psi}_e$ and $\ddot{\psi}_e$ for the remaining segment types.

A. Arc

The course angle of an arc segment is related linearly to the length along the segment as

$$\psi_a(s) = \psi_0 + ks \tag{63}$$

where k is the constant curvature of the arc segment. The derivative of this with respect to path length is given by

$$\psi_a'(s) = k \tag{64}$$

and the second derivative is $\psi'' = 0$. Then the time derivatives of the course angle (see (59) and (62)) are given by

$$\dot{\psi}_a = k\dot{s} \tag{65}$$

$$\ddot{\psi}_a = k\ddot{s}. \tag{66}$$

B. Clothoid

The course angle of the clothoid segment is given in (14). The derivative with respect to the path length is given by

$$\psi_c'(s) = k_0 + \sigma_c s \tag{67}$$

and the second derivative is given by

$$\psi_c'' = \sigma_c. \tag{68}$$

Then applying (59) and (62) the time derivatives are given by

$$\dot{\psi}_c(s) = \left(k_0 + \sigma_c s\right)\dot{s} \tag{69}$$

$$\ddot{\psi}_c(s) = \sigma_c\dot{s}^2 + \left(k_0 + \sigma_c s\right)\ddot{s}. \tag{70}$$

C. Fermat Spiral

The course angle of a Fermat Spiral segment is given in (20) in terms of the polar angle θ. In [18], a change of variables is presented as $u = \sqrt{\theta}$ which provides consistent sampling per path length. Then, the course angle can be expressed as

$$\psi_f(u) = u^2 + \arctan\left(2u^2\right). \tag{71}$$

This change of variables is useful because an expression for the time derivative of u exists and is given by

$$\dot{u} = \frac{\dot{s}}{c\sqrt{1+4u^4}} \tag{72}$$

Then the time derivative of the path segment can be computed as follows

$$\dot{\psi}_f = \rho \frac{d\psi}{du}\frac{du}{dt} \quad (73)$$

$$= \rho\left(2u + \frac{4u}{4u^4+1}\right)\dot{u} \quad (74)$$

where ρ is the direction of the curve defined in (11). The second derivative is computed by applying the quotient rule and chain rule as

$$\ddot{\psi}_f = \frac{d}{dt}\left(\frac{2\dot{s}\left(4u^5+3u\right)\sqrt{4u^4+1}}{c\left(4u^4+1\right)^2}\right). \quad (75)$$

The time derivative of the numerator is given by

$$\dot{\mathcal{N}} = 2\left[\ddot{s}\left(\left(4u^5+3u\right)\sqrt{4u^4+1}\right)+\dot{s}\dot{\mathcal{N}}_1\right] \quad (76)$$

where

$$\dot{\mathcal{N}}_1 = \frac{d}{dt}\left(\left(4u^5+3u\right)\sqrt{4u^4+1}\right) \quad (77)$$

$$= \left[\left(20u^4+3\right)\sqrt{4u^4+1} + \frac{8u^3\left(4u^5+3u\right)}{\sqrt{4u^4+1}}\right]\dot{u}. \quad (78)$$

The time derivative of the denominator is given by

$$\dot{\mathcal{D}} = 32c\left(4u^4+1\right)u^3\dot{u} \quad (79)$$

then

$$\ddot{\psi}_f = \rho\frac{\dot{\mathcal{N}}\mathcal{D} - \dot{\mathcal{D}}\mathcal{N}}{\mathcal{D}^2}. \quad (80)$$

V. Results

This section provides results for the path smoothing and aircraft state generation. The first set of results will include a comparison of the corner smoothing techniques presented in Section III. These results include a comparison between the path characteristics and the execution time for the methods presented. The second set of results show a comparison between the generated IMU measurements.

A. Path Smoothing

The algorithm defined in Section III was implemented in Matlab where a series of waypoints was converted to a continuous curvature path. Fig. 8 shows a piece-wise linear path smoothed using the three methods presented here. This was generated using $k_{max} = 2.1$, and $k'_{max} = 3$.

The course angle and curvature for the scenario shown in Fig. 8 is shown in Fig. 9. For this scenario all three methods achieve the maximum curvature but the differences in the shape for the curvature and course angle are apparent. The curvature plot shows a step change for the Arc Fillet method, a linear change for the Clothoid Fillet method, and a smooth transition for the Fermat Fillet method.

The shape of the curvature and course angle graphs should be considered when deciding what corner smoothing algorithm to use. For example, the arc fillet method has a step change in curvature which is infeasible for a fixed-wing aircraft. This highlights the need to consider the dynamics of the target

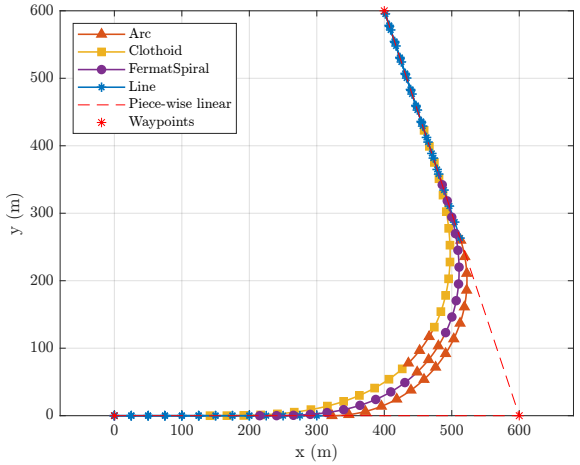

Fig. 8. Continuous curvature path given 3 waypoints. Blue lines represent straight segments, yellow lines with square markers represent clothoid segments, purple lines with circle markers represent Fermat segments and the orange lines with triangle markers represents the k_{max} arc segment. The dashed red line indicates the piece-wise linear path and the red asterisk symbols represent the waypoints.

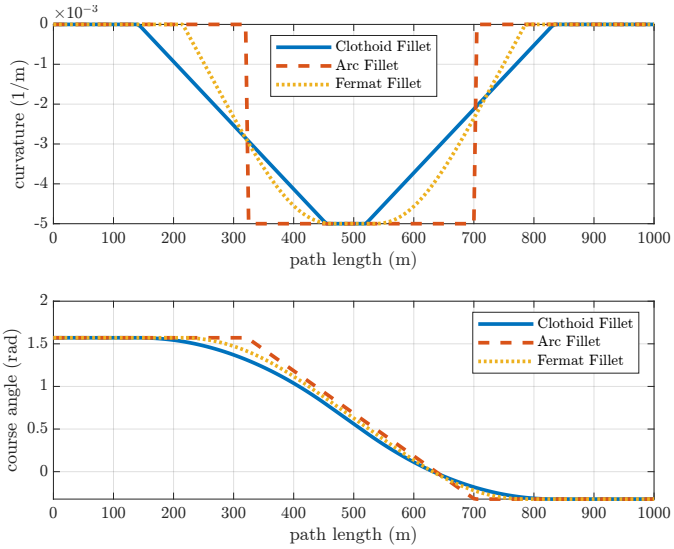

Fig. 9. Curvature and course angle along paths using the three path smoothing methods. Clothoid fillet (solid), arc fillet (dashed), Fermat fillet (dotted).

system and the desired maneuvers when selecting a corner smoothing algorithm and the associated path segment types.

The processing time for the 3 methods were compared using a series of 12 waypoints. The Clothoid Fillet method is the slowest (due to the Fresnel Integrals), and the Arc Fillet method is the fastest. The Fermat Fillet method provides a 63.3% improvement in execution time when compared with the Clothoid Fillet method, whereas the Arc Fillet method provides an 87.98% improvement. These results provide a framework for deciding which method best suits the target application. For example, if the application does not require continuous curvature, the Arc Fillet method is very efficient and fulfills the objective. However, if continuous curvature is desired, the Fermat Fillet or Clothoid Fillet methods should be considered and if execution time is a primary concern, the

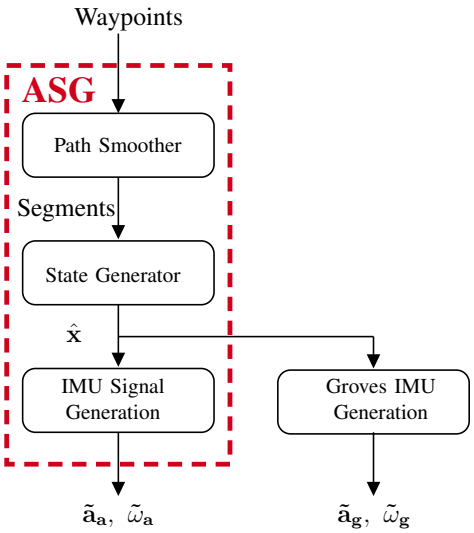

Fig. 10. Block diagram of ASG and RII used for the results comparison.

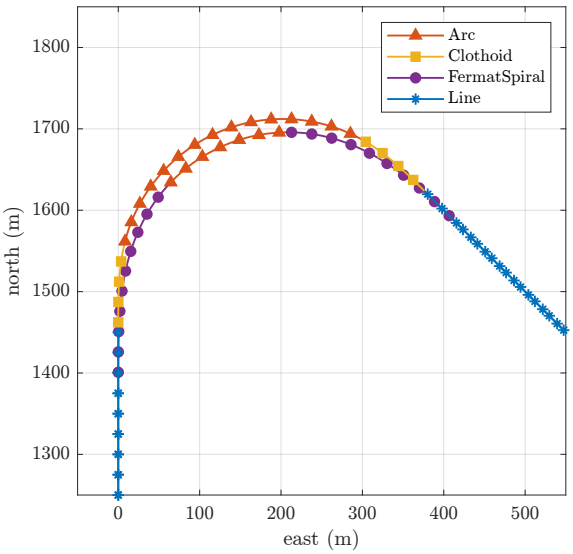

Fig. 11. First turn of nominal trajectory scenario showing the Clothoid Fillet and Fermat Fillet paths. The paths were created with $k_{max} = 0.005\ 1/rad$, and $k'_{max} = 0.00005\ 1/rad/m$.

preference should be given to the Fermat Fillet method.

B. IMU Measurement Results

The previous subsection showed results for the three path smoothing methods presented in this work. This section will extend these results and present the specific force and angular rates generated using the IMU signal generation method described in Section IV. Due to the discontinuities in course angle for the Arc Fillet method, it will be omitted from this analysis.

The IMU signals generated using the method shown in Section IV will be compared with the Groves method available as an open-source[1] implementation based on derivations in [7] and used in [24]. Fig. 10 shows a diagram of how the accelerometer, $\tilde{\boldsymbol{a}} = [a_x\ a_y\ a_z]^\intercal$, and gyro, $\tilde{\boldsymbol{\omega}} = [g_x\ g_y\ g_z]^\intercal$, measurements are generated using the ASG and Groves methods. Two simple scenarios of four waypoints (two turns) were used to compare the methods. The first method will be referred to as the nominal trajectory scenario with $k_{max} = 0.005\ 1/rad$, and $k'_{max} = 0.00005\ 1/rad/m$. The second will be referred to as the aggressive trajectory scenario that has waypoints closer together and with $k_{max} = 0.01\ 1/rad$, and $k'_{max} = 0.0002\ 1/rad/m$. Fig. 11 shows one of the turns in the nominal trajectory scenario with the Clothoid Fillet and Fermat Fillet methods.

The accelerometer and gyro measurements for the Clothoid and Fermat Fillet methods for the nominal trajectory scenario are provided in Figs. 12 and 13, respectively. The IMU signals for both methods match the baseline results well. The slight differences between the Groves method and ASG method are difficult to see in Figs. 12 and 13 so an error metric will be introduced in the following paragraphs to illustrate the differences.

The Groves method relies on a discrete derivative taken at each time step, dt. For a small time step, this method provides consistent results. However, in some applications, accurate

[1]https://github.com/jmcanana/MATLAB-Groves

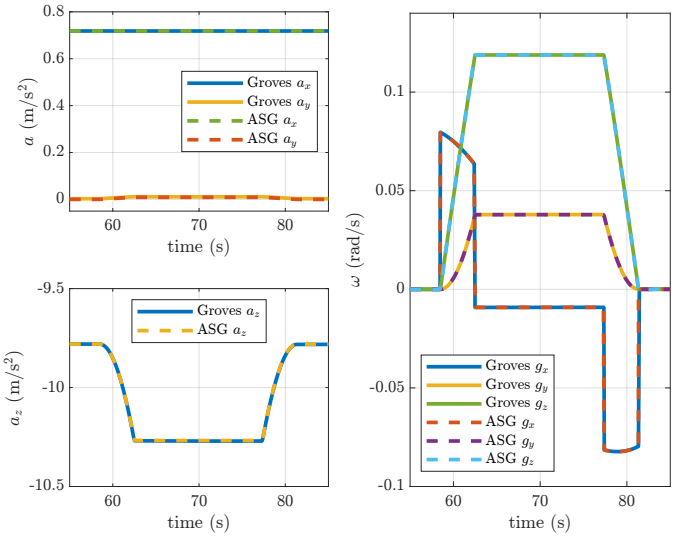

Fig. 12. Accelerometer and gyro measurements for the nominal trajectory scenario using the Clothoid Fillet corner smoother.

IMU signals are desired with larger time steps. This can be particularly useful in mission and path planning scenarios where reducing processor usage is desired. One benefit to the ASG method is that the IMU signal generation avoids the derivative and maintains accuracy for large time steps because the IMU measurements have analytical solutions along the path segments.

To quantify the effect of increasing the time step on these two methods, baseline IMU signals were generated using the Groves method with a small time step ($dt = 0.001s$). IMU signals for time steps ranging from $dt = 0.1s$ to $dt = 3.0s$ were generated using both methods. The integrated norm of the error, Υ, was calculated as the integrated difference between the IMU measurements generated by each method and the baseline Groves method (with $dt = 0.001s$). Fig. 14 provides

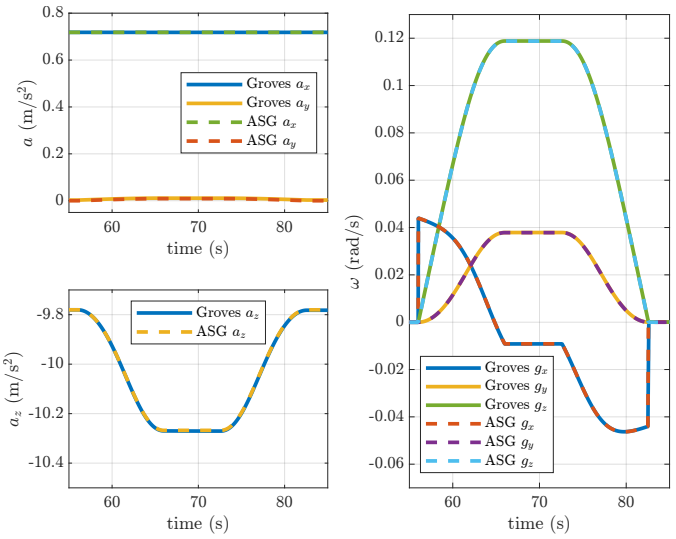

Fig. 13. Accelerometer and gyro measurements for the nominal trajectory scenario using the Fermat Fillet corner smoother.

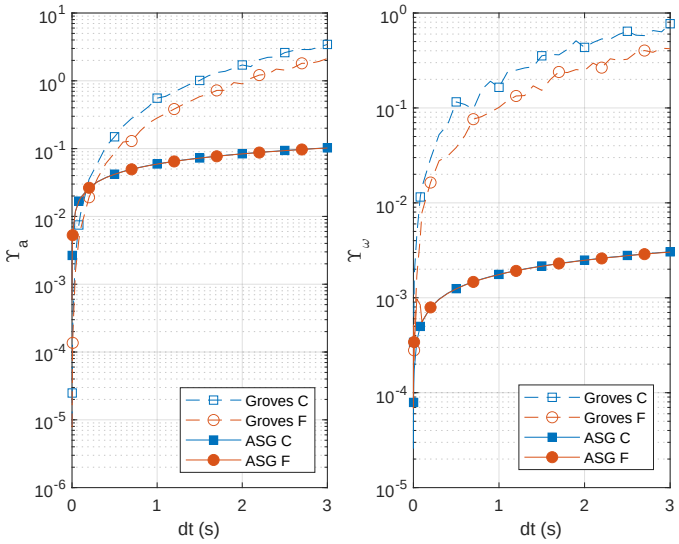

Fig. 14. Integrated norm of the error for the accelerometer (left) and gyro (right) measurements for the nominal trajectory scenario for a range of sample times. The plots show errors of both IMU signal generation methods (RII, ASG) for both Clothoid Fillet (C) and Fermat Fillet (F) corner smoothing algorithms. The y-axis was plotted with a log-scale to more clearly show the differences.

a graph of Υ for increasing dt using the Groves and ASG methods for the Clothoid and Fermat fillet methods. The errors associated with the Groves method grow more quickly than the ASG method as the step size increases for both the accelerometer and gyro measurements. The ASG method results in nearly constant errors for both corner smoothing methods. The ASG method clearly provides more accurate IMU signals for the time steps shown.

The integrated norm of the error, Υ, for the aggressive trajectory scenario is shown in Fig. 15. This trajectory has waypoints that are closer together and $k_{max} = 0.01\ 1/rad$, and $k'_{max} = 0.0002\ 1/rad/m$. The error plots indicate that the ASG method outperforms the Groves method for this

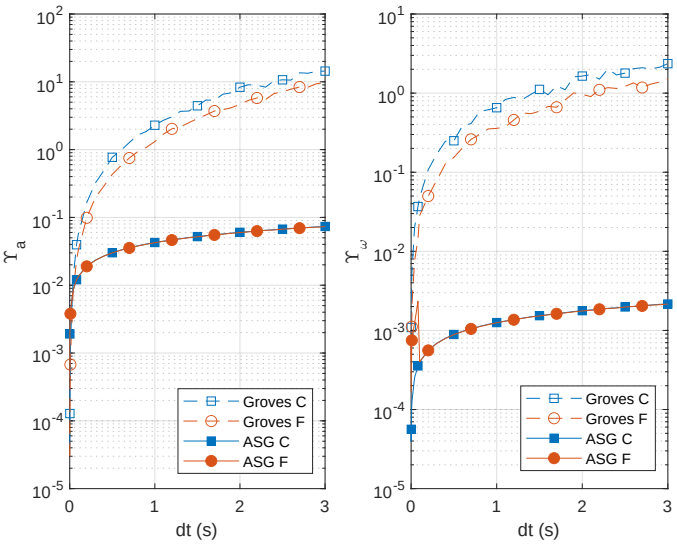

Fig. 15. Integrated norm of the error for the accelerometer (left) and gyro (right) measurements for the aggressive trajectory scenario for a range of sample times. The plots show errors of both IMU signal generation methods (RII, ASG) for both Clothoid Fillet (C) and Fermat Fillet (F) corner smoothing algorithms. The y-axis was plotted with a log-scale to more clearly show the differences.

trajectory as well, and the general error characteristics are consistent with the nominal trajectory scenario. It should be observed that the errors are higher for the aggressive trajectory scenario than the nominal trajectory scenario.

VI. Conclusion

This work has presented ASG as a method for generating aircraft states and IMU signals along a candidate path. The method includes a corner smoothing algorithm to convert a series of waypoints into a smoothed reference trajectory and uses path segment geometry to generate the aircraft states. The final stage of the method applies curvilear motion theory and vehicle maneuver dynamics to generate IMU signals along the candidate path. The generated states and IMU signals can be applied to a variety of applications, including general path planning, and covariance propagation for inertial navigation systems.

Three corner smoothing approaches were presented in a unified framework. The Clothoid Fillet and Fermat Fillet algorithms can be parameterized to respect vehicle constraints in curvature and curvature rate. The results showed that the Fermat Fillet requires less processing time than the Clothoid Fillet due to the Fresnel integrals. The Arc Fillet method requires the least processing time but has discontinuities in curvature and is thus not suitable for a fixed wing aircraft.

The results for the IMU signal generation stage show that the ASG method performs better than the Groves method by avoiding a discrete derivative. This allows for large step sizes in sampling when using the ASG method.

References

[1] P. T. Kabamba, S. M. Meerkov, and F. H. Zeitz, "Optimal path planning for unmanned combat aerial vehicles to defeat radar tracking," *Journal of Guidance, Control, and Dynamics*, vol. 29, no. 2, pp. 279–288, 2006. [Online]. Available: https://doi.org/10.2514/1.14303

[2] N. Ceccarelli, J. J. Enright, E. Frazzoli, S. J. Rasmussen, and C. J. Schumacher, "Micro uav path planning for reconnaissance in wind," in *2007 American Control Conference*, 2007, pp. 5310–5315.

[3] L. Blackmore, M. Ono, and B. C. Williams, "Chance-Constrained Optimal Path Planning With Obstacles," *IEEE Transactions on Robotics*, vol. 27, no. 6, pp. 1080–1094, Dec. 2011.

[4] Beard, Randy and McLain, Timothy, *Small Unmanned Aircraft Theory and Practice*. Princeton University Press, 2012.

[5] M. C. Potter, E. W. Nelson, C. L. Best, and W. G. McLean, *Schaum's Outline of Engineering Mechanics: Dynamics*, 7th ed. McGraw Hill, 2021.

[6] N. E. Du Toit and J. W. Burdick, "Robot Motion Planning in Dynamic, Uncertain Environments," *IEEE Transactions on Robotics*, vol. 28, no. 1, pp. 101–115, Feb. 2012.

[7] P. D. Groves, *Principles of GNSS, Inertial, and Multisensor Integrated Navigation Systems*. Norwood, UNITED STATES: Artech House, 2013.

[8] J. Farrell, *Aided Navigation: GPS with High Rate Sensors*, 1st ed. USA: McGraw-Hill, Inc., 2008.

[9] P. G. Savage, *Strapdown analytics*. Strapdown Associates Maple Plain, MN, 2000, vol. 2.

[10] K. Liu, W. Wu, K. Tang, and L. He, "IMU Signal Generator Based on Dual Quaternion Interpolation for Integration Simulation," *Sensors*, vol. 18, no. 8, p. 2721, Aug. 2018, number: 8 Publisher: Multidisciplinary Digital Publishing Institute. [Online]. Available: https://www.mdpi.com/1424-8220/18/8/2721

[11] G. Yan, J. Wang, and X. Zhou, "High-precision simulator for strapdown inertial navigation systems based on real dynamics from gnss and imu integration," in *China Satellite Navigation Conference (CSNC) 2015 Proceedings: Volume III*, J. Sun, J. Liu, S. Fan, and X. Lu, Eds. Berlin, Heidelberg: Springer Berlin Heidelberg, 2015, pp. 789–799.

[12] Z. Li, Z.-x. Cai, X.-p. Ren, A.-b. Chen, and Z.-c. Xue, "Vehicle kinematics modeling and design of vehicle trajectory generator system," *Journal of Central South University*, vol. 19, no. 10, pp. 2860–2865, Oct. 2012. [Online]. Available: http://link.springer.com/10.1007/s11771-012-1352-3

[13] T. Brunner, J.-P. Lauffenburger, S. Changey, and M. Basset, "Magnetometer-Augmented IMU Simulator: In-Depth Elaboration," *Sensors*, vol. 15, no. 3, pp. 5293–5310, Mar. 2015, number: 3 Publisher: Multidisciplinary Digital Publishing Institute. [Online]. Available: https://www.mdpi.com/1424-8220/15/3/5293

[14] K. Yang and S. Sukkarieh, "An Analytical Continuous-Curvature Path-Smoothing Algorithm," *IEEE Transactions on Robotics*, vol. 26, no. 3, pp. 561–568, Jun. 2010.

[15] A. Ravankar, A. A. Ravankar, Y. Kobayashi, Y. Hoshino, and C.-C. Peng, "Path Smoothing Techniques in Robot Navigation: State-of-the-Art, Current and Future Challenges," *Sensors*, vol. 18, no. 9, p. 3170, Sep. 2018.

[16] A. Scheuer and T. Fraichard, "Continuous-curvature path planning for car-like vehicles," in *Proceedings of the 1997 IEEE/RSJ International Conference on Intelligent Robot and Systems. Innovative Robotics for Real-World Applications. IROS 97*, vol. 2, Sep. 1997, pp. 997–1003 vol.2.

[17] M. Vázquez-Méndez and G. Casal Urcera, "The Clothoid Computation: A Simple and Efficient Numerical Algorithm," *Journal of Surveying Engineering*, vol. 142, pp. 04 016 005:1–9, Aug. 2016.

[18] A. M. Lekkas, A. R. Dahl, M. Breivik, and T. I. Fossen, "Continuous-Curvature Path Generation Using Fermat's Spiral," *Modeling, Identification and Control: A Norwegian Research Bulletin*, vol. 34, no. 4, pp. 183–198, 2013.

[19] R. Levien, "The Euler spiral: a mathematical history," University of California at Berkley, Tech. Rep., 2008.

[20] D. K. Wilde, "Computing clothoid segments for trajectory generation," in *2009 IEEE/RSJ International Conference on Intelligent Robots and Systems*, Oct. 2009, pp. 2440–2445.

[21] G. Brambley and N. L. Fulton, "Specific length trajectories optimised for maximum acceleration using conic parameterised clothoids," *IEEE Transactions on Aerospace and Electronic Systems*, vol. 47, no. 4, pp. 2627–2636, 2011.

[22] T. Fraichard and A. Scheuer, "From Reeds and Shepp's to continuous-curvature paths," *IEEE Transactions on Robotics*, vol. 20, no. 6, pp. 1025–1035, Dec. 2004.

[23] N. Nabaa and R. Bishop, "Validation and comparison of coordinated turn aircraft maneuver models," *IEEE Transactions on Aerospace and Electronic Systems*, vol. 36, no. 1, pp. 250–259, 2000.

[24] J. G. McAnanama and G. Marsden, "An open source flight dynamics model and imu signal simulator," in *2018 IEEE/ION Position, Location and Navigation Symposium (PLANS)*, 2018, pp. 874–881.

Austin Costley is a GNC Engineer at Autonomous Solutions, Inc. (ASI) located in Mendon, Utah. He is also a Research Assistant at Utah State University where he is working toward the Ph.D. in Electrical and Computer Engineering. Prior to working at ASI, Mr. Costley earned the M.S. and B.S. Degree in Electrical and Computer Engineering at USU in 2017. His research interests include path planning for autonomous vehicles in uncertain environments and localization and control of autonomous vehicles.

Randall Christensen is currently an Assistant Professor in the Electrical and Computer Engineering Department at Utah State University. Prior to USU, Dr. Christensen worked at Space Dynamics Laboratory and Raytheon Missile Systems. He earned the Ph.D. in 2013 in Mechanical and Aerospace Engineering at Utah State University. His research interests include GPS-denied navigation and control of autonomous vehicles, and efficient statistical frameworks for real-time decision making and optimization of GNC systems.

Greg N. Droge is an Assistant Professor in the department of Electrical and Computer Engineering at Utah State University. His research is focused on the coordination of unmanned systems. This includes the development of autonomous decision-making capabilities that would enable teams to react to actionable intelligence and adapt their performance to accomplish a higher-level objective. He completed his PhD at Georgia Institute of Technology in Electrical and Computer Engineering in 2014. His thesis focused on distributed optimization and multi-vehicle coordinated path planning. After graduating, he worked on an ONR program at SPAWAR-PAC to develop, test, and demonstrate a collaborative cross domain mission planning capability aimed at improving coordinated operations of teams of unmanned systems. He also supported the integration team which employed an evolutionary systems engineering model to establish a continuous improvement process for assessing capabilities and limitations of autonomy and maturing technologies accordingly. Dr. Droge also received an MS from Georgia Tech in 2012. Prior to Georgia Tech, he studied at Brigham Young University where he graduated Magna Cum Laude with a BS in Electrical Engineering in 2009.

Robert C. Leishman is currently the Director of the Autonomy and Navigation Technology (ANT) Center at the Air Force Institute of Technology (AFIT), which he began in April 2019. He is also a Research Assistant Professor in the Department of Electrical and Computer Engineering at AFIT. Prior to AFIT, Dr. Leishman worked at the Air Force Research Laboratory. He earned the Ph.D. in 2013 in Mechanical Engineering at Brigham Young University in Provo, UT through support from the DoD SMART Scholarship. His research interests include autonomous vehicles, robust alternative navigation, image processing, sensor fusion, and control.

CHAPTER 5

PATH PLANNING WITH UNCERTAINTY FOR AIRCRAFT UNDER THREAT OF DETECTION FROM GROUND-BASED RADAR

Path Planning with Uncertainty for Aircraft Under Threat of Detection from Ground-Based Radar

Austin Costley, Greg Droge, Randall Christensen, Robert C. Leishman, James Swedeen

***Abstract*—Mission planners for aircraft operating under threat of detection by ground-based radar systems are concerned with the probability of detection. Current path planning methods for such scenarios consider the aircraft pose, radar position, and radar parameters to be deterministic and known. This paper presents a framework for incorporating uncertainty in these quantities into a radar detection model that is used by a path planner. The developed path planner evaluates the radar detection risk in the presence of uncertainties and uses linear covariance analysis to efficiently generate error budgets. The error budgets identify the contribution of each source of uncertainty (e.g., sensor measurement noise, radar position uncertainty) to the overall variability in the probability of detection. The framework is applied to a modified visibility graph path planner that uses the detection risk and its variability to calculate path adjustments, which maintain the detection risk below a specified threshold. The results show that the framework is effective at providing actionable information to the mission planner that improves the final planned path and reduces the detection risk.**

NOMENCLATURE

P_D	Approximation of probability of detection
$\bar{P}_D$	Nominal value of P_D
δP_D	Perturbation of P_D about nominal
P_{fa}	Probability of false alarm
$\mathcal{S}$	Signal-to-noise ratio
σ_r	Radar cross section (m^2)
R	Range to target (m)
c_r	Lumped radar parameter ($Jm^2/^\circ K$)
$\boldsymbol{x_a}$	Aircraft state vector
$\bar{\boldsymbol{x}}_{\boldsymbol{a}}$	Nominal aircraft state
$\boldsymbol{p_a^n}$	Aircraft position vector in NED frame
$\boldsymbol{\Theta_a}$	Aircraft Euler angle vector
p_{an}, p_{ae}, p_{ad}	Aircraft position in NED frame (m)
ϕ_a, θ_a, ψ_a	Aircraft Euler angles roll, pitch, yaw ($rad.$)
$\boldsymbol{x_r}$	Radar state vector
$\bar{\boldsymbol{x}}_{\boldsymbol{r}}$	Nominal radar state
$\boldsymbol{p_r^n}$	Radar position vector in NED frame
p_{rn}, p_{re}, p_{rd}	Radar position elements in NED frame (m)
a, b, c	Ellipsoid RCS parameters
α	RCS azimuth angle ($rad.$)
ϕ	RCS elevation angle ($rad.$)
C_{aa}	Aircraft pose covariance
C_{rr}	Radar state covariance
A_{Pa}	Jacobian of P_D w.r.t. $\boldsymbol{x_a}$
A_{Pr}	Jacobian of P_D w.r.t. $\boldsymbol{x_r}$
σ_{pd}	Standard deviation of P_D
$\boldsymbol{v^n}$	Velocity vector in NED frame
q_b^n	Aircraft attitude quaternion
$\boldsymbol{b_a^b}$	Accelerometer bias in body frame
$\boldsymbol{b_g^b}$	Gyro bias in body frame
$\boldsymbol{\nu^b}$	Specific force vector in body frame
$\boldsymbol{\omega^b}$	Angular rate vector in body frame
$\boldsymbol{g^n}$	Gravity vector in NED frame
$\boldsymbol{w_a}$	FOGM driving noise for accelerometer bias
$\boldsymbol{w_g}$	FOGM driving noise for gyro bias
$\boldsymbol{n_\nu}$	Accelerometer noise std. dev.
$\boldsymbol{n_\omega}$	Gyro noise std. dev.
$\delta\theta_b^n$	Error rotation vector
$\delta\boldsymbol{x_e}$	Error state vector
R_b^n	Rotation matrix from body to NED frame
P	EKF covariance matrix
σ_n, σ_e, σ_d	GPS noise std. dev.
σ_h	Altimeter noise std. dev.
σ_ψ	Heading noise std. dev.
τ_a, τ_g	FOGM time constant for IMU biases
$\sigma_{a,ss}$	Accelerometer bias steady state std. dev.
$\sigma_{g,ss}$	Gyro bias steady state std. dev.
κ	Path segment curvature ($\frac{1}{m}$)
m_σ	Multiple of σ_{pd} used in planner
P_{DT}	P_D threshold for planning
P_{true}	True navigation error covariance
C_A	Augmented system covariance
k	Boltzmann's constant

This work was supported by Air Force Research Laboratory, Wright-Patterson Air Force Base, OH.

A. Costley is with the Electrical and Computer Engineering Department, Utah State University, Logan, UT 84322 USA (e-mail: austin.costley@usu.edu)
G. Droge is with the Electrical and Computer Engineering Department, Utah State University, Logan, UT 84322 USA (e-mail: greg.droge@usu.edu)
R. Christensen is with Blue Origin, Kent, WA 98032 USA (e-mail: rchristensen@blueorigin.com)
R. Leishman is with Draper Laboratory, Denver, CO 80602 USA (e-mail: rleishman@draper.com)
J. Swedeen is with the Electrical and Computer Engineering Department, Utah State University, Logan, UT 84322 USA (e-mail: james.swedeen@usu.edu)

I. INTRODUCTION

Aircraft mission planners are tasked with planning paths for aircraft operating under threat of detection by ground-based radar systems. Example missions include reconnaissance [1], radar counter-measure deployment [2, 3], and combat operations [4]. Mission planners for such scenarios are primarily interested in the probability of being detected by a radar system. This paper develops and demonstrates a framework that allows for the consideration of aircraft and radar state uncertainties when planning a path constrained to stay below a given probability of detection threshold.

The work herein builds upon two groups in the literature. The first is the target detection literature in which high-fidelity radar detection models have been developed [5–7]. In particular, [7] defines a value, P_D, that approximates the probability of detecting an aircraft given the signal-to-noise ratio and false alarm rate of the detection. The signal-to-noise ratio is dependent upon radar characteristics, relative positioning, and the radar cross section, which can vary significantly based upon the orientation of the aircraft. The second group is the radar detection path planning literature [2–4, 8–13], which use some form of detection risk that may only consider some aspects of the high-fidelity radar detection models. The planning literature seeks to rapidly evaluate candidate paths while the target detection literature seeks to create a high-fidelity determination of detection probabilities. Neither body considers the uncertainty of the aircraft state, radar position, or radar parameters, which are all estimated and include some uncertainty.

When accurate position measurements are available, neglecting aircraft state uncertainty is a useful technique to reduce complexity. However, scenarios where an aircraft is seeking to avoid radar detection may include regions where accurate position measurements are not available (i.e. GPS-denied regions). In such regions, the state uncertainty grows and becomes a significant factor in the variability of the predicted P_D [14]. Aircraft operating in radar detection regions are often equipped with an aided inertial navigation system (INS). Such systems use measurements from an inertial measurement unit (IMU) and aiding sources, such as GPS, to estimate the aircraft state and state covariance [15–17]. A common filtering technique for an aided INS is the Extended Kalman Filter (EKF) [18, 19], which propagates and updates the state estimate in the presence of measurement and process noise.

There are a couple of key questions that must be answered when creating paths that respect thresholds on P_D. First, how does the planner calculate an estimate for P_D and its uncertainty along a path while considering uncertainty in the aircraft state, radar position, and radar parameters? Answering this question aids in determining whether a path is valid. Second, how does one determine which noise sources (e.g., measurement, process, uncertain initial conditions, etc.) are the main cause of growth in P_D and its associated uncertainty (i.e., error budget analysis [17, 18])? Answering this question aids in determining, for example, whether a higher quality sensor will sufficiently reduce P_D for a given path.

A Monte Carlo approach could be utilized to answer the questions posed in the previous paragraph to an arbitrary level of fidelity. In a Monte Carlo approach, each path under consideration is simulated hundreds or thousands of times to model the effect of uncertainties on the aircraft state as estimated by the navigation filter. Each simulation, or run, uses a different sampling of the noise and radar uncertainties. The resulting ensemble statistics are calculated for P_D at each point in time to quantify the variability in P_D due to the uncertainties present in the simulations. The Monte Carlo analysis is repeated several times with a different set of active error sources to obtain the necessary data to build an error budget. This approach is computationally intensive and not well-suited to rapid planning or error budget analysis.

An efficient alternative to Monte Carlo analysis is linear covariance analysis [18, 20, 21]. Linear covariance analysis utilizes similar linearization techniques and Gaussian noise assumptions as employed by an EKF to propagate the second order moments of the random variables in question. This approach approximates the same statistical information as Monte Carlo analysis in a single simulation over the trajectory.

The path planner in this paper evaluates P_D with respect to the covariance of the aircraft and radar states using a framework provided in [14, 22]. The IMU measurement generation capability developed in [23] provides inputs to an inertial navigation filter to enable rapid evaluation of the aircraft state covariance along candidate paths. This paper uses linear covariance techniques to rapidly evaluate the variability of P_D due to uncertainties estimated by a navigation filter and demonstrates the use of these statistics in a path planning application. Given a path to be followed, the efficient IMU signal generator in [23] is used to generate representative measurements along the trajectory that are incorporated into a navigation filter. The aircraft and radar state uncertainties are used as in [14, 22] to estimate the variance of P_D. The path planner generates multiple such candidate paths and eliminates paths that violate threshold constraints.

The contributions of this work are threefold. First, a framework is developed for the calculation of the variance of P_D given a trajectory. The variance incorporates the aircraft state and radar state uncertainties and enables the mission planner to estimate unknown parameters with a distriution rather than a single value. Second, an error budget analysis for the resulting variance of P_D is developed using linear covariance analysis. Third, an iterative path planning technique based upon shortest path visibility graphs is created to demonstrate the ability to consider P_D uncertainty when planning.

The remainder of this paper is organized as follows. Section II-A presents the radar detection model which provides an expression for the probability of detection, the linearization of the model, and the incorporation of aircraft and radar state uncertainties. The aircraft state uncertainty is computed using an aided-INS as described in Section II-C. Section III describes the linear covariance model and the method for generating error budgets. Section IV describes the path planner that incorporates these components and the results of the path planner are provided in Section V.

II. Background and Previous Work

This section describes previous work that is relevant to the path planning application presented in this paper. The path planner seeks to keep P_D below a specified threshold while accounting for uncertainty in the aircraft and radar states. Section II-A describes the development of the radar detection model from [7] and the linearization of that model to obtain an expression for the variance of P_D as shown in [14, 22]. Section II-C details the INS model used in this paper to calculate the aircraft pose covariance. Finally, Section

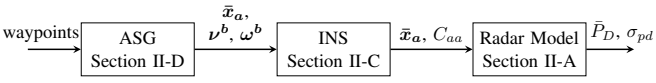

Fig. 1: Block diagram for components discussed in the background section.

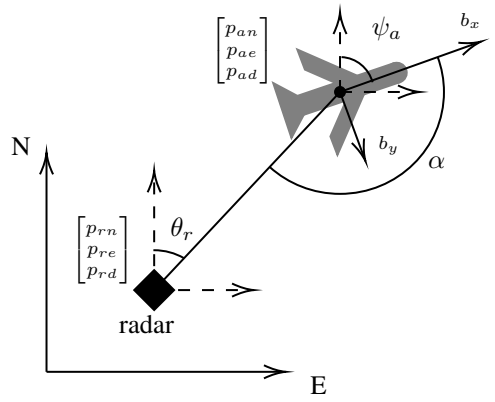

Fig. 2: Graphical representation of the quantities used in the radar detection model.

II-D describes the rapid aircraft state generation (ASG) used to create representative aircraft state and IMU measurements from smoothed piece-wise linear paths as presented in [23]. These measurements are used to propagate the aircraft state covariance. The block diagram in Fig. 1 shows the relationship of the ASG, INS, and radar model as described in this section.

A. Probability of Detection

The radar detection model used in this paper is presented in [7]. For sake of completeness, the main equations are provided in this section. The model includes expressions for the probability of detection, P_D, signal-to-noise ratio, $\mathcal{S}$, and RCS, σ_r. These quantities are functions of the aircraft pose, radar position, and radar parameters.

An accurate approximation to P_D, provided by North [7, 24], is

$$P_D \approx 0.5 \times \text{erfc}\left(\sqrt{-\ln P_{fa}} - \sqrt{\mathcal{S} + 0.5}\right) \tag{1}$$

where P_{fa} is the probability of false alarm, $\mathcal{S}$ is the signal-to-noise ratio, and erfc$(\cdot)$ is the complementary error function. The P_{fa} is considered a constant for a given radar, whereas $\mathcal{S}$ is a function of radar parameters and the pose of the target aircraft relative to the radar.

A general expression for the signal-to-noise ratio is given by

$$\mathcal{S} \quad = \quad c_r \frac{\sigma_r}{kR^4} \tag{2}$$

where k is Boltzmann's constant $(1.38 \times 10^{-23}\ J/^\circ K)$ and c_r is a radar constant that is a function of several radar parameters. These parameters include power, aperture area, noise figure, and loss factor. The specific equation for c_r is dependent on the type of radar being modeled [7].

The RCS, σ_r, and range, R, are functions of the aircraft pose and radar position as depicted in Fig. 2. The aircraft pose consists of the position in the North-East-Down (NED) frame, $\boldsymbol{p}_{\boldsymbol{a}}^{\boldsymbol{n}}$, and a vector of the Euler angles, $\boldsymbol{\Theta}_{\boldsymbol{a}}$, as described in [25]. The range to the radar is given by

$$R \quad = \quad ||\boldsymbol{p}_{\boldsymbol{a}}^{\boldsymbol{n}} - \boldsymbol{p}_{\boldsymbol{r}}^{\boldsymbol{n}}||_2 \tag{3}$$

where $\boldsymbol{p}_{\boldsymbol{r}}^{\boldsymbol{n}}$ represents the position of the radar in the NED frame.

The framework developed in [14, 22] supports several RCS models. In this paper, the ellipsoid RCS representation is used [4, 7, 14], which is a function of the RCS azimuth α and elevation ϕ angles and is given by

$$\sigma_r = \frac{\pi\,(abc)^2}{\left((a\,\mathrm{S}\alpha\,\mathrm{C}\phi)^2 + (b\,\mathrm{S}\alpha\,\mathrm{S}\phi)^2 + (c\,\mathrm{C}\alpha)^2\right)^2} \tag{4}$$

where a, b, and c are the length of the ellipsoid axes and S$\cdot$ and C$\cdot$ are the $\sin(\cdot)$ and $\cos(\cdot)$ functions. Equations for the RCS azimuth and elevation angles as functions of the aircraft pose and radar position are provided in [14, 22].

B. Uncertainty in Probability of Detection

The framework presented in [14, 22] provides a method for incorporating aircraft and radar state uncertainty into the calculation of P_D for a single-pulse radar detection model. The framework provides an expression for the variance of P_D given the covariance of the aircraft and radar states.

Let the aircraft state be $\boldsymbol{x}_{\boldsymbol{a}} = \begin{bmatrix}\boldsymbol{p}_{\boldsymbol{a}}^{\boldsymbol{n}} & \boldsymbol{\Theta}_{\boldsymbol{a}}\end{bmatrix}^\intercal$ and radar state be $\boldsymbol{x}_{\boldsymbol{r}} = \begin{bmatrix}\boldsymbol{p}_{\boldsymbol{r}}^{\boldsymbol{n}} & c_r\end{bmatrix}^\intercal$. The state vectors are represented as Gaussian distributed random variables with $\boldsymbol{x}_{\boldsymbol{a}} \sim \mathcal{N}(\bar{\boldsymbol{x}}_{\boldsymbol{a}}, C_{aa})$ and $\boldsymbol{x}_{\boldsymbol{r}} \sim \mathcal{N}(\bar{\boldsymbol{x}}_{\boldsymbol{r}}, C_{rr})$ where the bar notation is used to indicate the mean (or nominal). To find a linear approximation of P_D, $\boldsymbol{x}_{\boldsymbol{a}}$ and $\boldsymbol{x}_{\boldsymbol{r}}$ are both expressed as the sum of a nominal state and a perturbation as

$$\boldsymbol{x}_{\boldsymbol{a}} = \bar{\boldsymbol{x}}_{\boldsymbol{a}} + \delta\boldsymbol{x}_{\boldsymbol{a}} \tag{5}$$

$$\boldsymbol{x}_{\boldsymbol{r}} = \bar{\boldsymbol{x}}_{\boldsymbol{r}} + \delta\boldsymbol{x}_{\boldsymbol{r}}. \tag{6}$$

Because P_D is a nonlinear function of the aircraft and radar state, variability in $\boldsymbol{x}_{\boldsymbol{a}}$ and $\boldsymbol{x}_{\boldsymbol{r}}$ induce variability in P_D. Thus, P_D is expressed as the sum of a nominal and a perturbation as

$$P_D = \bar{P}_D + \delta P_D. \tag{7}$$

The perturbation, δP_D, is approximated, to the first order, by linearizing (1)-(4) about the nominal operating points $(\bar{\boldsymbol{x}}_{\boldsymbol{a}}, \bar{\boldsymbol{x}}_{\boldsymbol{r}})$ using a Taylor series expansion to obtain

$$\delta P_D \approx A_{Pa}\delta\boldsymbol{x}_{\boldsymbol{a}} + A_{Pr}\delta\boldsymbol{x}_{\boldsymbol{r}}. \tag{8}$$

The Jacobians A_{Pa} and A_{Pr} are the partial derivatives of P_D as defined in (1) with respect to $\boldsymbol{x}_{\boldsymbol{a}}$ and $\boldsymbol{x}_{\boldsymbol{r}}$, respectively. The partial derivatives are described in detail in [14, 22].

The variance of P_D due to aircraft and radar state covariance is computed by taking the expectation of δP_D^2 as

$$\sigma_{pd}^2 = E\left[\delta P_D^2\right] \tag{9}$$

$$= A_{Pa}C_{aa}A_{Pa}^\intercal + A_{Pr}C_{rr}A_{Pr}^\intercal. \tag{10}$$

These equations show that variability of P_D is a function of the Jacobians A_{Pa} and A_{Pr}, the covariance of the aircraft

state, C_{aa}, and the covariance of the radar state, C_{rr}. For the path planning application presented in this paper, C_{rr} is considered constant and C_{aa} is time-varying and obtained from a stochastic model of an inertial navigation system.

C. Inertial Navigation Model

The expression in (10) indicates that the variance of P_D is a function of the aircraft state covariance, C_{aa}. This section provides a method for calculating C_{aa} by modeling the covariance propagation of an aided-INS.

The INS used in this work is a continuous-time error-state EKF with discrete measurement updates for position, heading, and altitude. The covariance of the EKF is propagated with measurements from an IMU using the "model replacement" method [18]. The following paragraphs describe the method for propagating and updating the aircraft state covariance for the INS.

The error-state EKF estimates the difference between a truth and navigation model of the aircraft dynamics. For the development of this filter, let the truth model for the aircraft dynamics be defined as

$$\underbrace{\begin{bmatrix} \dot{\boldsymbol{p}}^n \\ \dot{\boldsymbol{v}}^n \\ \dot{q}_b^n \\ \dot{\boldsymbol{b}}_a^b \\ \dot{\boldsymbol{b}}_g^b \end{bmatrix}}_{\dot{\boldsymbol{x}}} = \underbrace{\begin{bmatrix} \boldsymbol{v}^n \\ T_b^n \boldsymbol{\nu}^b(t) + \boldsymbol{g}^n \\ \frac{1}{2} q_b^n \otimes \begin{bmatrix} 0 \\ \boldsymbol{\omega}^b(t) \end{bmatrix} \\ -\frac{1}{\tau_a} \boldsymbol{b}_a^b + \boldsymbol{w}_a \\ -\frac{1}{\tau_g} \boldsymbol{b}_g^b + \boldsymbol{w}_g \end{bmatrix}}_{\boldsymbol{f}(\boldsymbol{x},\boldsymbol{w},t)} \tag{11}$$

where the aircraft position, $\boldsymbol{p}^n$, and velocity, $\boldsymbol{v}^n$, are in the NED frame, the attitude quaternion, q_b^n, is the orientation of the body frame with respect to the NED frame, and the accelerometer bias $\boldsymbol{b}_a^b$, and gyro bias $\boldsymbol{b}_g^b$ are in the body frame. The matrix T_b^n is the transformation from the body frame to the NED frame associated with the attitude quaternion q_b^n and $\otimes$ represents the Hamiltonian quaternion product [26]. The accelerometer and gyro biases are modeled as Fist-Order Gauss Markov (FOGM) processes with time constants τ_a and τ_g and driving white noise of $\boldsymbol{w}_a$ and $\boldsymbol{w}_g$. The truth model is driven by the true specific force $\boldsymbol{\nu}^b$ and angular rate $\boldsymbol{\omega}^b$ of the aircraft body. This model is similar to navigation models presented in [15–17] with the addition of FOGM sensor biases as in [18].

The navigation model has the same states as the truth model but is driven by biased and noisy measurements from an IMU with

$$\underbrace{\begin{bmatrix} \dot{\hat{\boldsymbol{p}}}^n \\ \dot{\hat{\boldsymbol{v}}}^n \\ \dot{\hat{q}}_b^n \\ \dot{\hat{\boldsymbol{b}}}_a^b \\ \dot{\hat{\boldsymbol{b}}}_g^b \end{bmatrix}}_{\dot{\hat{\boldsymbol{x}}}} = \underbrace{\begin{bmatrix} \hat{\boldsymbol{v}}^n \\ \hat{T}_b^n \left(\tilde{\boldsymbol{\nu}}^b(t) - \hat{\boldsymbol{b}}_a \right) + \boldsymbol{g}^n \\ \frac{1}{2} \hat{q}_b^n \otimes \begin{bmatrix} 0 \\ \tilde{\boldsymbol{\omega}}^b(t) - \hat{\boldsymbol{b}}_g^b \end{bmatrix} \\ -\frac{1}{\tau_a} \hat{\boldsymbol{b}}_a^b \\ -\frac{1}{\tau_g} \hat{\boldsymbol{b}}_g^b \end{bmatrix}}_{\hat{\boldsymbol{f}}(\hat{\boldsymbol{x}},\tilde{\boldsymbol{y}},t)}. \tag{12}$$

where the hat symbol ($\hat{\boldsymbol{x}}$) is used to indicate navigation model states. The IMU measurements are provided by a three-axis accelerometer and gyro and are corrupted by bias and noise given by

$$\underbrace{\begin{bmatrix} \tilde{\boldsymbol{\nu}}^b(t) \\ \tilde{\boldsymbol{\omega}}^b(t) \end{bmatrix}}_{\tilde{\boldsymbol{y}}} = \underbrace{\begin{bmatrix} \boldsymbol{\nu}^b(t) + \boldsymbol{b}_a^b \\ \boldsymbol{\omega}^b(t) + \boldsymbol{b}_g^b \end{bmatrix}}_{\boldsymbol{c}(\boldsymbol{x},\boldsymbol{u})} + \underbrace{\begin{bmatrix} \boldsymbol{n}_\nu \\ \boldsymbol{n}_\omega \end{bmatrix}}_{\boldsymbol{\eta}}. \tag{13}$$

where $\boldsymbol{n}_\nu \sim \mathcal{N}(0, Q_\nu)$ and $\boldsymbol{n}_\omega \sim \mathcal{N}(0, Q_\omega)$.

The EKF states are updated by discrete-time measurements using the Kalman update equation

$$\hat{\boldsymbol{x}}_k^+ = \hat{\boldsymbol{x}}_k^- + K_k \left[\tilde{\boldsymbol{z}}_k - \hat{\tilde{\boldsymbol{z}}}_k \right] \tag{14}$$

where K_k is the Kalman gain. The measurements are generated with

$$\tilde{\boldsymbol{z}}_k = \boldsymbol{h}(\boldsymbol{x}_k) + \boldsymbol{\nu}_k \tag{15}$$

and the expected measurement is given by

$$\hat{\tilde{\boldsymbol{z}}}_k = \hat{\boldsymbol{h}}\left(\hat{\boldsymbol{x}}_k\right). \tag{16}$$

The INS in this paper processes discrete-time measurements for position, heading, and altitude corrupted by additive white noise as

$$\tilde{\boldsymbol{p}}^n\left[t_k\right] = \boldsymbol{p}^n\left[t_k\right] + \boldsymbol{n}_p\left[t_k\right] \tag{17}$$

$$\tilde{\psi}\left[t_k\right] = \psi\left[t_k\right] + n_\psi\left[t_k\right] \tag{18}$$

$$\tilde{h}\left[t_k\right] = h\left[t_k\right] + n_h\left[t_k\right] \tag{19}$$

where

$$\boldsymbol{n}_p \sim \mathcal{N}\left(\boldsymbol{0}_{3\times 1}, R_p = \text{diag}\left(\sigma_n^2,\ \sigma_e^2,\ \sigma_d^2\right)\right) \tag{20}$$

$$n_\psi \sim \mathcal{N}\left(0, R_\psi = \sigma_\psi^2\right) \tag{21}$$

and

$$n_h \sim \mathcal{N}\left(0, R_h = \sigma_h^2\right). \tag{22}$$

The error states of the EKF are defined as the difference between the true and navigation states given by

$$\delta \boldsymbol{x}_e = \boldsymbol{x} - \hat{\boldsymbol{x}}. \tag{23}$$

where the difference is defined by subtraction for all but the attitude states. The attitude difference is defined using quaternion arithmetic as

$$\begin{bmatrix} 1 \\ -\frac{1}{2}\delta\boldsymbol{\theta}_b^n \end{bmatrix} = q_b^n \otimes (\hat{q}_b^n)^* \tag{24}$$

where $(\hat{q}_b^n)^*$ represents the quaternion conjugate of the navigation attitude quaternion and $\delta\boldsymbol{\theta}_b^n$ is the error rotation vector. The error state vector is then given by

$$\delta \boldsymbol{x}_e = \begin{bmatrix} \delta\boldsymbol{p}^n & \delta\boldsymbol{v}^n & \delta\boldsymbol{\theta}_b^n & \delta\boldsymbol{b}_a^b & \delta\boldsymbol{b}_g^b \end{bmatrix}^\intercal. \tag{25}$$

The error state dynamics are linearized about the nominal aircraft trajectory to obtain

$$\delta\dot{\boldsymbol{x}}_e = \hat{F}\delta\boldsymbol{x} + \hat{B}\boldsymbol{w_e} \tag{26}$$

where $\hat{F}$ is the linearized error state dynamics matrix given by

$$\hat{F} = \begin{bmatrix} \mathbf{0} & \boldsymbol{I} & \mathbf{0} & \mathbf{0} & \mathbf{0} \\ \mathbf{0} & \mathbf{0} & \left[\hat{T}_b^n \left(\tilde{\boldsymbol{\nu}}^b - \hat{\boldsymbol{b}}_a^b\right)\right] \times & -\hat{T}_b^n & \mathbf{0} \\ \mathbf{0} & \mathbf{0} & \mathbf{0} & \mathbf{0} & \hat{T}_b^n \\ \mathbf{0} & \mathbf{0} & \mathbf{0} & -\frac{1}{\tau_a}\boldsymbol{I} & \mathbf{0} \\ \mathbf{0} & \mathbf{0} & \mathbf{0} & \mathbf{0} & -\frac{1}{\tau_g}\boldsymbol{I} \end{bmatrix} \quad (27)$$

and $\hat{B}$ is the noise mixing matrix given by

$$\hat{B} = \begin{bmatrix} \mathbf{0} & \mathbf{0} & \mathbf{0} & \mathbf{0} \\ -\hat{T}_b^n & \mathbf{0} & \mathbf{0} & \mathbf{0} \\ \mathbf{0} & \hat{T}_b^n & \mathbf{0} & \mathbf{0} \\ \mathbf{0} & \mathbf{0} & \boldsymbol{I} & \mathbf{0} \\ \mathbf{0} & \mathbf{0} & \mathbf{0} & \boldsymbol{I} \end{bmatrix}. \quad (28)$$

The boldface $\mathbf{0}$ and $\boldsymbol{I}$ entries represent 3×3 zero matrix and identity matrix, respectively. The additive white noise vector, $\boldsymbol{w_e}$, consists of the accelerometer and gyro measurement noise as well as the process noise of the FOGM biases

$$\boldsymbol{w_e} = \begin{bmatrix} \boldsymbol{n}_\nu & \boldsymbol{n}_\omega & \boldsymbol{w}_a & \boldsymbol{w}_g \end{bmatrix}^T \quad (29)$$

which has power spectral density, Q, defined by

$$E\left[\boldsymbol{w_e}(t)\,\boldsymbol{w_e}(t')^T\right] = Q\delta(t-t') \quad (30)$$

where

$$Q = \begin{bmatrix} Q_\nu & \mathbf{0} & \mathbf{0} & \mathbf{0} \\ \mathbf{0} & Q_\omega & \mathbf{0} & \mathbf{0} \\ \mathbf{0} & \mathbf{0} & q_a\boldsymbol{I} & \mathbf{0} \\ \mathbf{0} & \mathbf{0} & \mathbf{0} & q_g\boldsymbol{I} \end{bmatrix} \quad (31)$$

and

$$q_a = \frac{2\sigma_{a,ss}^2}{\tau_a} \quad (32)$$

$$q_g = \frac{2\sigma_{g,ss}^2}{\tau_g}. \quad (33)$$

The state covariance, P, is propagated with the continuous Ricatti equation given by

$$\dot{P} = \hat{F}P + P\hat{F}^\intercal + \hat{B}Q\hat{B}^\intercal. \quad (34)$$

In implementation, the continuous Ricatti equation is often replaced by a more efficient discrete-time propagation equation that uses the state transition matrix [27]. The path planner presented in this paper uses such a method where the state transition matrix is approximated using Lear's method [28]. More details about Lear's method and this covariance propagation approach are provided in Appendix B.

The EKF state covariance is updated at the discrete measurement times using the Joseph form [18] as

$$P_k^+ = (I - K_k H_k) P_k^- (I - K_k H_k)^T + K_k R_\nu K_k^T \quad (35)$$

where K_k and H_k are the Kalman gain and the measurement model Jacobian for the measurement being processed. The measurement model Jacobian for the position, altitude, and heading measurements are given by

$$H_p = \begin{bmatrix} I_{3\times3} & 0_{3\times3} & 0_{3\times3} & 0_{3\times3} & 0_{3\times3} \end{bmatrix} \quad (36)$$

$$H_h = \begin{bmatrix} 0 & 0 & -1 & 0_{1\times3} & 0_{1\times3} & 0_{1\times3} & 0_{1\times3} \end{bmatrix} \quad (37)$$

and

$$H_\psi = \begin{bmatrix} 0_{1\times3} & 0_{1\times3} & 0 & 0 & -1 & 0_{1\times3} & 0_{1\times3} \end{bmatrix}. \quad (38)$$

The Kalman gain, K_k, is calculated with

$$K_k = P_k^- H_k \left(H_k P_k^- H_k^T + R_\nu\right)^{-1}. \quad (39)$$

The INS state vector defined in this section differs from the aircraft state vector used in the radar detection model in Section II-A. The primary difference is that $\boldsymbol{x_a}$ is a reduced set of states and the attitude is represented by a vector of Euler angles instead of a quaternion. The aircraft state covariance, C_{aa}, used in the radar detection model is a transformation of the EKF state covariance estimated by the navigation model given by

$$C_{aa}(t) = M_a P(t) M_a^\intercal \quad (40)$$

where M_a is derived in Appendix A.

D. Aircraft State and IMU Generation

The previous section shows that the aircraft state covariance, C_{aa}, is propagated using the aircraft states, process noise and bias parameters, and measured accelerations from an IMU (i.e., $\tilde{\boldsymbol{\nu}}^{\boldsymbol{b}}$ in (27)). The process noise and bias parameters are constant for a given scenario, however the aircraft states and IMU measurements must be generated for each candidate path considered by the path planner. To enable rapid planning, an efficient aircraft state and IMU measurement generator is desired. This paper uses the ASG method presented in [23] to accomplish this task.

The ASG method converts a series of 2D waypoints to a smooth flyable trajectory constrained by maximum curvature and maximum curvature rate. The waypoint path is smoothed using fillets with line, arc, and clothoid [29] segments. The nominal aircraft position, heading, and curvature are obtained using the path segment geometry equations. For example, the clothoid segment geometry is defined by

$$x(s) = x_0 + \int_0^s \cos(0.5\kappa'\xi^2 + \kappa_0\xi + \psi_0)d\xi \quad (41)$$

$$y(s) = y_0 + \int_0^s \sin(0.5\kappa'\xi^2 + \kappa_0\xi + \psi_0)d\xi \quad (42)$$

$$\psi(s) = \psi_0 + \kappa_0 s + 0.5\kappa' s^2 \quad (43)$$

$$\kappa(s) = \kappa_0 + \kappa' s \quad (44)$$

where s is the length along the segment, ψ_0 is the initial heading, κ_0 is the initial curvature, x_0 and y_0 represent the starting point, and κ' is the curvature rate per unit length of the segment. This approach enables efficient generation of nominal aircraft states that adhere to a flyable trajectory given the vehicle maneuver constraints.

In the ASG method, the pitch angle, θ_a, is a constant trim value and the roll angle, ϕ_a, is obtained from a coordinated turn model [25]. The coordinated turn model provides a relationship between the heading rate and roll angle of the aircraft as

$$\dot{\psi_a} = \frac{g}{\dot{s}}\tan\phi_a \quad (45)$$

where ψ_a and ϕ_a are the Euler angles for yaw and roll, g is the acceleration due to gravity, and $\dot{s}$ is the speed of the aircraft.

The final stage of the ASG method uses the Euler angles and Euler angle rates along the segments to calculate the specific force and angular rates experienced by the aircraft body when following the smoothed path. The ASG method in [23] shows that the true specific force is given by

$$\boldsymbol{\nu}^b = T_n^b \begin{bmatrix} \ddot{s}\cos(\psi_a) - \dot{s}\dot{\psi}_a \sin(\psi_a) \\ \ddot{s}\sin(\psi_a) + \dot{s}\dot{\psi}_a \cos(\psi_a) \\ -g \end{bmatrix} \tag{46}$$

and the angular rates are given by

$$\boldsymbol{\omega}^b = \begin{bmatrix} \ddot{\psi}_a \frac{\dot{s}}{g}\cos^2\phi - \dot{\psi}_a \sin\theta_a \\ \dot{\psi}_a \sin\phi\cos\theta_a \\ \dot{\psi}_a \cos\phi\cos\theta_a \end{bmatrix} \tag{47}$$

where $\ddot{s}$ is the acceleration in the direction of the path, and T_n^b is the rotation matrix from the NED frame to the body frame.

The quantities generated from ASG are used as the nominal aircraft states, $\bar{\boldsymbol{x}}_{\boldsymbol{a}}$, true specific force, $\boldsymbol{\nu^b}$, and true angular rates, $\boldsymbol{\omega^b}$. These quantities are used by the INS model in Section II-C to calculate the aircraft state covariance C_{aa}, which is used by the radar detection model from Section II-A to calculate the variance of P_D, σ_{pd}^2. The remainder of this paper shows how these elements are combined into a path planner that incorporates uncertainty in the aircraft and radar states.

III. Error Budgets and Linear Covariance

The INS model described in Section II-C is used to estimate the uncertainty of a navigation state due to biased and noisy sensor measurements. One approach to analyze the performance of the INS, is to generate error budgets that provide a graphical representation of the contribution of each source of uncertainty on the overall estimation uncertainty. This section describes error budgets in more detail and derives a linear covariance model that is used to efficiently generate error budgets.

A. Error Budgets

Error budgets are generated from statistical information typically obtained through several Monte Carlo analyses [17, 18]. In this approach, a Monte Carlo analysis is first performed with all uncertainty sources activated. Then the Monte Carlo analysis is repeated for each source of uncertainty where a single source is activated and all other sources are de-activated (i.e. noise samples set to zero). The ensemble statistics for each Monte Carlo analysis are used to estimate the time-varying navigation error covariance, P_{true}, due to the activated uncertainty source.

The error budget generation method is used to analyze the effect of the sources of uncertainty on the overall navigation error covariance. For the radar detection path planning application, the error budget of interest is the effect of the sources of uncertainty on the variability of P_D. This introduces two additional uncertainty sources to be evaluated (i.e., radar position and radar constant). The effect of each source of uncertainty on P_D is analyzed by turning off all sources of uncertainty except the one being evaluated and calculating the variance of P_D using (10). Once all sources of uncertainty have been evaluated, the variance of P_D calculated during each test can be compared in an error budget.

The P_D error budget analysis includes eight Monte Carlo analyses with each requiring hundreds or thousands of navigation system simulations along the reference trajectory. The high computational burden of this analysis prohibits its use in the proposed path planning framework. An alternative method to compute the navigation error covariance is linear covariance analysis (LinCov) [18, 20, 21]. LinCov uses linear models for the truth and navigation states to efficiently generate the navigation error covariance along a reference trajectory. This approach generates the same statistical information as a Monte Carlo analysis, but requires only a single simulation over the reference trajectory. Thus, the error budget analysis described in this section can be performed with only eight simulations over the reference trajectory. The following section describes the LinCov models used in this paper to obtain the true navigation error covariance P_{true}.

B. Linear Covariance Model

This section describes the LinCov model associated with the truth and navigation models developed in Section II-C. The LinCov model forms an augmented state vector of the truth and navigation states and the associated linearized augmented system matrices. The notation used in this section follows the development in [21].

The linearized truth state dispersion dynamics are determined by taking the Jacobian of the truth model defined in (11) to obtain

$$\delta\dot{\boldsymbol{x}} = F_x \delta\boldsymbol{x} + B\boldsymbol{w} \tag{48}$$

where the uppercase letters represent the partial derivative of an equation taken with respect to the variable in the subscript. For example, $F_{\boldsymbol{x}}$ is the partial derivative of $\boldsymbol{f}(\cdot)$, as defined in (11), with respect to the truth state, $\boldsymbol{x}$, evaluated at the nominal truth state, $\bar{\boldsymbol{x}}$. Given this definition, the matrices in (48) are defined as

$$F_x = \begin{bmatrix} \mathbf{0} & \boldsymbol{I} & \mathbf{0} & \mathbf{0} & \mathbf{0} \\ \mathbf{0} & \mathbf{0} & \left(\bar{T}_b^n \boldsymbol{\nu}^b\right)\times & \mathbf{0} & \mathbf{0} \\ \mathbf{0} & \mathbf{0} & \mathbf{0} & \mathbf{0} & \mathbf{0} \\ \mathbf{0} & \mathbf{0} & \mathbf{0} & -\frac{1}{\tau_a}\boldsymbol{I} & \mathbf{0} \\ \mathbf{0} & \mathbf{0} & \mathbf{0} & \mathbf{0} & -\frac{1}{\tau_g}\boldsymbol{I} \end{bmatrix} \tag{49}$$

and

$$B = \begin{bmatrix} \mathbf{0}_{9\times 6} \\ I_{6\times 6} \end{bmatrix}. \tag{50}$$

The additive white noise vector is given by

$$\boldsymbol{w} = \begin{bmatrix} \boldsymbol{w}_a \\ \boldsymbol{w}_g \end{bmatrix} \tag{51}$$

where $\boldsymbol{w}_a$ and $\boldsymbol{w}_g$ are defined in (29)-(33).

The linearized navigation state dispersion dynamics are determined by taking the Jacobian of the navigation model defined in (12) to obtain

$$\delta\dot{\hat{\boldsymbol{x}}} = \hat{F}_{\hat{x}}\delta\hat{\boldsymbol{x}} + \hat{F}_{\tilde{y}}C_x\delta\boldsymbol{x} + \hat{F}_{\tilde{y}}\boldsymbol{\eta} \tag{52}$$

where

$$\hat{F}_{\hat{x}} = \begin{bmatrix} \mathbf{0} & \boldsymbol{I} & \mathbf{0} & \mathbf{0} & \mathbf{0} \\ \mathbf{0} & \mathbf{0} & \left[\hat{\hat{T}}_b^n\left(\boldsymbol{\nu}^b - \hat{\hat{\boldsymbol{b}}}_a\right)\right]\times & -\hat{\hat{T}}_b^n & \mathbf{0} \\ \mathbf{0} & \mathbf{0} & \mathbf{0} & \mathbf{0} & \hat{\hat{T}}_b^n \\ \mathbf{0} & \mathbf{0} & \mathbf{0} & -\frac{1}{\tau_a}\boldsymbol{I} & \mathbf{0} \\ \mathbf{0} & \mathbf{0} & \mathbf{0} & \mathbf{0} & -\frac{1}{\tau_a}\boldsymbol{I} \end{bmatrix} \tag{53}$$

$$\hat{F}_{\tilde{y}} = \begin{bmatrix} \mathbf{0} & \mathbf{0} \\ \hat{\hat{T}}_b^n & \mathbf{0} \\ \mathbf{0} & -\hat{\hat{T}}_b^n \\ \mathbf{0} & \mathbf{0} \\ \mathbf{0} & \mathbf{0} \end{bmatrix} \tag{54}$$

and

$$C_x = \begin{bmatrix} 0_{6\times9} & I_{6\times6} \end{bmatrix}_{6\times15}. \tag{55}$$

The truth state update is linearized to obtain

$$\delta\boldsymbol{x}_k^+ = \delta\boldsymbol{x}_k^-. \tag{56}$$

The navigation state update equation defined in (14) is also linearized to produce the dispersion update equation given by

$$\delta\hat{\boldsymbol{x}}_k^+ = \left(I_{16\times16} - \hat{K}_k\hat{H}_{\hat{x}}\right)\delta\hat{\boldsymbol{x}}_k^- + \hat{K}_kH_x\delta\boldsymbol{x}_k^- + \hat{K}_k\boldsymbol{\nu}_k \tag{57}$$

where the H matrices depend on the measurement update type and are defined in (36)-(38). Note that for the measurement models used in this paper, $H_x = \hat{H}_{\hat{x}}$.

The linearized truth and navigation models are combined to form the augmented system model. The augmented system state vector for the linearized dispersion models is formed as

$$\boldsymbol{X} = \begin{bmatrix} \delta\boldsymbol{x} \\ \delta\hat{\boldsymbol{x}} \end{bmatrix} \tag{58}$$

and the augmented propagation and update equations are

$$\dot{\boldsymbol{X}} = \mathcal{F}\boldsymbol{X} + \mathcal{G}\boldsymbol{\eta} + \mathcal{W}\boldsymbol{w} \tag{59}$$

$$\boldsymbol{X}_k^+ = \mathcal{A}_k\boldsymbol{X}_k^- + \mathcal{B}_k\boldsymbol{\nu}_k \tag{60}$$

where

$$\mathcal{F} = \begin{bmatrix} F_x & 0 \\ \hat{F}_{\tilde{y}}C_x & \hat{F}_{\hat{x}} \end{bmatrix} \tag{61}$$

$$\mathcal{G} = \begin{bmatrix} 0 \\ \hat{F}_{\tilde{y}} \end{bmatrix} \tag{62}$$

$$\mathcal{W} = \begin{bmatrix} B \\ 0_{16\times6} \end{bmatrix} \tag{63}$$

$$\mathcal{A}_k = \begin{bmatrix} I_{16\times16} & 0_{16\times16} \\ K_kH_x & I_{16\times16} - K_k\hat{H}_{\hat{x}} \end{bmatrix} \tag{64}$$

$$\mathcal{B}_k = \begin{bmatrix} 0_{16\times n_z} \\ K_k \end{bmatrix} \tag{65}$$

and n_z is dimension of the discrete-time measurement being processed.

Finally, the covariance propagation and update of the augmented system is expressed as

$$E\left[\dot{\boldsymbol{X}}\dot{\boldsymbol{X}}^T\right] = \dot{C}_A = \mathcal{F}C_A + C_A\mathcal{F}^T + \mathcal{G}S_\eta\mathcal{G}^T + \mathcal{W}S_w\mathcal{W}^T \tag{66}$$

$$E\left[\boldsymbol{X}_k^+\boldsymbol{X}_k^{+T}\right] = C_A^+ = \mathcal{A}_kC_A^-\mathcal{A}_k^T + \mathcal{B}_kR_\nu\mathcal{B}_k^T \tag{67}$$

where the power spectral density of the inertial measurements and process noise are

$$S_\eta = \begin{bmatrix} Q_\nu & 0_{3\times3} \\ 0_{3\times3} & Q_\omega \end{bmatrix} \tag{68}$$

$$S_w = \begin{bmatrix} q_a\boldsymbol{I} & 0_{3\times3} \\ 0_{3\times3} & q_g\boldsymbol{I} \end{bmatrix} \tag{69}$$

and Q_ν, Q_ω, q_a, and q_g are defined in (30)-(33).

The quantity of interest for this paper is the navigation estimation error. It is important to note that the navigation error covariance defined below is the true navigation error covariance, which may be different than the estimated navigation covariance from the Kalman filter. This quantity is extracted from the augmented covariance matrix via

$$P_{true} = \begin{bmatrix} -I & I_{16\times16} \end{bmatrix} C_A \begin{bmatrix} -I & I_{16\times16} \end{bmatrix}^T. \tag{70}$$

Note that the error budget and linear covariance models developed in this section evaluate the variability in P_D due to uncertainty in the aircraft INS and the radar states. This approach evaluates knowledge errors due to the sources of uncertainty rather than vehicle dispersions that are affected by disturbances such as wind, or guidance and control designs. This is convenient for the path planning application because it requires less computation than the vehicle dispersion analysis. Furthermore, the navigation errors are a good approximation of the vehicle dispersions when the control authority of the vehicle is sufficient to follow the planned path in the presence of disturbances. If an analysis of the vehicle dispersions is desired, then a closed-loop LinCov model as developed in [21] could be used in the framework presented in this paper.

IV. Application: Visibility Graph Planner

The methods presented in this paper can be used to inform a variety of radar detection path planning algorithms. This section presents an application of these methods to a visibility graph path planner. The following subsections describe the visibility graph path planner and an associated extension to incorporate the radar detection framework discussed in the previous sections.

A. General Visibility Graph Path Planner

The visibility graph path planner finds the shortest path between a start and goal location while navigating around obstacles. The nodes in the graph are the start and goal points and the vertices of the obstacles. Each node is connected by edges to every "visible" node. In this context, a node is visible if a line segment to the node does not pass through an obstacle. The edge cost is set to the Euclidean distance of the edge. The

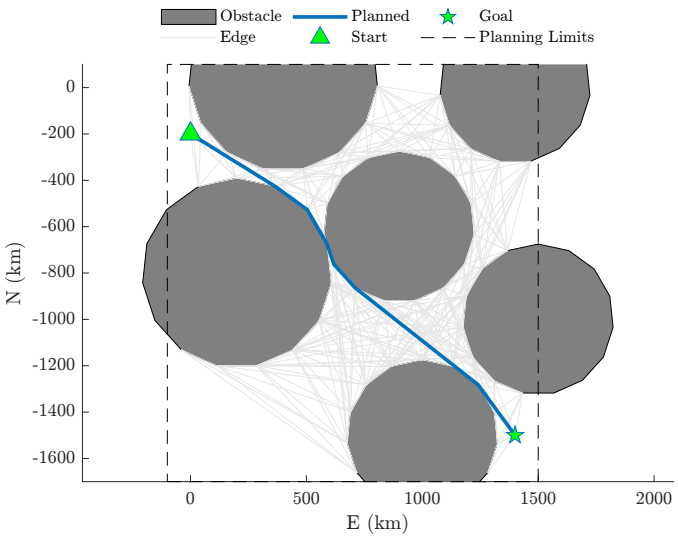

Fig. 3: Visibility graph example with six polygon obstacles (dark gray) where the light gray lines represent the edges of the visibility graph

shortest path (the path with the least cost) between the goal and target vertices is found using a graph search algorithm such as Dijkstra's [30] or A* [31].

Fig. 3 shows an example of a visibility graph applied to a path planning problem where the gray lines represent the edges of the graph, and the gray polygons are the obstacles. The blue line is the shortest path between the start point (triangle) and the goal point (star) that was found using a shortest path algorithm. The visibility graph method relies on the assumption that the shortest path through an obstacle field will touch the edges of the obstacles if a single straight segment between the start point and goal point is not valid.

The visibility graph planner described in this section is sufficient for radar detection planning with constant RCS and no uncertainty. The following subsection describes an extension to the visibility graph path planning algorithm to incorporate the methods presented in this paper. The resulting algorithm generates a path that maintains P_D below a specified threshold and accounts for varying RCS and uncertainty in the aircraft and radar states.

B. Visibility Graph Extension

A block diagram for the P_D visibility graph (PDVG) algorithm is shown in Fig. 4 where the Aircraft and Radar Models block is expanded in Fig. 1. The algorithm represents the radar detection region with polygons so that a visibility graph problem can be formulated and solved to efficiently produce a candidate path. The path is smoothed to provide continuous heading and curvature using the fillet method described in Section II-D. Once smoothed, the navigation covariance is propagated along the path using the INS model described in Section II-C. Finally, the radar detection model from Section II-A is used to determine if the probability of detection stays within the user-specified requirements. If the smoothed path satisfies the threshold, the algorithm is complete. Otherwise, the radar polygons are expanded based on the radar detection information and a new plan is generated using expanded polygons. The following paragraphs will describe these steps in more detail.

1) Initial Radar Polygons: The first step of the algorithm is to construct the initial radar detection polygons. The detection polygons are parameterized by a position, number of vertices, and a radius. The position of the radar, $\boldsymbol{p_r^n}$, is the center of the detection polygon. The number of vertices is a design decision by the user and the radius is determined by solving (1) and (2) for R as

$$R = \left(\frac{c_r \sigma_r}{k \left(\text{erfcinv}\left(2P_{D,\text{init}}\right) - \sqrt{-\log P_{fa}}\right)^2 - 0.5} \right)^{\frac{1}{4}}. \tag{71}$$

where $P_{D,\text{init}}$ is a P_D value used to construct the polygons, and σ_r is a nominal RCS value for the aircraft. Typically, $P_{D,\text{init}}$ is the same or slightly lower than the mission P_D threshold P_{DT}, and σ_r is the average RCS value of the chosen RCS model.

2) Visibility Graph Planner: The visibility graph planner uses the radar polygons to build a visibility graph and calculates the shortest path from the start point to the goal point. The resulting path is a series of waypoints that mark a path through the planning region.

3) Aircraft and Radar Models: The Aircraft and Radar Models are used to generate samples of P_D and σ_{pd} from a series of waypoints. The ASG method from [23] and summarized in Section II-D generates a flyable trajectory from the waypoints. The flyable trajectory includes nominal aircraft states, $\bar{\boldsymbol{x}}_{\boldsymbol{a}}$, and nominal IMU measurement samples ($\boldsymbol{\nu^b}$, $\boldsymbol{\omega^b}$) along the path. The inertial navigation model uses the nominal aircraft states and IMU measurements to compute the aircraft state covariance, C_{aa}, along the candidate path using the methods described in Section II-C.

The nominal aircraft state and aircraft state covariance are used to calculate the time-varying nominal $\bar{P}_D(t)$ using (1) and the variance of P_D, $\sigma_{pd}^2(t)$, using (10). The variance of P_D along the nominal trajectory, as defined in (10), is modified for the multiple-radar scenario such that, for the i^{th} radar, σ_{pd} is given by

$$\begin{aligned}\sigma_{pd,i}^2(t) =& A_{Pa,i}(t) C_{aa}(t) A_{Pa,i}(t)^\intercal \\ &+ A_{Pr,i}(t) C_{rr,i} A_{Pr,i}(t)^\intercal. \end{aligned} \tag{72}$$

4) Check Path Validity: The $\bar{P}_{D,i}$ and $\sigma_{pd,i}$ are used to determine if the candidate path is valid. For this application, a path is considered valid if the nominal P_D plus a multiple of σ_{pd} stays below a specified P_D threshold, P_{DT}, for all time as described below. Let m_σ be a mission planner specified multiple of the standard deviation of P_D. Then a path is considered valid if

$$\bar{P}_{D,i}(t) + m_\sigma \sigma_{pd,i}(t) \quad < \quad P_{DT} \qquad \forall\, t, i. \tag{73}$$

Note that the σ_{pd} value calculated with the linearized radar detection model using (10) represents the standard deviation of a Gaussian distribution. So the m_σ multiple follows the empirical rule such that one, two, and three deviations

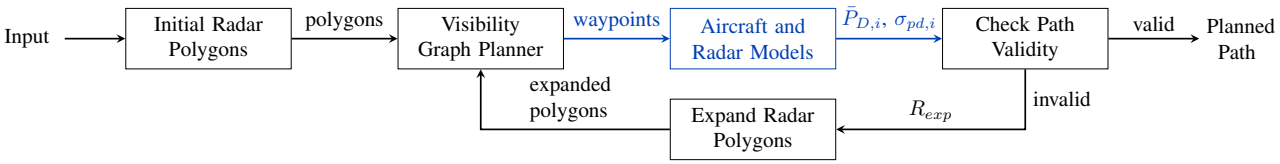

Fig. 4: Block diagram for the PDVG path planner. The Aircraft and Radar Models block in blue is expanded in Fig. 1.

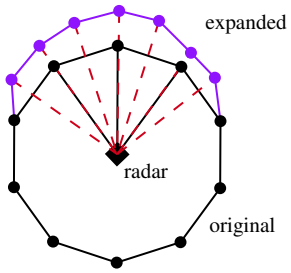

Fig. 5: Radar expansion diagram. The black polygon represents the original polygon, the blue segments represent the polygon expansion, and the dashed red lines show the expansion vertices. Vertices of the original and expanded polygons are represented by black and blue circles, respectively.

will contain 68%, 95%, and 99.7% of samples from the distribution, respectively.

5) Radar Polygon Expansion: If a candidate path passes the validity check in (73) for all time and every radar, the algorithm terminates and the candidate path is provided as the planned path. Otherwise, the detection statistics are used to expand the radar polygons.

The radar polygon expansion component expands the polygons in areas where the candidate path was invalid according to (73). The polygon expansion is shown graphically in Fig. 5 and is accomplished in two steps as described in the following paragraphs.

First, an expansion range is determined using $\bar{P}_{D,i}$ and $\sigma_{pd,i}$ for all samples where the path is invalid according to (73). The objective of the expansion range is to move the nominal path away from the radar to pass the validity check in (73). This is accomplished by determining an expansion P_D, $P_{D,exp}$, that when added to $m_\sigma \sigma_{pd}$ stays below P_{DT}. Let $P_{D,exp}$ for the i^{th} radar be defined as

$$P_{D,exp,i}(t) \quad = \quad \max\left(P_{DT} - m_\sigma \sigma_{pd,i}(t),\, 1e^{-3}\right) \quad (74)$$

where the max() function is used to ensure that $P_{D,exp,i}$ is positive and avoids the asymptote of the erfcinv() function at zero. Then the associated expansion range $R_{exp,i}(t)$ is determined by solving (71) with $P_{D,\text{init}} = P_{D,exp,i}(t)$ and $\sigma_r = \sigma_{r,i}(t)$.

Second, the expansion ranges calculated in the first step are applied to the closest radar polygon vertices. Then vertices are added to the polygon near the expanded vertices with the same expansion range as represented in Fig. 5.

The expanded radar polygons are provided to the visibility graph component and the algorithm continues until a valid path is found. The iterative nature of this algorithm allows the visibility graph component to provide a new candidate path according to the expanded obstacles.

TABLE I: Common parameters for the scenarios in this section.

Param	Value	Description
a	0.18 m	Ellipsoid RCS forward axis length
b	0.17 m	Ellipsoid RCS side axis length
c	0.20 m	Ellipsoid RCS up axis length
σ_{pr}	500/3 m	Radar position std. dev.
σ_{cr}	2/3 $\text{Jm}^2/^\circ\text{K}$	Radar constant std. dev.
p_{ad}	-3.5 km	Nominal aircraft position - "D" axis
$\boldsymbol{p}^{\boldsymbol{n}}_{\boldsymbol{r,1}}$	$\mathbf{0_{3\times 1}}$ km	Radar 1 nominal position (NED)
$\boldsymbol{p}^{\boldsymbol{n}}_{\boldsymbol{r,2}}$	[-650, 900, 0]$^\intercal$ km	Radar 2 nominal position (NED)
c_r	164.7 $\text{Jm}^2/^\circ\text{K}$	Nominal radar constant
P_{fa}	1×10^{-9}	Probability of false alarm
$\boldsymbol{p}^{\boldsymbol{n}}_{\text{start}}$	[-100, -700, -3.5]$^\intercal$ km	Start position
$\boldsymbol{p}^{\boldsymbol{n}}_{\text{goal}}$	[-400, 1650, -3.5]$^\intercal$ km	Goal position
$P_{D,\text{init}}$	0.1	P_D used for initial vgraph
$\sigma_{r,\text{init}}$	0.09 m^2	RCS used for initial vgraph
n_p	30	# of radar polygon vertices
P_{DT}	0.1	P_D threshold for planner
σ_n	1/3 m	North position noise std. dev.
σ_e	1/3 m	East position noise std. dev.
σ_d	1 m	Down position noise std. dev.
σ_h	0.1/3 m	Altitude noise std. dev.
σ_ψ	0.1/3 deg.	Heading noise std. dev.

V. Results

The results in this section illustrate the performance of the PDVG path planner described in Section IV-B for three scenarios. The planner seeks to satisfy (73) with a threshold of $P_{DT} = 0.1$ and $m_\sigma = 3$. The results for each scenario include a 2D map of the planning region, P_D calculated along the planned trajectory, and an error budget for the sources of uncertainty. The common parameters for the three scenarios are provided in Table I and the ellipsoid RCS model as a function of azimuth and elevation angles are shown in Fig. 6.

The three scenarios include a start point, goal point, radar systems and "planning limits" in which the planned path must remain. Fig. 7 shows the map for Scenario 1 with the start (triangle) and goal (star) points. The diamonds represent the position of the radar systems and the gray circles surrounding the diamonds show the radar detection regions. The radius of the radar detection regions are determined using (71) with $\sigma_r = 0.15$ m^2 and $P_{D,\text{init}} = 0.01$. These quantities were chosen so that the radar detection region would reflect a worst-case scenario for the RCS and a very low P_D value. The scenarios in this section will compare the effect of the IMU

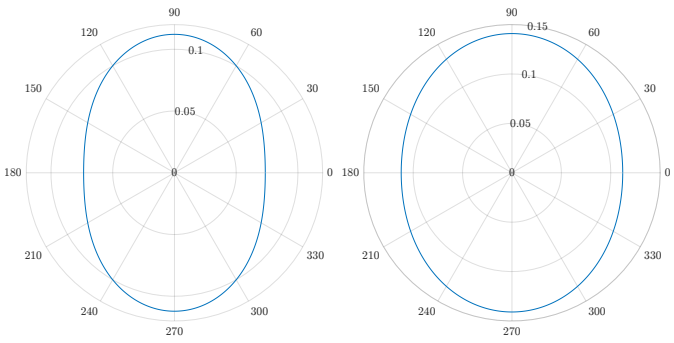

(a) RCS Azimuth (α) (b) RCS Elevation (ϕ)

Fig. 6: Ellipsoid RCS model as a function of RCS azimuth and elevation angles.

TABLE II: Parameters for tactical and navigation grade IMU's.

IMU Grade	$3\sqrt{q_a}$ (m/s/$\sqrt{\text{hr}}$)	$3\sigma_{a,ss}$ (g)	$3\sqrt{q_g}$ (deg./$\sqrt{\text{hr}}$)	$3\sigma_{g,ss}$ (deg./hr.)
Industrial	0.1	0.001	0.2	10
Tactical	0.03	0.0001	0.05	1

grade (i.e. industrial, tactical) on the uncertainty in P_D and illustrate how this influences the path planner. The IMU grade parameters used in this section are provided in Table II.

A. Scenario 1

The first scenario shows a planned path for an aircraft equipped with a industrial-grade IMU. Fig. 7 shows a map with the planned and candidate paths of the path planner. The black polygons show the final state of the radar polygons used in the visibility graph planner. The initial candidate path shows that the shortest path is between the two radar units. As the aircraft travels through a GPS-Denied region, position and heading measurements are made unavailable to the INS. This causes the aircraft pose covariance to grow which contributes to an increase in σ_{pd}. The radar polygons are adjusted in areas where (73) is not satisfied according to the adjustment policy described in Section IV. The adjusted polygons overlap making the path between the radar units infeasible. The final planned path goes around the bottom of the lower radar unit but remains within the gray radar detection region.

Fig. 8 shows the P_D results for Scenario 1. This indicates that $\bar{P}_D + 3\sigma_{pd}$ stays below the P_D threshold of 0.1 as required by (73). Note that the areas of highest detection risk and largest σ_{pd} occur when the radar is detecting the side of the aircraft (i.e. $\alpha \approx 90$, 270 deg.). This is expected as these azimuth angles are associated with the largest RCS values and highest degree of variability (see Fig. 6). Also note that at its peak ($t \approx 4.2$ hr.), $3\sigma_{pd} \approx 0.018$ which is 34.4% of the nominal $\bar{P}_D$ at that time. These results indicate that there is substantial variability in P_D due to uncertainty in the aircraft pose, radar position, and radar parameters.

Fig. 9 shows an error budget for the sources of uncertainty at $t = 4.2$ hours using the methods presented in Section III. This time was chosen because it is when the aircraft is about to exit the GPS-Denied region and the aircraft pose uncertainty

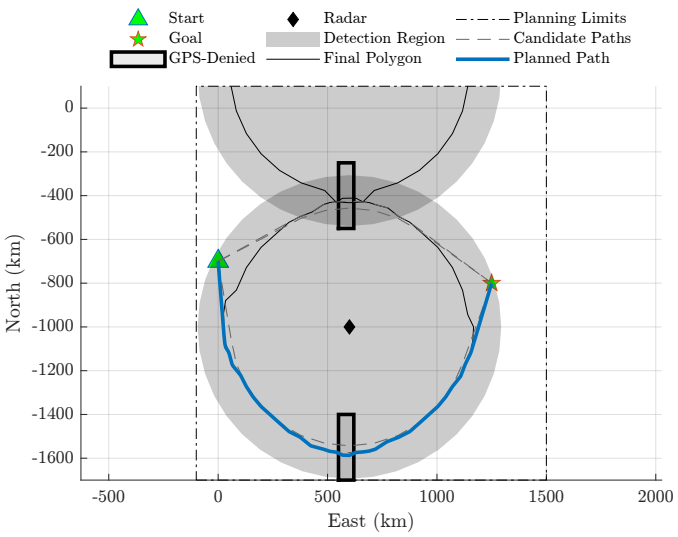

Fig. 7: Visibility graph path planner results for Scenario 1 with two radar systems (diamonds), radar polygons (black lines), GPS-Denied regions (black rectangles), candidate paths (dashed gray lines), and the final planned path (blue line).

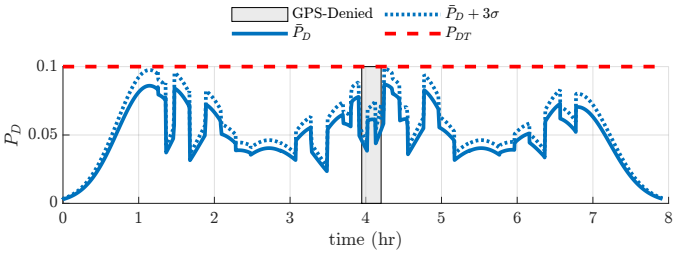

Fig. 8: P_D results for Scenario 1 with the P_D threshold $P_{DT} = 0.1$, nominal $\bar{P}_D$, and $\bar{P}_D + 3\sigma_{pd}$. The planner successfully finds a path through the radar detection region that maintains $\bar{P}_D + 3\sigma_{pd} < P_{DT}$.

is the largest. The error budget indicates that the uncertainty in the IMU is the primary driver of uncertainty in the variability of P_D. This indicates that to reduce the uncertainty in P_D the uncertainty in the IMU measurements must be reduced which will be examined in Scenario 2.

The LinCov analysis that is used to generate the error budget in Fig. 9 is expected to provide the same statistical information as a Monte Carlo analysis. Fig. 10 shows Monte Carlo results for a subset of the planned trajectory near the GPS-Denied region below the lower radar unit. The gray lines in Fig. 10 represent the P_D results for each of the 500 Monte Carlo runs. As expected, the gray lines mostly stay within the $3\sigma_{pd}$ lines and the plots show agreement between the LinCov 3σ and the Monte Carlo 3σ. Agreement between the Monte Carlo and LinCov results serve to validate the linear approximations made in the LinCov framework. There are minor deviations throughout the trajectory due to linearization errors (i.e. minor bias between $t = 4.15$-4.25 hrs.), but the deviations are negligible for the path planning scenario presented.

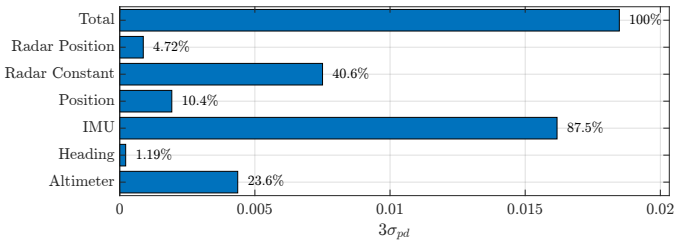

Fig. 9: Error budget results for Scenario 1 at $t = 4.2$ hours. This shows the $3\sigma_{pd}$ value at the stated time when each source of uncertainty is isolated. The Total line shows the $3\sigma_{pd}$ value of the LinCov model with all the sources of uncertainty activated. The percentages to the side of each bar indicate the percent of the Total uncertainty and the root-sum-square of the contributing $3\sigma_{pd}$ values equal the Total uncertainty.

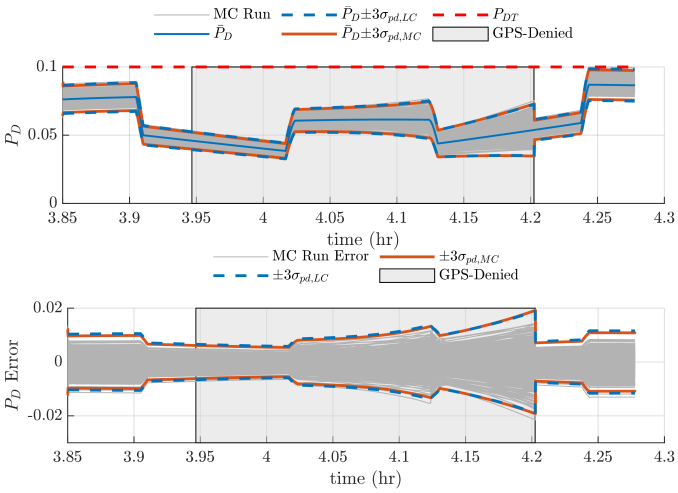

Fig. 10: P_D Monte Carlo results with 500 runs for the path segments around the first radar. The gray lines indicate P_D results for each Monte Carlo run with the P_D error results in the bottom figure. The P_D error is determined by subtracting the Monte Carlo run P_D from $\bar{P}_D$.

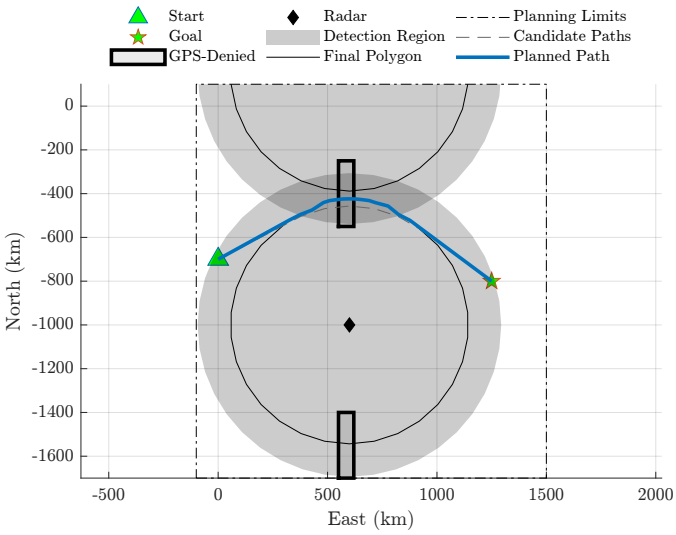

Fig. 11: Visibility graph path planner results for Scenario 2 with two radar systems (diamonds), radar polygons (black lines), GPS-Denied regions (thick black rectangles), candidate paths (dashed gray lines), and the final planned path (blue line).

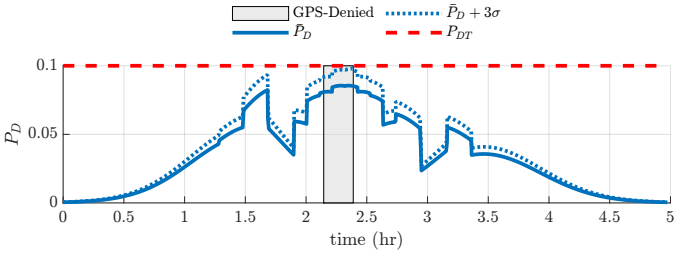

Fig. 12: P_D results for Scenario 2 with the P_D threshold $P_{DT} = 0.1$, nominal $\bar{P}_D$, and $\bar{P}_D + 3\sigma_{pd}$. The planner successfully finds a path through the radar detection region that maintains $\bar{P}_D + 3\sigma_{pd} < P_{DT}$. The effect of the GPS-Denied region is the increase in $3\sigma_{pd}$ near $t = 2.4$ hours.

B. Scenario 2

The second scenario uses the same radar and aircraft configuration as Scenario 1, except the industrial grade IMU is replaced by a tactical grade IMU (see Table II). Fig. 11 shows the 2D map for Scenario 2 where the final planned path goes between the radar units. In contrast to Scenario 1 with the industrial grade IMU, the tactical grade IMU makes the shorter path between the radar feasible by reducing the aircraft pose covariance.

Fig. 12 shows the P_D results for Scenario 2. The graph shows that the PDVG planner maintains $\bar{P}_D + 3\sigma_{pd}$ below the P_{DT} threshold of 0.1. Note that at its peak ($t \approx 2.38$ hr.), $3\sigma_{pd} \approx 0.013$ which is 15.2% of the nominal $\bar{P}_D$ at that time. This is a significant portion of the nominal P_D that must be considered for radar detection path planning in the presence of uncertainty, but is smaller than the variation calculated in Scenario 1.

The error budget for Scenario 2 at $t = 2.38$ hours, which is just before the aircraft exits the GPS-Denied region, is provided in Fig. 13. The graph indicates that the radar constant is the primary driver of uncertainty in P_D followed by the IMU. Contrast these results with the error budget in Scenario 1 (Fig. 9) to observe the reduction of the variability of P_D due to the IMU grade improvement.

C. Scenario 3

The third scenario illustrates the performance of the PDVG path planning algorithm in a radar detection region with several radar units. For this scenario, the radar constant and radar uncertainty were lowered ($c_r = 50$ and 20, $\sigma_{pr} = 100/3$, $\sigma_{cr} = 1/3$) to fit more radar units in the planning region used for Scenarios 1 and 2. Fig. 14 shows the 2D map of the results for Scenario 3. The dashed lines show the candidate paths considered by the PDVG path planner and the blue line shows the final planned path. Fig. 15 shows the P_D results for Scenario 3, which indicates the planner successfully

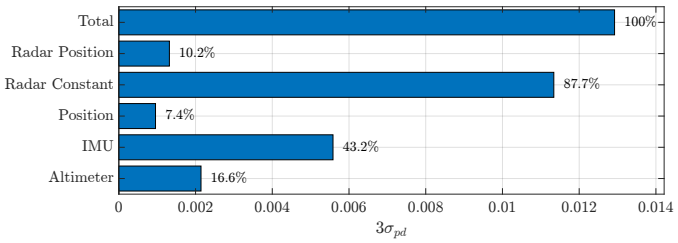

Fig. 13: Error budget results for Scenario 2 at $t = 2.38$ hours. The Total line shows the $3\sigma_{pd}$ value of the LinCov model with all the sources of uncertainty activated. The percentages to the side of each bar indicate the percent of the Total uncertainty for each of the sources of uncertainty and the root-sum-square of the contributing $3\sigma_{pd}$ values equal the Total uncertainty.

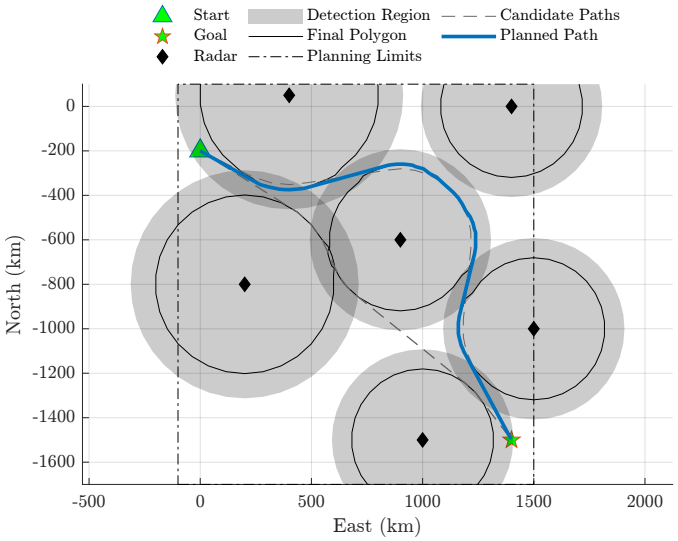

Fig. 14: Visibility graph path planner results for Scenario 3 with six radar systems (diamonds), radar polygons (black lines), GPS-Denied regions (thick black rectangles), a candidate path (dashed gray line), and a planned path (blue line).

finds a path through the radar detection region that maintains $\bar{P}_D + 3\sigma_{pd} < P_{DT}$. This scenario illustrates the utility of the PDVG path planner in complex detection environments that require expansions around several radar units.

The results in this section have illustrated the methods presented in this paper in four ways. First, the visibility graph path planner with the associated polygon adjustment policy is used to determine a feasible path that maintains $\bar{P}_D + 3\sigma_{pd} < P_{DT}$. Second, the INS is modeled to obtain aircraft state uncertainty due to errors in measurement sources and GPS-Denied regions. The resulting state covariance is used to inform the visibility graph path planner to find a path that maintains P_D below the mission-specified threshold. Third, the LinCov models are used to generate error budgets to compare sources of uncertainty. The error budget provided actionable information (i.e., improve IMU grade) which, when implemented, resulted in a shorter path between the radars that met the mission objectives. Fourth, the PDVG planner

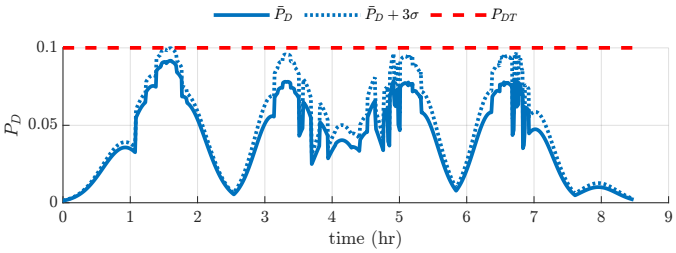

Fig. 15: P_D results for Scenario 3 with the P_D threshold $P_{DT} = 0.1$, nominal $\bar{P}_D$, and $\bar{P}_D + 3\sigma_{pd}$. The planner successfully finds a path through the radar detection region that maintains $\bar{P}_D + 3\sigma_{pd} < P_{DT}$.

described in this paper is applied to a congested detection region with several radar systems.

VI. Conclusion

Path planning for aircraft operating under threat of detection from ground-based radar systems must account for the probability of detection. Several factors influence the detection risk of the aircraft including the aircraft pose, radar position, and radar performance characteristics. In addition, uncertainty in each of these factors also influence the probability of detection. Current radar detection path planning methods fail to consider the uncertainty in these factors when estimating the detection risk of a trajectory. In practice, the uncertainty inherent in each of these factors is significant and influences the variability of the probability of detection. In the scenarios shown in this paper, the variability of P_D is a large fraction, up to 34.4%, of the nominal value.

This paper presents a method to propagate the covariance of the aircraft state and incorporate it with the uncertainty of the radar state into the radar detection model. The method uses an inertial navigation system to propagate the covariance using IMU measurements and update the covariance with position, heading, and altitude measurements. The nominal aircraft states and IMU measurements are generated using the ASG method from [23]. The radar detection model is linearized about a nominal operating point and the variance of P_D is calculated using the aircraft and radar state covariance matrices [14, 22].

These methods are used in the P_D Visibility Graph (PDVG) path planner, where the nominal P_D and standard deviation, σ_{pd}, are used to determine path validity and the polygon expansion policy. This paper shows that the PDVG planner successfully plans paths that maintain $P_D + 3\sigma_{pd}$ below a threshold for three scenarios. The error budgets generated by the path planner indicate that when the aircraft travels through GPS-Denied regions, measurement uncertainties in the IMU become the primary driver of the variance of P_D. This variance is reduced by improving the IMU grade used in the aircraft model.

The results show that an advantage of using the methods presented in this paper is that the user can evaluate the sources of uncertainty and make actionable decisions. For example, the IMU uncertainties were the primary driver of the variance

of P_D in Scenario 1, but when the IMU grade was improved, σ_{pd} was reduced by 27.8%. The improved IMU grade allowed the aircraft to travel between two radars which was infeasible with the original IMU grade. The results in this paper show that uncertainty in the aircraft and radar states significantly impact the variability of P_D and must be considered for path planning. To address this, the PDVG planner is presented as a framework for incorporating the variability of P_D in planning a path that maintains the probability of detection below a mission-specified threshold.

REFERENCES

[1] N. Ceccarelli, J. J. Enright, E. Frazzoli, S. J. Rasmussen, and C. J. Schumacher, "Micro uav path planning for reconnaissance in wind," in *2007 American Control Conference*, 2007, pp. 5310–5315.

[2] R. Larson, M. Pachter, and M. Mears, "Path Planning by Unmanned Air Vehicles for Engaging an Integrated Radar Network," in *AIAA Guidance, Navigation, and Control Conference and Exhibit*. American Institute of Aeronautics and Astronautics, 2001.

[3] F. Xiao-wei, L. Zhong, and G. Xiao-guang, "Path Planning for UAV in Radar Network Area," in *2010 Second WRI Global Congress on Intelligent Systems*, vol. 3, Dec. 2010, pp. 260–263.

[4] P. T. Kabamba, S. M. Meerkov, and F. H. Z. III, "Optimal Path Planning for Unmanned Combat Aerial Vehicles to Defeat Radar Tracking," *Journal of Guidance, Control, and Dynamics*, May 2012.

[5] J. Marcum, "A statistical theory of target detection by pulsed radar," *IRE Transactions on Information Theory*, vol. 6, no. 2, pp. 59–267, Apr. 1960.

[6] P. Swerling, "Probability of Detection for Fluctuating Targets," RAND Corporation, Tech. Rep., Jan. 1954.

[7] B. R. Mahafza and A. Elsherbeni, *MATLAB Simulations for Radar Systems Design*. CRC Press, Dec. 2003.

[8] M. McFarland, R. Zachery, and B. Taylor, "Motion planning for reduced observability of autonomous aerial vehicles," in *Proceedings of the 1999 IEEE International Conference on Control Applications (Cat. No.99CH36328)*, vol. 1, Aug. 1999, pp. 231–235 vol. 1.

[9] S. Bortoff, "Path planning for UAVs," in *Proceedings of the 2000 American Control Conference. ACC (IEEE Cat. No.00CH36334)*, vol. 1, Jun. 2000, pp. 364–368 vol.1, iSSN: 0743-1619.

[10] P. Chandler, S. Rasmussen, and M. Pachter, "UAV cooperative path planning," in *AIAA Guidance, Navigation, and Control Conference and Exhibit*. Dever,CO,U.S.A.: American Institute of Aeronautics and Astronautics, Aug. 2000.

[11] M. Pachter and J. Hebert, "Optimal aircraft trajectories for radar exposure minimization," in *Proceedings of the 2001 American Control Conference. (Cat. No.01CH37148)*, vol. 3, Jun. 2001, pp. 2365–2369 vol.3, iSSN: 0743-1619.

[12] F. Moore, "Radar cross-section reduction via route planning and intelligent control," *IEEE Transactions on Control Systems Technology*, vol. 10, no. 5, pp. 696–700, Sep. 2002.

[13] M. Jun and R. D'Andrea, "Path Planning for Unmanned Aerial Vehicles in Uncertain and Adversarial Environments," in *Cooperative Control: Models, Applications and Algorithms*, ser. Cooperative Systems, S. Butenko, R. Murphey, and P. M. Pardalos, Eds. Boston, MA: Springer US, 2003, pp. 95–110.

[14] A. Costley, R. Christensen, G. Droge, and R. C. Leishman, "Sensitivity of single-pulse radar detection to aircraft pose uncertainties," 2022.

[15] P. G. Savage, *Strapdown analytics*. Maple Plain, Minn.: Strapdown Associates, 2000.

[16] M. S. Grewal, A. P. Andrews, and C. G. Bartone, *Global Navigation Satellite Systems, Inertial Navigation, and Integration*. John Wiley & Sons, Jan. 2020.

[17] J. Farrell, *Aided Navigation: GPS with High Rate Sensors*, 1st ed. USA: McGraw-Hill, Inc., 2008.

[18] P. S. Maybeck, *Stochastic Models, Estimation, and Control*. New York: Navtech Book and Software Store, 1994, vol. 1.

[19] R. G. Brown and P. Y. C. Hwang, *Introduction to random signals and applied Kalman filtering : with MATLAB exercises and solutions*, 1997.

[20] R. S. Christensen and D. Geller, "Linear covariance techniques for closed-loop guidance navigation and control system design and analysis," *Proceedings of the Institution of Mechanical Engineers, Part G: Journal of Aerospace Engineering*, vol. 228, no. 1, pp. 44–65, 2014. [Online]. Available: https://doi.org/10.1177/0954410012467717

[21] R. S. Christensen, G. Droge, and R. C. Leishman, "Closed-Loop Linear Covariance Framework for Path Planning in Static Uncertain Obstacle Fields," *Journal of Guidance, Control, and Dynamics*, vol. 45, no. 4, pp. 669–683, 2022, publisher: American Institute of Aeronautics and Astronautics _eprint: https://doi.org/10.2514/1.G006228. [Online]. Available: https://doi.org/10.2514/1.G006228

[22] A. Costley, R. Christensen, R. C. Leishman, and G. Droge, "Sensitivity of single-pulse radar detection to radar state uncertainty," 2022. [Online]. Available: https://arxiv.org/abs/2203.11372

[23] A. Costley, R. S. Christensen, R. Leishman, and G. Droge, "Analytical aircraft state and imu signal generator from smoothed reference trajectory," *IEEE Transactions on Aerospace and Electronic Systems*, pp. 1–1, 2021.

[24] D. North, "An Analysis of the factors which determine signal/noise discrimination in pulsed-carrier systems," *Proceedings of the IEEE*, vol. 51, no. 7, pp. 1016–1027, Jul. 1963.

[25] Beard, Randy and McLain, Timothy, *Small Unmanned Aircraft Theory and Practice*, 2012.

[26] R. Zanetti, "Rotations, Transformations, Left Quaternions, Right Quaternions?" *The Journal of the Astronautical Sciences*, vol. 66, no. 3, pp. 361–381, Sep. 2019.

[27] J. R. Carpenter and C. N. D'Souza, "Navigation Filter Best Practices," National Aeronautics and Space Administration, NASA Technical Report, Apr. 2018.

[28] W. Lear, "Kalman Filtering Techniques," NASA Johnson Space Center, NASA Technical Report JSC-20688, Sep. 1985.

[29] A. Scheuer and T. Fraichard, "Continuous-curvature path planning for car-like vehicles," in *Proceedings of the 1997 IEEE/RSJ International Conference on Intelligent Robot and Systems. Innovative Robotics for Real-World Applications. IROS 97*, vol. 2, Sep. 1997, pp. 997–1003 vol.2.

[30] E. Dijkstra, "A Note on Two Problems in Connexion with Graphs," *Numerische mathematik*, vol. 1, no. 1, pp. 269–271, 1959.

[31] P. E. Hart, N. J. Nilsson, and B. Raphael, "A formal basis for the heuristic determination of minimum cost paths," *IEEE Transactions on Systems Science and Cybernetics*, vol. 4, no. 2, pp. 100–107, 1968.

[32] J.-L. Blanco, "A tutorial on se (3) transformation parameterizations and on-manifold optimization," *University of Malaga, Tech. Rep*, vol. 3, p. 6, 2010.

APPENDIX A
QUATERNION TO EULER ANGLE LINEARIZATION

This appendix derives the linearization of the quaternion to Euler angle attitude representations with a small angle assumption. The linearized model is used to define the matrix M_a which transforms the aircraft state of the INS model $\hat{\boldsymbol{x}}$ defined in (12) to the aircraft state of the radar model $\boldsymbol{x_a}$ given by $\boldsymbol{x_a} = \begin{bmatrix}\boldsymbol{p_a^n} & \boldsymbol{\Theta_a}\end{bmatrix}^\intercal$.

The general quaternion to Euler transformation [32] is given by

$$\begin{bmatrix}\phi\\ \theta\\ \psi\end{bmatrix} = \begin{bmatrix}\arctan\frac{2(q_0q_1+q_2q_3)}{1-2\left(q_1^2+q_2^2\right)}\\ \arcsin 2(q_0q_2-q_3q_1)\\ \arctan\frac{2(q_0q_3+q_1q_2)}{1-2\left(q_2^2+q_3^2\right)}\end{bmatrix} \tag{75}$$

The first element of the error quaterion defined in (24) is 1 so let $q_0 = 1$ then

$$\begin{bmatrix}\phi\\ \theta\\ \psi\end{bmatrix} = \begin{bmatrix}\arctan\frac{2(q_1+q_2q_3)}{1-2\left(q_1^2+q_2^2\right)}\\ \arcsin 2(q_2-q_3q_1)\\ \arctan\frac{2(q_3+q_1q_2)}{1-2\left(q_2^2+q_3^2\right)}\end{bmatrix} \tag{76}$$

The Jacobian of (76) with respect to $\boldsymbol{q}_{1:3}$ is $\frac{\partial\boldsymbol{\Theta}}{\partial\boldsymbol{q}_{1:3}}$. The elements of $\frac{\partial\boldsymbol{\Theta}}{\partial\boldsymbol{q}_{1:3}}$ are given by

$$\frac{\partial\phi}{\partial q_1} = -\frac{\frac{2}{q_a}-\frac{q_1(2q_1+2q_2q_3)4}{q_a^2}q_a^2}{q_a^2+(2q_1+2q_2q_3)} \tag{77}$$

$$\frac{\partial \phi}{\partial q_2} = -\frac{\frac{2q_3}{q_a} - \frac{q_2(2q_1+2q_2q_3)4}{q_a^2}q_a^2}{q_a^2 + (2q_1 + 2q_2q_3)} \tag{78}$$

$$\frac{\partial \phi}{\partial q_3} = -\frac{2q_1^2 + 2q_2^2 - 1}{(2q_1^2 + 2q_2^2 - 1)^2 + (2q_1 + 2q_2q_3)^2} \tag{79}$$

$$\frac{\partial \theta}{\partial q_1} = -\frac{2q_3}{\sqrt{1-(2q_2 - 2q_1q_3)^2}} \tag{80}$$

$$\frac{\partial \theta}{\partial q_2} = \frac{2}{\sqrt{1-(2q_2 - 2q_1q_3)^2}} \tag{81}$$

$$\frac{\partial \theta}{\partial q_3} = -\frac{2q_1}{\sqrt{1-(2q_2 - 2q_1q_3)^2}} \tag{82}$$

$$\frac{\partial \psi}{\partial q_1} = -\frac{2q_2q_b}{q_b^2 + (2q_3 + 2q_1q_2)^2} \tag{83}$$

$$\frac{\partial \psi}{\partial q_2} = -\frac{\frac{2q_1}{q_b} - \frac{q_2(2q_3+2q_1q_2)4}{q_b^2}q_b^2}{q_b^2 + (2q_3 + 2q_1q_2)^2} \tag{84}$$

$$\frac{\partial \psi}{\partial q_3} = -\frac{\frac{2}{q_b} - \frac{q_3(2q_3+2q_1q_2)4}{q_b}q_b^2}{q_b^2 + (2q_3 + 2q_1q_2)} \tag{85}$$

where

$$q_a = 2q_1^2 + 2q_2^2 - 1 \tag{86}$$

$$q_b = 2q_2^2 + 2q_3^2 - 1. \tag{87}$$

Evaluating the partial derivatives at the nominal $q_1 = q_2 = q_3 = 0$ yields the final Jacobian of the quaternion to Euler angle transformation as

$$\left.\frac{\partial \boldsymbol{\Theta}}{\partial \boldsymbol{q}_{1:3}}\right|_{\boldsymbol{\delta\bar{q}}} = 2\boldsymbol{I}_{3\times 3}. \tag{88}$$

The quaterion to Euler angle Jacobian defined in (88) is used to transform the INS model state $\hat{\boldsymbol{x}}$ as defined in (12) to the aircraft state in the radar model $\boldsymbol{x_a}$ as

$$\boldsymbol{x_a} = \begin{bmatrix} I_{3\times3} & 0_{3\times3} & 0_{3\times3} & 0_{3\times3} & 0_{3\times3} \\ 0_{3\times3} & 0_{3\times3} & 2I_{3\times3} & 0_{3\times3} & 0_{3\times3} \end{bmatrix} \boldsymbol{x} \tag{89}$$

$$= M_a \boldsymbol{x}. \tag{90}$$

Appendix B
Covariance Propagation using Lear's Method

While the error state model in (26) is an accurate representation of the error dynamics, the error states are more efficiently propagated using the state transition matrix (STM). This is represented in discrete time as

$$\delta \boldsymbol{x}_k = \Phi\left(t_k, t_{k-1}\right) \delta \boldsymbol{x}_{k-1} + \boldsymbol{w}_{k-1} \tag{91}$$

where $\Phi\left(t_k, t_{k-1}\right)$ is the STM from the t_{k-1} to t_k , and $\boldsymbol{w}_{k-1}$ is the integrated process noise over the same time interval given by

$$\boldsymbol{w}_{k-1} = \int_{t_{k-1}}^{t_k} \Phi\left(t_k, \tau\right) BQ\left(\tau\right) \boldsymbol{w}\left(\tau\right) d\tau. \tag{92}$$

The covariance of the estimation errors is also propagated using the STM using

$$P_k^- = \Phi\left(t_k, t_{k-1}\right) P_{k-1}^- \Phi^T\left(t_k, t_{k-1}\right) + Q_{k-1} \tag{93}$$

where Q_{k-1} is the covariance of the integrated process noise defined by

$$Q_{k-1} = E\left[\boldsymbol{w}_{k-1}\boldsymbol{w}_{k-1}^T\right] = \int_{t_{k-1}}^{t_k} \Phi\left(t_k, \tau\right) B\left(\tau\right) Q\left(\tau\right) B^T\left(\tau\right) \Phi^T\left(t_k, \tau\right) d\tau. \tag{94}$$

The following paragraphs provide a derivation for $\Phi\left(t_k, t_{k-1}\right)$ and Q_{k-1}. The STM is defined as the matrix which satisfies the differential equation [18]

$$\dot{\Phi}\left(t_{k+1}, t_k\right) = F\left(t\right) \Phi\left(t_{k+1}, t_k\right) \tag{95}$$

where $\Phi\left(t_k, t_k\right) = I_{n\times n}$. While it is possible to numerically integrate (95), approximation of the integral over small time frames is sufficient for many practical filters and is much more efficient. There are many good approximations for this purpose [27], however Lear's method is chosen for this application [28]. Lear's method for approximating the state transition matrix is given by

$$\Phi\left(t_{k+1}, t_k\right) \approx I + \frac{\Delta t}{2}\left(F_k + F_{k-1}\right) + \frac{\Delta t^2}{2} F_k F_{k-1} \tag{96}$$

where $F_k = F\left(t_k\right)$ and $\Delta t = t_k - t_{k-1}$. To aid in the derivation that follows, the error states defined in (25) are partitioned into vehicle states and parameter states as

$$\delta \boldsymbol{x} = \begin{bmatrix} \delta \boldsymbol{x}_v & \delta \boldsymbol{x}_p \end{bmatrix}^T \tag{97}$$

where the vehicle states comprise the position, velocity, and attitude errors

$$\delta \boldsymbol{x}_v = \begin{bmatrix} \delta \boldsymbol{p}^n & \delta \boldsymbol{v}^n & \delta \boldsymbol{\theta}_b^n \end{bmatrix}^T \tag{98}$$

and the parameter states include the accelerometer and gyro biases.

$$\delta \boldsymbol{x}_p = \begin{bmatrix} \delta \boldsymbol{b}_a^b & \delta \boldsymbol{b}_g^b \end{bmatrix}^T \tag{99}$$

The state coupling matrix F_k has the same form as (53) and is partitioned as

$$F_k = \begin{bmatrix} F_{vv} & F_{vp} \\ 0_{6\times9} & F_{pp} \end{bmatrix} \tag{100}$$

and the STM is partitioned as

$$\Phi\left(t_{k+1}, t_k\right) = \Phi_k = \begin{bmatrix} \Phi_{vv} & \Phi_{vp} \\ \Phi_{pv} & \Phi_{pp} \end{bmatrix}. \tag{101}$$

Since the parameter states are modeled as FOGM processes, independent of the vehicle states, the corresponding elements of the STM are known analytically as

$$\Phi_{pv} = 0_{6\times9} \tag{102}$$

and

$$\Phi_{pp} = \begin{bmatrix} \exp\left(-\Delta t/\tau_a\right) I_{3\times3} & 0_{3\times3} \\ 0_{3\times3} & \exp\left(-\Delta t/\tau_g\right) I_{3\times3} \end{bmatrix} \tag{103}$$

The upper-left element of the STM from (101) is approximated using (96) to yield

$$\Phi_{vv} \approx \begin{bmatrix} I_{3\times3} & \Delta t I_{3\times3} & \frac{\Delta t^2}{2}\left[\hat{\boldsymbol{\nu}}_{k-1}^n\right]\times \\ 0_{3\times3} & I_{3\times3} & \frac{\Delta t}{2}\left[\hat{\boldsymbol{\nu}}_{\Sigma}^n\right]\times \\ 0_{3\times3} & 0_{3\times3} & I_{3\times3} \end{bmatrix} \tag{104}$$

where

$$\hat{\boldsymbol{\nu}}_{k-1}^{n} = \hat{T}_{b,k-1}^{n}\left(\tilde{\boldsymbol{\nu}}_{k-1}^{b} - \hat{\boldsymbol{b}}_{a,k-1}^{b}\right) \quad (105)$$

$$\hat{\boldsymbol{\nu}}_{k}^{n} = \hat{T}_{b,k-1}^{n}\left(\tilde{\boldsymbol{\nu}}_{k}^{b} - \hat{\boldsymbol{b}}_{a,k}^{b}\right) \quad (106)$$

and

$$\hat{\boldsymbol{\nu}}_{\Sigma}^{n} = \hat{\boldsymbol{\nu}}_{k}^{n} + \hat{\boldsymbol{\nu}}_{k-1}^{n}. \quad (107)$$

The lower-left element of the STM from (101) is approximated using (96) to yield

$$\Phi_{vp} \approx \begin{bmatrix} -\frac{\Delta t^2}{2}\hat{T}_{b,k-1}^{n} & 0_{3\times3} \\ -\frac{\Delta t}{2}\hat{T}_{b,\Sigma}^{n} + \frac{\Delta t^2}{2\tau_a}\hat{T}_{b,k}^{n} & \frac{\Delta t^2}{2}\left\{[\hat{\boldsymbol{\nu}}_{k}^{n}]\times\right\}\hat{T}_{b,k-1}^{n} \\ 0_{3\times3} & \frac{\Delta t}{2}\hat{T}_{b,\Sigma}^{n} - \frac{\Delta t^2}{2\tau_g}\hat{T}_{b,k}^{n} \end{bmatrix} \quad (108)$$

where

$$\hat{T}_{b,\Sigma}^{n} = \hat{T}_{b,k}^{n} + \hat{T}_{b,k-1}^{n}. \quad (109)$$

The integrated process noise Q_{k-1} in (94) is derived in the following paragraphs. Begin by partitioning the dynamics coupling matrix and noise density matrix

$$B = \begin{bmatrix} B_{v,n} & 0_{9\times6} \\ 0_{6\times6} & I_{6\times6} \end{bmatrix} \quad (110)$$

$$Q = \begin{bmatrix} Q_{n} & 0_{6\times6} \\ 0_{6\times6} & Q_{w} \end{bmatrix} \quad (111)$$

where

$$B_{v,n} = \begin{bmatrix} 0_{3\times3} & 0_{3\times3} \\ -\hat{T}_{b}^{n} & 0_{3\times3} \\ 0_{3\times3} & \hat{T}_{b}^{n} \end{bmatrix} \quad (112)$$

$$Q_{n} = \begin{bmatrix} Q_{\nu} & 0_{3\times3} \\ 0_{3\times3} & Q_{\omega} \end{bmatrix} \quad (113)$$

$$Q_{w} = \begin{bmatrix} q_a I_{3\times3} & 0_{3\times3} \\ 0_{3\times3} & q_g I_{3\times3} \end{bmatrix} \quad (114)$$

The integral of (94) can be expressed as

$$Q_{k-1} = \begin{bmatrix} Q_{vv} & Q_{vp} \\ Q_{pv} & Q_{pp} \end{bmatrix} \quad (115)$$

where

$$Q_{vv} = \int_{t_{k-1}}^{t_k} \Phi_{vv}\left(t_k,\tau\right) B_{v,n}\left(\tau\right) Q_n B_{v,n}^{T}\left(\tau\right) \Phi_{vv}^{T}\left(t_k,\tau\right) + \Phi_{vp}\left(t_k,\tau\right) Q_w \Phi_{vp}^{T}\left(t_k,\tau\right) d\tau \quad (116)$$

$$Q_{vp} = Q_{pv}^{T} = \int_{t_{k-1}}^{t_k} \Phi_{vp}\left(t_k,\tau\right) Q_w \Phi_{pp}^{T}\left(t_k,\tau\right) d\tau \quad (117)$$

and

$$Q_{pp} = \int_{t_{k-1}}^{t_k} \Phi_{pp}\left(t_k,\tau\right) Q_w \Phi_{pp}^{T}\left(t_k,\tau\right) d\tau \quad (118)$$

The integrals in (116)-(118) are derived separately in the following paragraphs. The integrated process noise for the parameter states is approximated as

$$Q_{pp} \approx \begin{bmatrix} q_a\frac{\tau_a}{2}e_a I_{3\times3} & 0_{3\times3} \\ 0_{3\times3} & q_g\frac{\tau_g}{2}e_g I_{3\times3} \end{bmatrix}. \quad (119)$$

where

$$e_a = 1 - \exp(\frac{-2\Delta t}{\tau_a}) \quad (120)$$

$$e_g = 1 - \exp(\frac{-2\Delta t}{\tau_g}). \quad (121)$$

The integrated process noise of the coupled parameter and vehicle states can be derived as

$$Q_{vp} = \begin{bmatrix} -q_a\hat{T}_{b,k-1}^{n}c_a & 0_{3\times3} \\ -q_a\hat{T}_{b,\Sigma}^{n}c_t + q_a\hat{T}_{b,k}^{n}\frac{c_a}{\tau_a} & q_g\left\{[\hat{\boldsymbol{\nu}}_{k}^{n}]\times\right\}\hat{T}_{b,k-1}^{n}c_a \\ 0_{3\times3} & q_g\hat{T}_{b,\Sigma}^{n}c_t - q_g\hat{T}_{b,k}^{n}c_a \end{bmatrix} \quad (122)$$

where

$$c_a = \tau_a^3 - \frac{1}{2}\tau_a\left(2\tau_a^2 + 2\tau_a\Delta t + \Delta t^2\right)\exp(\frac{\Delta t}{\tau_a}) \quad (123)$$

$$c_t = \frac{\tau_a^2}{2} - \frac{\tau_a}{2}(\tau_a + \Delta t)\exp(\frac{-\Delta t}{\tau_a}) \quad (124)$$

The integrated process noise of the vehicle states is partitioned as

$$Q_{vv} = \begin{bmatrix} Q_{vv,11} & Q_{vv,12} & Q_{vv,13} \\ Q_{vv,21} & Q_{vv,22} & Q_{vv,23} \\ Q_{vv,31} & Q_{vv,32} & Q_{vv,33} \end{bmatrix} \quad (125)$$

where the equations for each entry are given by

$$Q_{vv,11} = \frac{\Delta t^3}{3}\mathcal{Q}_{\nu,k} + \frac{\Delta t^5}{20}\left(\mathcal{Q}_{b,k-1}^{n} + q_a\hat{T}_{b,k-1}^{n}\left(\hat{T}_{b,k-1}^{n}\right)^{T}\right) \quad (126)$$

$$Q_{vv,12} = \frac{\Delta t^2}{2}\mathcal{Q}_{\nu,k} + \frac{\Delta t^4}{16}\left(\left\{\left[\hat{\boldsymbol{\nu}}_{k-1}^{n}\right]\times\right\}\mathcal{Q}_{\omega,k}\left\{[\hat{\boldsymbol{\nu}}_{\Sigma}^{n}]\times\right\}^{T} + q_a\hat{T}_{b,k-1}^{n}\hat{T}_{b,\Sigma}^{n\,T}\right) - q_a\frac{\Delta t^5}{20\tau_a}\hat{T}_{b,k-1}^{n}\left(\hat{T}_{b,k}^{n}\right)^{T} \quad (127)$$

$$Q_{vv,13} = \frac{1}{6}\Delta t^3\left\{\left[\hat{\boldsymbol{\nu}}_{k-1}^{n}\right]\times\right\}\mathcal{Q}_{\nu,k} \quad (128)$$

$$Q_{vv,21} = \frac{\Delta t^2}{2}\mathcal{Q}_{\nu,k} + \frac{\Delta t^4}{16}\left(\left\{[\hat{\boldsymbol{\nu}}_{\Sigma}^{n}]\times\right\}\mathcal{Q}_{\omega,k}\left\{\left[\hat{\boldsymbol{\nu}}_{k-1}^{n}\right]\times\right\}^{T} + q_a\hat{T}_{b,\Sigma}^{n}\left(\hat{T}_{b,k-1}^{n}\right)^{T}\right) - q_a\frac{\Delta t^5}{20\tau_a}\hat{T}_{b,k-1}^{n}\left(\hat{T}_{b,k}^{n}\right)^{T} \quad (129)$$

$$Q_{vv,22} = \Delta t\mathcal{Q}_{\nu,k} + \frac{\Delta t^3}{12}\left(\left\{[\hat{\boldsymbol{\nu}}_{\Sigma}^{n}]\times\right\}\mathcal{Q}_{\omega,k}\left\{[\hat{\boldsymbol{\nu}}_{\Sigma}^{n}]\times\right\}^{T} + q_a\hat{T}_{b,\Sigma}^{n}\left(\hat{T}_{b,\Sigma}^{n}\right)^{T}\right)$$

$$
\begin{aligned}
&- q_a \frac{\Delta t^4}{16\tau_a} \hat{T}^n_{b,k} \left[\hat{T}^n_{b,k} \left(\hat{T}^n_{b,\Sigma} \right)^T + \hat{T}^n_{b,\Sigma} \left(\hat{T}^n_{b,k} \right)^T \right] \\
&+ \frac{\Delta t^5}{20} \left(\frac{q_a}{\tau_a^2} \hat{R}^n_{b,k} \left(\hat{R}^n_{b,k} \right)^T \right. \\
&\left. + q_g \left\{ [\hat{\boldsymbol{\nu}}^n_k] \times \right\} \hat{T}^n_{b,k-1} \left(\hat{T}^n_{b,k-1} \right)^T \left\{ [\hat{\boldsymbol{\nu}}^n_k] \times \right\}^T \right)
\end{aligned} \tag{130}
$$

$$
\begin{aligned}
Q_{vv,23} = &\frac{\Delta t^2}{4} \left\{ [\hat{\boldsymbol{\nu}}^n_\Sigma] \times \right\} \mathcal{Q}_{\omega,k} \\
&+ q_g \frac{\Delta t^4}{16} \left\{ [\hat{\boldsymbol{\nu}}^n_k] \times \right\} \hat{T}^n_{b,k-1} \left(\hat{T}^n_{b,\Sigma} \right)^T \\
&- q_g \frac{\Delta t^5}{20\tau_g} \left\{ [\hat{\boldsymbol{\nu}}^n_k] \times \right\} \hat{T}^n_{b,k-1} \left(\hat{T}^n_{b,k} \right)^T
\end{aligned} \tag{131}
$$

$$
Q_{vv,31} = \frac{\Delta t^3}{6} \mathcal{Q}_{\omega,k} \left\{ \left[\hat{\boldsymbol{\nu}}^n_{k-1} \right] \times \right\}^T \tag{132}
$$

$$
\begin{aligned}
Q_{vv,32} = &\frac{\Delta t^2}{4} \mathcal{Q}_{\omega,k} \left\{ [\hat{\boldsymbol{\nu}}^n_\Sigma] \times \right\}^T \\
&+ q_g \frac{\Delta t^4}{16} \hat{T}^n_{b,\Sigma} \left(\left\{ [\hat{\boldsymbol{\nu}}^n_k] \times \right\} \hat{T}^n_{b,k-1} \right)^T \\
&- q_g \frac{\Delta t^5}{20\tau_g} \hat{T}^n_{b,k} \left(\left\{ [\hat{\boldsymbol{\nu}}^n_k] \times \right\} \hat{T}^n_{b,k-1} \right)^T
\end{aligned} \tag{133}
$$

$$
\begin{aligned}
Q_{vv,33} = &\Delta t \mathcal{Q}_{\omega,k} + q_g \frac{\Delta t^3}{12} \hat{T}^n_{b,\Sigma} \left(\hat{T}^n_{b,\Sigma} \right)^T \\
&- q_g \frac{\Delta t^4}{16\tau_g} \left[\hat{T}^n_{b,k} \left(\hat{T}^n_{b,\Sigma} \right)^T + \hat{T}^n_{b,\Sigma} \left(\hat{T}^n_{b,k} \right)^T \right] \\
&+ q_g \frac{\Delta t^5}{20\tau_g^2} \hat{T}^n_{b,k} \left(\hat{T}^n_{b,k} \right)^T
\end{aligned} \tag{134}
$$

and

$$
\mathcal{Q}^n_{b,k-1} = \left\{ \left[\hat{\boldsymbol{\nu}}^n_{k-1} \right] \times \right\} \hat{T}^n_{b,k} Q_\omega \left(\hat{T}^n_{b,k} \right)^T \left\{ \left[\hat{\boldsymbol{\nu}}^n_{k-1} \right] \times \right\}^T \tag{135}
$$

$$
\mathcal{Q}_{\nu,k} = \hat{T}^n_{b,k} Q_\nu \left(\hat{T}^n_{b,k} \right)^T \tag{136}
$$

$$
\mathcal{Q}_{\omega,k} = \hat{T}^n_{b,k} Q_\omega \left(\hat{T}^n_{b,k} \right)^T \tag{137}
$$

$$
\hat{R}^n_{b,\Sigma} = \hat{T}^n_{b,k-1} + \hat{T}^n_{b,k}. \tag{138}
$$

CHAPTER 6

CONCLUSION

Mission planners for aircraft operating under threat of detection by ground-based radar systems plan paths to avoid detection. Several factors influence the probability of detection, including the aircraft pose, radar cross-section, radar position, and radar parameters. In practice, these factors have inherent uncertainty that is neglected by prior path planning methods. This dissertation describes research to incorporate uncertainty in these factors into a path planner. The development includes a framework to calculate detection risk with uncertainty, a novel aircraft state and IMU measurement generator to enable rapid path evaluation, and a path planner that uses the detection risk uncertainty and provides actionable information to the mission planner.

The radar detection model used in this work provides an expression for the detection risk, P_D, as a nonlinear function of the detection factors. The framework developed in Chapter 2 linearizes the equation for P_D with respect to the aircraft pose. The linearized model is used to approximate, to the first order, the uncertainty induced by the aircraft pose covariance. The results in Chapter 2 validate the linearization of P_D and examine the sensitivity of P_D to aircraft pose uncertainty. It is shown that the $3\sigma_{pd}$ values predicted by the linearized model exceed 0.1 for moderate aircraft pose uncertainty with the simple spikeball RCS model.

The radar detection framework is extended to include uncertainties in the radar state in Chapter 3. In this development, the equation for P_D is linearized with respect to the radar position and radar constant. The results in Chapter 3 validate the linearization for three levels of radar state uncertainty and shows that the $3\sigma_{pd}$ values estimated by the linearized model approach 0.1 for moderate radar state uncertainty. Furthermore, an error budget is generated that compares the contribution of moderate aircraft and radar state uncertainties to the variability in P_D. The error budget shows that the radar state

uncertainties contribute more to the variability in P_D than aircraft state uncertainty.

The radar detection framework presented in Chapters 2 and 3 relies on the calculation of the aircraft pose covariance matrix. The framework does not dictate the source of the aircraft pose covariance, but the approach taken in this dissertation is to use the pose covariance estimated by an aided inertial navigation system. The pose covariance propagation of such a system relies on noisy and biased measurements from an IMU. Previous methods for generating IMU measurements relied on differentiating aircraft pose samples to generate an aircraft trajectory with associated specific force and angular rate measurements. This approach is computationally intensive due, in part, to the small time steps required to get accurate IMU measurements. This limitation is addressed in Chapter 4, where a novel aircraft state and IMU measurement generator, ASG, is developed that provides analytical expressions for the quantities on interest.

The ASG method is a multi-stage component that provides analytical expressions for the aircraft pose, specific force, and angular rates along a path. The first stage converts a series of waypoints to continuous-curvature path segments with analytical expressions for position, curvature, and course angle. The second stage assumes the aircraft is operating at a trimmed pitch value and applies a coordinated turn assumption to calculate the roll and pitch angle, roll and pitch angle rates, and course angle rate along each segment. The third stage uses curvilinear motion theory to obtain an expression for the acceleration vector along path that is used to generate nominal specific force measurements. The final stage converts the roll, pitch, and yaw angle rates to the body frame angular rates experienced by an aircraft flying along the smoothed path. The results in Chapter 4 compare the accuracy of the IMU measurements from the analytical expressions with those generated from an integration method for various time-steps. The results show that the analytical method is consistent with the integration method for small time steps (i.e., $dt = 0.001s$) and as the time step is increased, the error in the analytical method grows much slower than the integration method.

The ASG method and radar detection framework enable rapid path planning for aircraft operating under threat of detection from ground-based radar systems with uncertainty in the aircraft and radar states. Chapter 5 extends a visibility graph path planner with the methods developed in this dissertation to efficiently propagate the covariance of an aided inertial navigation system and consider the variability in P_D as part of the path evaluation. The path planner uses a linear covariance model to obtain the necessary statistical information to generate error budgets for the uncertainty sources present in the aircraft and radar models. The error budgets provide a graphical comparison of how each uncertainty source contributes to the variability in P_D.

The results in Chapter 5 illustrate the performance of the path planner and the advantages of generating error budgets for the sources of uncertainty. The path planner successfully maintains the detection risk below a mission specified threshold for multiple planning scenarios. In the first scenario, the planner determines a path around the two radar systems because the planner is unable to find a valid path between them. The error budget indicates that the uncertainty in the IMU measurement is the primary driver of variability in P_D. In the second scenario, a higher-grade IMU is used and the planner successfully finds a path between the radar systems. This example illustrates the advantage of incorporating uncertainties in the path planning scenario and generating an error budget to inform the mission planner of actionable information to improve the performance.

The research in this dissertation provides a foundation for future work in the field of path planning for aircraft under threat of radar detection. Several extensions to this research may be explored and are discussed below. First, the path planner in Chapter 5 uses the INS covariance to evaluate path validity and an open-loop linear covariance model for error budget generation. This approach could be extended to a full closed-loop linear covariance model where the aircraft pose covariance is obtained from the state dispersions. The dispersions will include errors from guidance and control laws, actuator limitations, and modeled disturbances such as wind.

Second, the ASG method and PDVG path planner assume that the aircraft is traveling

at a constant altitude which reduces the planning space to a 2D plane. These components can be modified to allow changes in altitude which will affect the radar detection vector and probability of detection. This could result in a path planner that optimizes the operating altitude as part of the trajectory to avoid detection.

Third, the PDVG path planner uses an unobstructed planning space, so the radar units have a clear field of view to their maximum detection ranges. The PDVG planner could incorporate terrain models or radar counter measures to obstruct the radar field of view which could be leveraged by the path planner. This additional situational awareness may prove useful for practical planning scenarios.

APPENDIX

The RCS models used throughout this work are analytical representations of the backscattered radar cross-section for a given aircraft. The constant and ellipsoid RCS models are often used in path planning applications due to their simplicity, however, mission planners sometimes have access to a table of measured RCS values for an aircraft. This appendix presents the look-up table (LUT) RCS model that incorporates tabulated RCS data into the radar detection framework presented in Chapters 2 and 3.

RCS look-up table data provides RCS values as a function of the RCS azimuth angle α and elevation angle ϕ. The objective of the LUT RCS model is to fit a polynomial surface that envelops the LUT data. The enveloping function will provide a conservative estimate of the RCS signature of the aircraft while capturing the overall structure of the data.

Figure 1 shows an example of RCS LUT data as a function of α and ϕ. Despite the sharp spikes across the ranges of the RCS angles, there is a general structure in the LUT data that the RCS model will exploit. The LUT RCS model will fit a polynomial surface by solving

$$\min_{\boldsymbol{x}} \quad \sum_{p=0}^{P}\sum_{q=0}^{Q}\left(\mathcal{R}(\alpha_p,\phi_q)-\sigma_{rl}(\boldsymbol{x},\alpha_p,\phi_q)\right)^2 \tag{1}$$

$$\text{s.t.} \quad \mathcal{R}(\alpha_p,\phi_q) < \sigma_{rl}(\boldsymbol{x},\alpha_p,\phi_q)$$

$$\forall \quad p=0,...,P \; q=0,...,Q \tag{2}$$

where $\mathcal{R}(\alpha_p,\phi_q)$ is the measured RCS value associated with the p^{th} α and q^{th} ϕ values and

$$\sigma_{rl}(\boldsymbol{x},\alpha_p,\phi_q)=\sum_{i=0}^{N}\sum_{j=0}^{M}x_{i,j}\alpha_p^i\phi_q^j \tag{3}$$

defines the polynomial surface with coefficients defined by $\boldsymbol{x}$. The constraint in (2) ensures that the polynomial surface is larger than the sampled data at every point. This results in a conservative representation of the LUT data. Figure 2 shows the resulting polynomial fit where $N=M=5$.

The resulting polynomial surface is a function of α and ϕ and can be used as an RCS

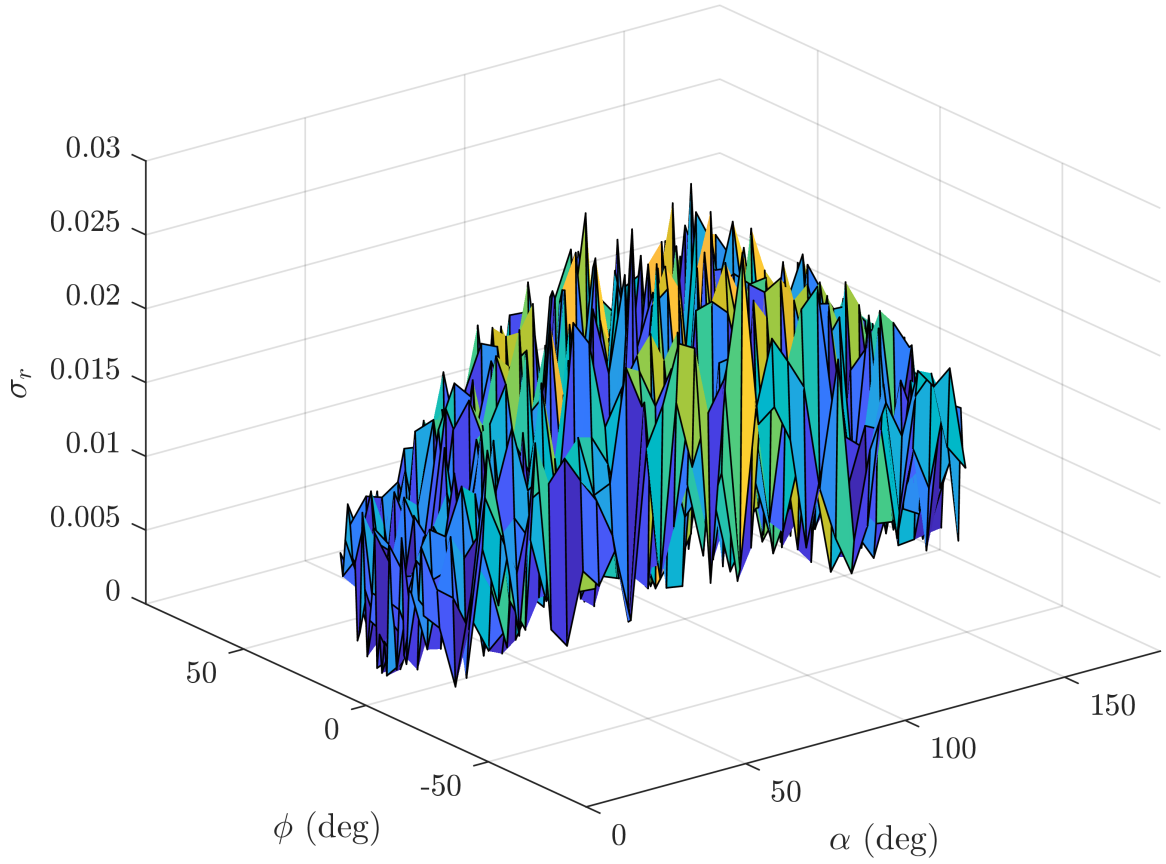

Fig. 1: LUT RCS data as a function of RCS azimuth α and elevation ϕ angles.

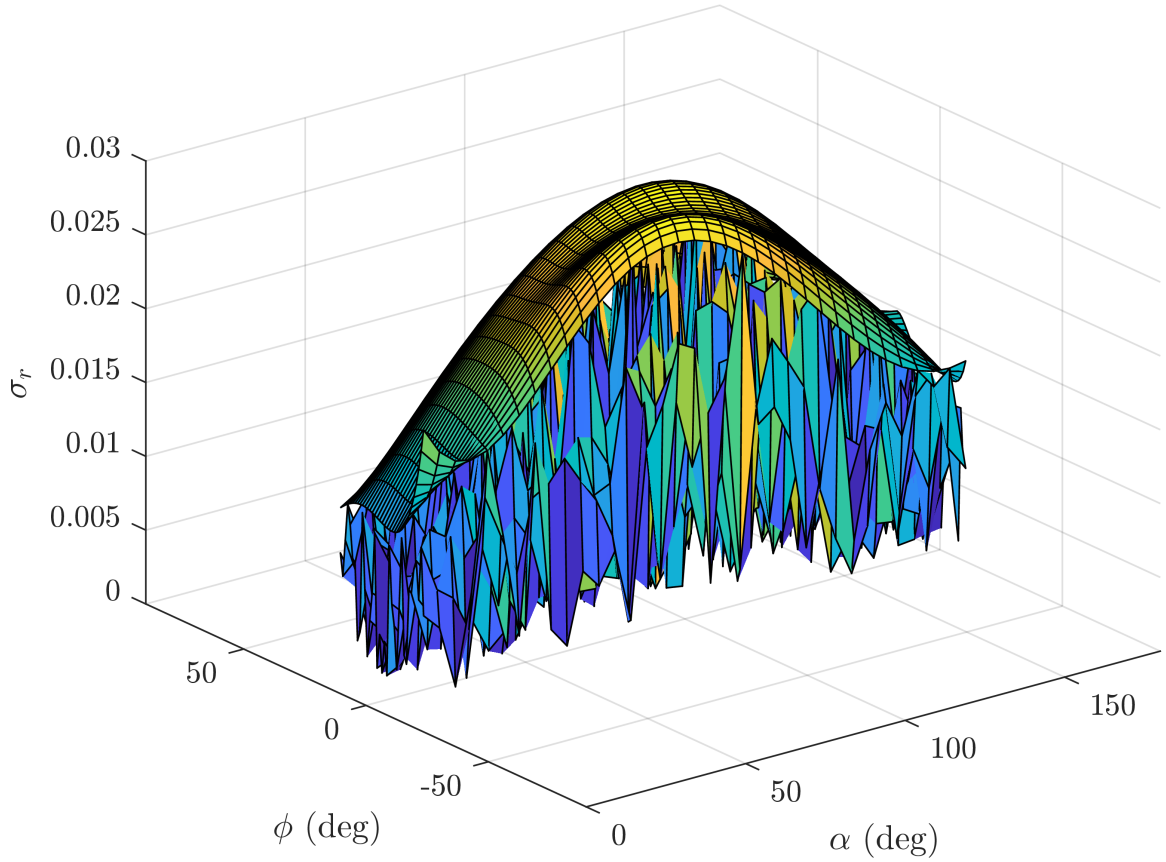

Fig. 2: LUT RCS data with enveloping polynomial surface fit.

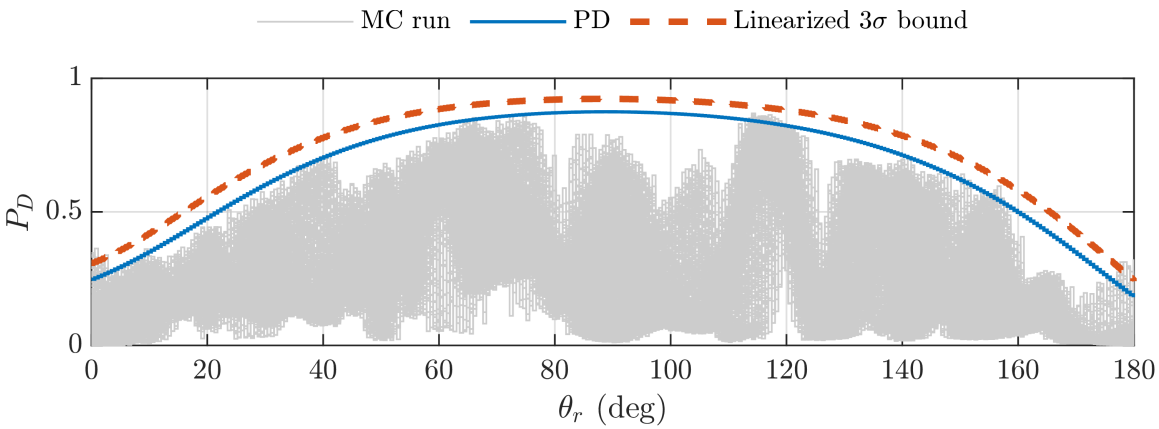

Fig. 3: Monte Carlo analysis results for P_D with "medium" level of aircraft and radar state uncertainty over the range $\theta_r = [0,\ 180]$ degrees with the LUT RCS model. The plot shows that the linearized model provides a conservative estimate of the LUT data in the presence of state uncertainty.

model in the framework presented in Chapters 2 and 3. This model is linearized by taking the partial derivative of (3) with respect to α and ϕ. These partials are given by

$$\frac{\partial \sigma_{rl}}{\partial \alpha} = \sum_{i=1}^{N} \sum_{j=0}^{M} i x_{i,j} \alpha_p^{i-1} \phi_q^j \tag{4}$$

and

$$\frac{\partial \sigma_{rl}}{\partial \phi} = \sum_{i=0}^{N} \sum_{j=1}^{M} j x_{i,j} \alpha_p^{i} \phi_q^{j-1}. \tag{5}$$

The linearization is verified by performing the same Monte Carlo analysis described in Chapters 2 and 3 with the medium level of state uncertainty, and nominal range $R = 400$ km. For this scenario, each Monte Carlo run obtained P_D values using the LUT data with linear interpolation. Fig. 3 shows P_D calculated for each Monte Carlo run for this scenario, P_D calculated with the nominal aircraft and radar states, and the upper 3-σ value from the linearized model. The key observation from this graph is that P_D and the 3-σ values calculated with the linearized model provide a conservative estimate of the detection probability.

The LUT RCS model is convenient option in situations where the mission planner has access to the measured RCS data for a given aircraft. The mission planner should consider

the general structure of the data when choosing the order parameters for the polynomial surface (N, M) and evaluate the polynomial surface to ensure that it captures the desired RCS features.

CURRICULUM VITAE

Austin D. Costley

Published Journal Articles

- Analytical Aircraft State and IMU Signal Generator from Smoothed Reference Trajectory, A. Costley, R. Christensen, R. Leishman, and G. Droge, *IEEE Transactions on Aerospace and Electronic Systems*, vol. 58, no. 3, pp. 2517-2530, 2022.

- Sensitivity of Single-Pulse Radar Detection to Aircraft Pose Uncertainties, A. Costley, R. Christensen, R. Leishman, and G. Droge, *IEEE Transactions on Aerospace and Electronic Systems*, *Accepted*

- Low Cost, Open-Source Platform to Enable Full-Sized Automated Vehicle Research, A. Costley, C. Kunz, R. Sharma, and R. Gerdes, *IEEE Transactions on Intelligent Vehicles*, vol. 6 no. 1, pp. 3-13, 2020.

Published Conference Papers

- Landmark Aided GPS-Denied Navigation for Orchards and Vineyards, A. Costley, R. Christensen, *IEEE/ION Position, Location and Navigation Symposium (PLANS)*, 2020.

Under Review

- Sensitivity of Single-Pulse Radar Detection to Radar State Uncertainty, A. Costley, R. Christensen, R. Leishman, and G. Droge, Submitted to *IEEE Transactions on Aerospace and Electronic Systems.*

- Path Planning with Uncertainty for Aircraft Under Threat of Detection from Ground-Based Radar, A. Costley, G. Droge, R. Christensen, R. Leishman, and J. Swedeen, Will Submit to *Robotics and Autonomous Systems*.